Physics of Practical Spin-Exchange Optical Pumping

by

Ian A. Nelson

A dissertation submitted in partial fulfillment

of the requirements for the degree of

Doctor of Philosophy

(Physics)

at the

UNIVERSITY OF WISCONSIN-MADISON

2001

Acknowledgements

I wish to thank first my major advisor, Prof. Thad Walker, who's scientific curiosity has always been an inspiration. I have been learning physics from him nearly as long as I have been learning physics, and I owe any future professional success I enjoy to the foundation which he has helped me to establish. I look forward to collaborating with him in the future.

I also must thank Prof. L. W. Anderson, whose assistance especially early in this work has been much appreciated. His vast experience has been an invaluable resource to me. In this vein, I also thank Dr. Bastiaan Driehuys, who has greatly speeded the completion of this work by sharing his knowledge of all things gaseous and polarizable.

I thank all Atom Trainers past and present, especially Steve Kadlecek and Bien Chann, who have both lent assistance directly related to this work — Steve through his impressive understanding of underlying quantum mechanics and Bien through his contributions as a completely tireless experimentalist.

Finally, I wish to thank my entire family for the support they have given me. First, I thank my mother, Marilyn, both for raising three great children and for giving me an appreciation for learning. I also thank my parents-in-law, Chris and Renate, for lending me love, support, and assistance with our children while I completed this writing. I look forward to the future with my beautiful loving wife, Alecia, and our two wonderful children, Jonah and Hayden, to whom I dedicate this work.

Contents

List of Figures

List of Tables

Chapter 1

Introduction

Hyperpolarized noble gases are gases in which the nuclear polarization has been increased through spin exchange with an alkali metal vapor, which has in turn been polarized through the absorption of light. Through the use of inexpensive optics and gas handling equipment, one can produce gas samples with nuclear polarization orders of magnitude beyond the thermal Boltzmann polarization in the highest attainable magnetic fields. These highly nonequilibrium systems have found applications in many very different fields.

Hyperpolarized ^{3}He has become a widely used target for nuclear physics, and it was such a target that was used in the discovery of the neutron spin-structure function [Anthony93]. The enhanced signals from hyperpolarized gases have made the nuclear magnetic resonance (NMR) study of many surface effects possible [Wu90][Raftery91]. Hyperpolarized ^{3}He and ^{129}Xe are being used together in the search for an atomic electric dipole moment [Chupp94]. However, the biggest impact of hyperpolarized noble gases is likely to be felt in medical imaging [Albert94].

Gas-phase densities (2.69×10^{19} atoms/cm^3 at S.T.P.) are typically 3 orders of magnitude lower than those of liquids, making gas-phase conventional NMR signals too

small to permit rapid magnetic resonance imaging (MRI). Conventional MRI techniques therefore image the protons of the water molecules in biological tissues. Hyperpolarized gases, however, may have polarizations 100,000 times higher than the thermal Boltzmann polarization in typical MRI magnets, more than making up for the low density [Albert94]. Early images of the lung cavities [MacFall96] have lead the way toward techniques taking advantage of diffusion, solubility, and transport of hyperpolarized noble gas atoms, including functional MRI (fMRI) of the brain [Swanson97].

For any of these applications, it is desirable to produce highly polarized ($\geq$50%) gases at high rates ($\sim$liters per hour). With this in mind, we have addressed three of the most important issues limiting current hyperpolarized gas production and use: light sources, storage times, and fundamental rate measurements.

1.1 Spin Exchange Optical Pumping Overview

This section is meant only as a way to highlight the important practical issues of spin exchange optical pumping. For a more complete overview, the reader is pointed to reference [Walker97]. For a thorough theoretical treatment of spin exchange optical pumping, see reference [Appelt98].

The first step in spin exchange optical pumping is the transfer of angular momentum from photons to alkali atoms. Figure 1.1 illustrates how this may be done using circularly polarized light resonant with the $^2S_{1/2} \rightarrow ^2 P_{1/2}$ transition in an alkali metal atom. It is assumed in figure 1.1 that the absorption line is pressure broadened sufficiently in order that the hyperfine levels are unresolved. This is almost always true in practice, where typical gas densities are 3-10 amagats, as the pressure broadening for alkalis in noble gases is 10 GHz per amagat or more, while all alkali hyperfine splittings are <10 GHz. (This picture works even at low pressures, provided that the linewidth

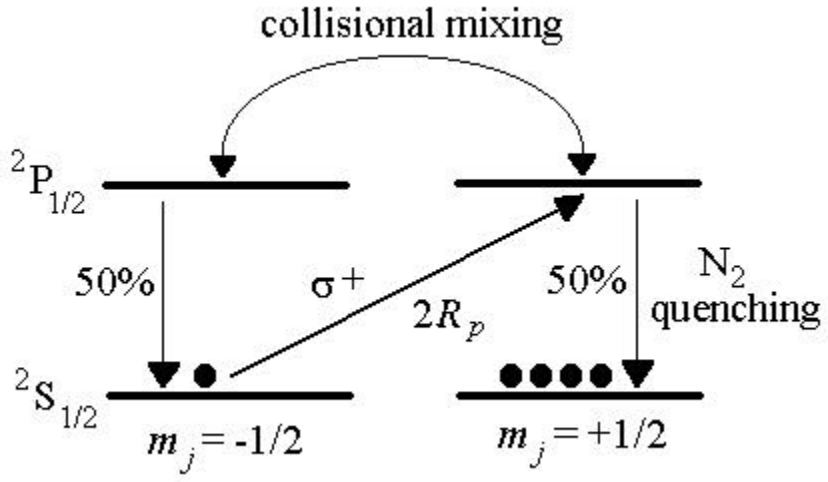

Figure 1.1: Optically pumping alkali atoms into the $m_j = +1/2$ state via circularly polarized light.

of the pumping source is much wider than the hyperfine splitting, such that all of the hyperfine levels are pumped equally.) The photon is absorbed by the atom, adding one unit of angular momentum, $\hbar$. Collisions with gas atoms in the cell mix the excited state levels. A fraction of an atmosphere of "buffer gas", typically N_2, is added to the cell in order to nonradiatively quench the excited alkali atom. The end result is that the atom is equally likely to be de-excited to either ground state level. On average, then, $\hbar/2$ units of angular momentum are deposited in the vapor with each photon absorption.

The average photon absorption rate per alkali atom is given by [Walker97]

$$\langle \delta\Gamma \rangle = (1 - 2\langle S_z \rangle) R_p, \tag{1.1}$$

where R_p is the photon absorption rate for unpolarized atoms. R_p depends upon the intensity of the incident light, I, which falls within the frequency-dependent alkali metal

absorption cross section, $\sigma(\nu)$:

$$R_p = \int_0^\infty I(\nu)\sigma(\nu)d\nu, \tag{1.2}$$

where the units of I have been chosen for convenience to be photons per time per area per unit frequency.

The equation which governs the rate of change of the alkali electron spin, $\langle S_z \rangle$, is

$$\frac{d\langle S_z \rangle}{dt} = \frac{1}{2}\left(1 - 2\langle S_z \rangle\right) R_p - \Gamma_a \langle S_z \rangle, \tag{1.3}$$

where $(1 - 2\langle S_z \rangle)R_p$ is the rate at which photons are absorbed, and each absorption event deposits on average $\frac{1}{2}$ unit of angular momentum. Γ_a is the rate at which the alkali spin is lost through collisions with other atoms in the spin exchange cell or with the walls of the cell itself. In steady state, the polarization, $2\langle S_z \rangle$, is then

$$P_a = \frac{R_p}{R_p + \Gamma_a}. \tag{1.4}$$

To produce high alkali polarization, it is necessary to make R_p larger than Γ_a. The processes which contribute to Γ_a include spin exchange and spin destruction interactions involving binary collisions, molecular processes, and diffusion of the alkali atoms to the walls of the optical pumping cell.

Some fraction of the alkali electron spin $\langle S_z \rangle$ is transferred to the nuclear spin $\langle K_z \rangle$ of the noble gas atoms in the cell via the spin exchange interaction $\alpha \mathbf{K} \cdot \mathbf{S}$. The exchange can in general occur during binary collisions or while the alkali and noble gas atoms are in short-lived van der Waals molecules.

The rate equation which governs the noble gas nuclear spin is

$$\frac{d\langle K_z \rangle}{dt} = \Gamma_{SE}(\langle S_z \rangle - \langle K_z \rangle) - 1/T_1 \langle K_z \rangle \tag{1.5}$$

High noble gas nuclear polarization $P_K = 2\langle K_z \rangle$ requires that the spin exchange rate, Γ_{SE}, is at least as large as the noble gas relaxation rate, $1/T_1$:

$$P_K = P_a \frac{\Gamma_{SE}}{\Gamma_{SE} + 1/T_1}. \tag{1.6}$$

$1/T_1$ depends in general upon magnetic field gradients [Cates88], oscillating magnetic field noise [Cates88b], and collisions with other atoms (including noble gas self relaxation [Hunt63]). However, the limiting factor in practical spin exchange systems is nearly always collisions with the walls of the cell (or storage container).

From the above discussion, it is clear that there are three main problems limiting the noble gas polarization in current practical spin exchange optical pumping systems. First, $1/T_1$ must be made small in order to acquire and store polarized gas (see equation 1.6). However, with the exception of polymer surfaces [Driehuys95], little is known about the mechanisms by which noble gases relax on storage container walls. We have done theoretical estimates and experimental measurements of noble gas relaxation on metal walls via a "surface Korringa" mechanism. This work has already had impact on the commercial polarized gas production field.

Second, to produced highly polarized alkali vapor, R_p must be made much larger than Γ_a (see equation 1.4). Most current hyperpolarization production systems use broadband diode arrays for the optical pumping. These arrays, typically with 60 Watts at 1-2 nm linewidth, necessitate the use of high pressures and temperatures to make use of a significant portion of their output power (*i.e.* to make the frequency width of $\sigma(\nu)$ a significant fraction of the width of $I(\nu)$) [Driehuys96]. We have developed a novel external cavity diode laser array (ECDLA) in order to increase R_p by decreasing the width of the laser intensity distribution rather than simply increasing the integrated intensity.

Finally, we seek to make Γ_{SE} as large and Γ_a as small as possible; however, though these rates have received some attention in the literature [Cates92][Zeng85][Ramsey83], there does not seem to be enough understanding of the fundamental processes at work in optical pumping (particularly at high pressures) to accurately predict their values. This has motivated our measurements of Γ_a and Γ_{SE} over a wider range of pressures

than has previously been done. In addition, our work represents the first measurements of the temperature dependences of these fundamental rates. These rate measurements will also allow us to measure noble gas polarizations *in situ* via all optical methods, eliminating noble gas NMR losses and the need for NMR calibrations.

1.2 Summary of results

Chapter 2 contains the main details of the apparatus used for this work, with the exception of a cell specially constructed for measuring surface relaxation. Our cell preparation techniques, low field home-built NMR system, and optical Rb polarization and number density measurement techniques are all described in turn.

Chapter 3 outlines our theoretical estimates of a possible mechanism by which ^{129}Xe atoms relax on metal surfaces. Our estimates and our measured relaxivities of Au, Ag, and In metal films are presented in table 3.1. We have also measured the relaxivity of a gold surface as a function of temperature (figure 3.3). A full table of estimated Korringa relaxivities of ^{129}Xe and ^{3}He appears in Appendix C.

Chapter 4 describes our work applying external cavities to broad area lasers (BAL's) and diode laser arrays. We have produced 16.5 Watts of output power with a 90 GHz bandwidth using only a stock diode array and optical components, and we have compared its performance to that of an unnarrowed diode laser array. The ^{129}Xe polarization produced in a spin-exchange cell by this laser is 3 times that produced by a commercially available 15 Watt fiber-coupled diode array.

Chapter 5 details our measurements of spin exchange and spin destruction rates for the Rb-^{129}Xe system. At the time of this writing, this work represents the most complete study of these rates, covering a wide range of pressures and temperatures relevant to the efficient production of hyperpolarized ^{129}Xe gas. The results from the

Rb spin loss measurements are summarized in table 1.1. From our spin exchange data,

	80°C	**150°C**
$\langle \sigma v \rangle$ (s^{-1} $amagats^{-1}$)	$(2.28 \pm 0.07) \times 10^5$	$(2.44 \pm 0.16) \times 10^5$
Γ_{vdW} (s^{-1})	3240 ± 100	2049 ± 120
$[G]_1$ (amagats)	2.8 ± 0.6	1.95 ± 0.7
$[G]_0$ (amagats)	0.100 ± 0.010	—
D_0 (cm^2/s)	0.35 ± 0.03	—

Table 1.1: Rubidium spin loss parameters obtained from Rb polarization decay curves (section 5.1).

we obtain the values of the characteristic density $[G]_1$ shown in table 1.2. In addition, we measure

$$\gamma_{SE}\Big|_{20°C} = \frac{\mathcal{K}\alpha}{2\hbar x}\frac{[G]_0}{[G]_1}\Big|_{20°C} = (1.16 \pm 0.16) \times 10^{-15} cm^3/s$$
$$\langle \sigma_{SE} v \rangle\Big|_{20°C} = (2.2 \pm 2.5) \times 10^{-17} cm^3/s.$$

Finally, combining one or more measured values from the spin loss and spin exchange data, we calculate the RbXe van der Waals molecule parameters summarized in table 1.3.

As a result of these measurements we have gained a greater understanding of the processes affecting the production of hyperpolarized ^{129}Xe gas. Chapter 6 summarizes our results as they pertain to practical ^{129}Xe spin exchange optical pumping systems. Our results suggest utilizing larger spin exchange cells, lower temperatures, lower pressures, and narrower bandwidth light sources than are currently in general use [Shah00] [Baranga98b].

	120°C	**130°C**	**140°C**	**150°C**
$[\mathrm{G}]_1$ (amagats)	2.42 ± 0.35	2.36 ± 0.34	1.96 ± 0.28	1.57 ± 0.22

Table 1.2: Characteristic density $[\mathrm{G}]_1$ obtained from Rb-^{129}Xe spin exchange data (section 5.2).

Parameter	**Value**	calculated from
τ	0.103 ns·amagats $\left(\frac{T+273}{413}\right)^{-2.64\pm0.6}$	$[\mathrm{G}]_1$
$\frac{\gamma N}{h}$	109 MHz	$[\mathrm{G}]_1$, $[\mathrm{G}]_0$
x	2.0 ± 0.2	$[\mathrm{G}]_1$, Γ_{vdW}, γ_{SE}
$\frac{\alpha}{h}$	57 MHz	$[\mathrm{G}]_1$, $[\mathrm{G}]_0$, Γ_{vdW}, γ_{SE}
$\mathcal{K}$(80°C)	2.51×10^{-22} cm^3	$[\mathrm{G}]_1$, $[\mathrm{G}]_0$, Γ_{vdW}, γ_{SE}

Table 1.3: RbXe van der Waals molecule parameters calculated from the measurements of sections 5.1 and 5.2. See those sections for definitions of parameters.

Chapter 2

General Apparatus

In most ways, our ^{129}Xe spin-exchange optical pumping apparatus resembles those used previously by other groups. We make use of siliconizing agents to coat Pyrex cells for long ^{129}Xe relaxation times, we utilize forced air to heat our cells to create significant rubidium vapor pressure, and we use either 15 Watt fiber-coupled laser diode arrays or our frequency-narrowed diode arrays (see Chapter 4) as pumping light sources. Our low-field pulsed ^{129}Xe NMR system is based upon a design given to us by Bastiaan Driehuys of Magnetic Imaging Technologies, Incorporated. We also measure rubidium polarization and number density by optical means, using a low power diode probe laser. These general features of our experiments are each described in detail below.

2.1 Spin-Exchange Cell

All of the rubidium spin-loss and spin-exchange measurements were made using a custom constructed cylindrical Pyrex cell (figure 2.1). The cell measures 4 cm in diameter by 8 cm length. The cell ends are flat, for good optical access. Two 1/4" Pyrex high vacuum O-ring sealed valves provide access to the cell for purposes of gas

filling and removal. One of these valves mates via a glass-to-metal seal to a 1.33" conflat flange for connection to the gas manifold.

The cell was initially attached to a glass vacuum manifold via a tip-off and annealed. We then cleaned the cell and the Pyrex valve stems in an ultrasonic cleaner with acetone and then with ethanol. We prepared a weak solution of SurfaSil (Pierce Chemical Company part #42800) in cyclohexane (several drops of SurfaSil to 10 ml of cyclohexane), and swished the solution around the cell interior to produce a full coating. A final rinse with ethanol removed any excess SurfaSil and cyclohexane. We then attached the manifold to a 60 l/s turbomolecular pump (Leybold Hy.Cone 60), and pumped on it while baking at 120°C for approximately one week. We chased a large droplet of natural abundance rubidium metal into the cell through the tipoff with a cool torch, and then pulled the cell off of the manifold under vacuum, using a small hot flame but being careful not to heat the cell more than necessary.

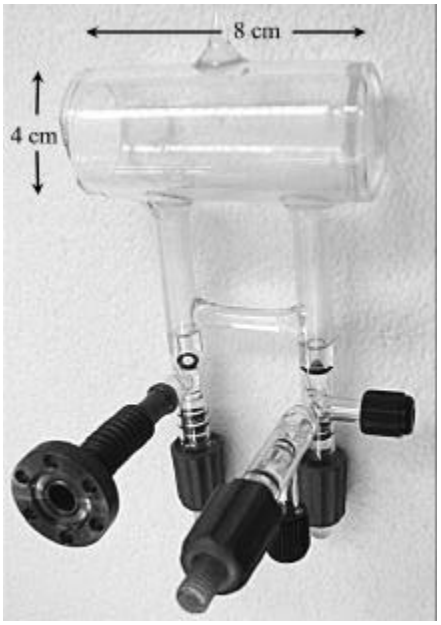

Figure 2.1: Spin-exchange cell used for spin-exchange and spin-loss measurements.

We then attached the cell to a gas manifold constructed from copper tubing via

the cell's conflat flange. A heat-activated gas purifier (UltraPure Minipurifier) serves to minimize impurities introduced to the cell with the gases. We purged and pumped out the manifold and regulators using a rotary vane pump with a foreline trap before the initial purifier activation. Because we found that the rubidium number density in the heated cell would temporarily decrease after we added gas which had been in the manifold for some time (presumably due to some impurities entering the gas, perhaps outgassing from the copper manifold itself), we also pumped the manifold out before each new gas addition. This extra step largely alleviates this problem.

2.2 Forced-Air Oven

We placed the cell in an oven specially constructed of 1/2" thick Teflon sheet assembled with brass hardware (care was taken throughout this work to avoid the use of even weakly ferromagnetic items in and around the spin-exchange oven, as magnetic field gradients are associated with spin relaxation (see equation 2.6). 50.8 mm diameter windows provide optical access from the front to the rear of the oven. The cell's inlet and outlet valves protrude through holes in the oven wall (figure 2.2).

Heat is provided via air forced through a process air heater (Omega part#AHP 5051) and delivered to the oven through insulated copper tubing. A resistive thermal device (RTD) taped directly on the cell between the two arms provides temperature measurements and feedback to a PID temperature controller (Omega part# CN77000), which in turn provides 110 Volts to the process air heater as needed via a zero-switching solid state relay (Omega part# SSR240DC25).

The oven is mounted on an XY-translation stage which in turn is mounted on a (nonmagnetic) optical lab jack, which allows us to carefully center the cell in a 1 meter diameter Helmholtz pair. We use the width of the frequency-domain ^{129}Xe NMR signal

(see section 2.4) to position the oven as well as to adjust the positions of the coils themselves. The translation stage and lab jack provide a means to make millimeter-scale movements of the oven, and we use cardboard shims to make millimeter-scale adjustments to the coil positions. We measure the width of the ^{129}Xe NMR signal before and after each adjustment, and minimize that width with respect to oven and coil positions. Several extra turns on one of the Helmholtz coil forms and a second power supply allow us to shim any residual longitudinal field gradients, and we minimize the NMR signal width with respect to current through those extra turns as well. In this way, we provide a longitudinal magnetic field at the cell of up to 30 Gauss with gradients on the order of 1 mG/cm or less (see section 2.4).

2.3 Broadband pumping source

Commercially available 15 Watt fiber-coupled diode arrays (Optopower Corporation OPC-A015-FCPS) provide the optical pumping light for much of this work. Because the fiber output is unpolarized, we approximately collimate it using a 50 mm focal length lens, and then pass the resulting beam through a polarizing beam splitter cube. The two resulting linearly polarized beams may then be directed toward the cell and circularly polarized via separate $\lambda/4$ plates. We have felt the need to check that each "polarizing" beam-splitter cube is indeed polarizing (by simply observing the transmission of each output beam through a sheet of polarizer material), as we have come across several in our laboratory which do not properly polarize both output beams.

Care must be taken to avoid imaging the end of the fiber bundle onto the spin exchange cell, as the resulting inhomogeneous light field would lead to reduced Rb polarization (though R_p scales linearly with light intensity, the polarization of the Rb

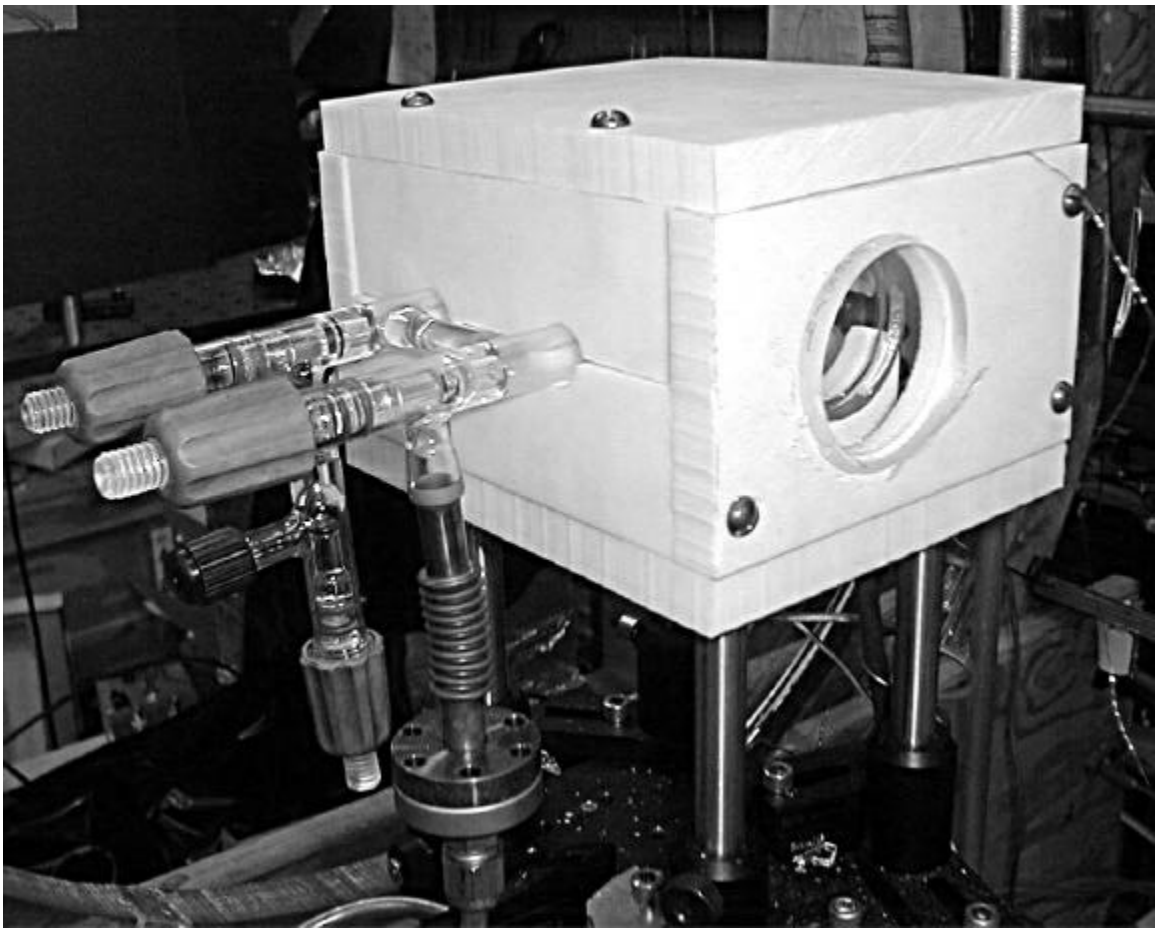

Figure 2.2: Forced air oven, showing inlet and outlet arms of spin-exchange cell.

does not). In practice, we have imaged the collimating lens onto the cell with the desired magnification (the same technique is employed in overhead projectors to avoid an image of the light bulb on the screen).

2.4 NMR

We detect xenon polarization using a custom-built LabView-controlled low field NMR system (figure 2.3). A single tuned 200-turn coil wound from 34 gauge magnet wire around a 9 mm diameter Teflon form ($Q = \omega L/R \approx 18$ at 25 kHz, $L = 1.0$ mH) serves as both the pulse coil and the sense coil. Silicone RTV secures the coil to the top of the spin-exchange cell, its axis perpendicular to the longitudinal DC field. We first send a short resonant 25 kHz pulse (generated by a National Instruments 500 kHz DAQ card) through the coil with the analog switch open. We then close the analog switch in order that electronic noise from the DAQ card is attenuated rather than amplified (the "diode gate" pictured also serves to block noise from the DAQ card). After allowing 1-3 ms for the coil to ring down, the voltage induced in the coil by the precessing ^{129}Xe magnetization may be measured.

This free induction decay (FID) signal is amplified and then sent to a Stanford Research Systems 830 lock-in amplifier. The lock-in phase-sensitive detector (PSD) multiplies the atoms' signal, $V_{sig}\sin(\omega_{sig}t + \phi_{sig})$ by the reference $V_{ref}\sin(\omega_{ref}t + \phi_{ref})$, generating difference and sum frequencies:

$$\begin{aligned} V_{PSD} = \quad & \frac{1}{2}V_{sig}V_{ref}\sin((\omega_{sig} - \omega_{ref})t + (\phi_{sig} - \phi_{ref})) + \\ & + \frac{1}{2}V_{sig}V_{ref}\sin(\omega_{sig} + \omega_{ref})t + (\phi_{sig} + \phi_{ref})) \end{aligned} \tag{2.1}$$

If the result is low pass filtered with sufficient bandwidth ($(\omega_{sig} - \omega_{ref}) \ll$bandwidth$\ll$

$\omega_{ref}, \omega_{sig}$) the lock-in output is

$$V_{out} = \frac{1}{2} V_{sig} V_{ref} \sin((\omega_{sig} - \omega_{ref})t + (\phi_{sig} - \phi_{ref})). \tag{2.2}$$

In practice, we set the internal reference of the lock-in 50-100 Hz from the ^{129}Xe resonant frequency. Our 50-100 Hz mixed down FID signal is then read by the DAQ card (figure 2.3).

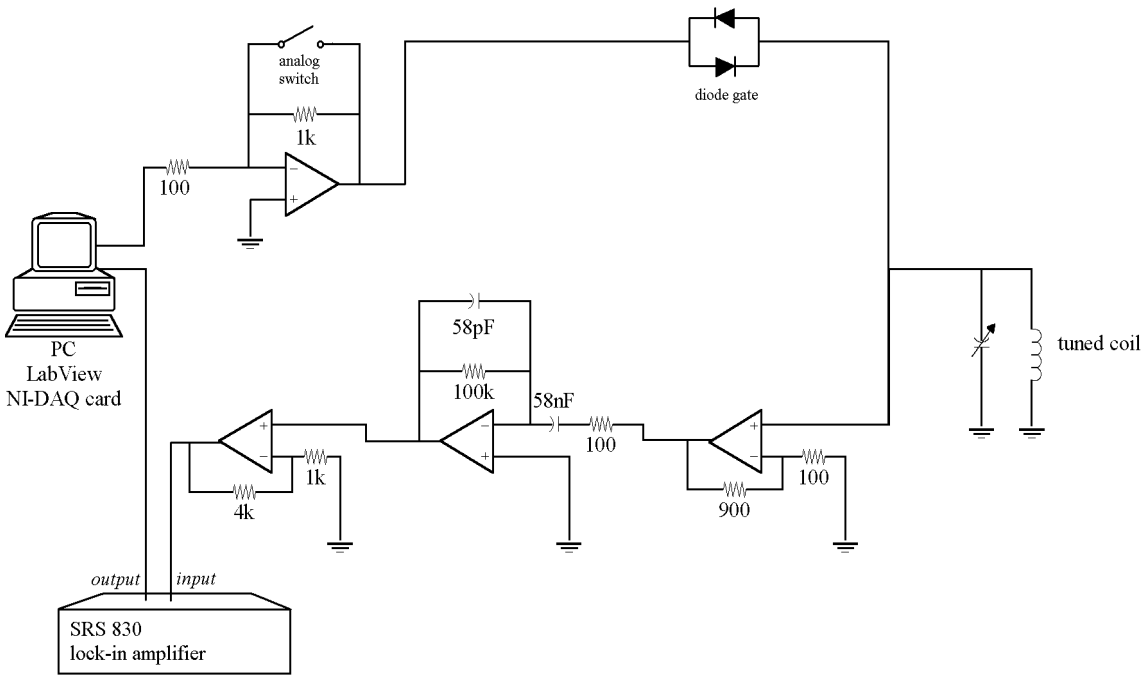

Figure 2.3: Pulsed NMR detection circuit.

The FID signal (figure 2.4) can be analyzed in either the time or frequency domain. The analysis is straightforward in the time domain, where we assume the form

$$V(t) = V_{FID} \sin(2\pi f_0 t + \phi)\, e^{-t/T_2^*}, \tag{2.3}$$

and perform a least-squares fit to the raw data using V_{FID}, f_0, ϕ, and T_2^* as free parameters. The initial induced voltage, V_{FID}, is proportional to ^{129}Xe magnetization.

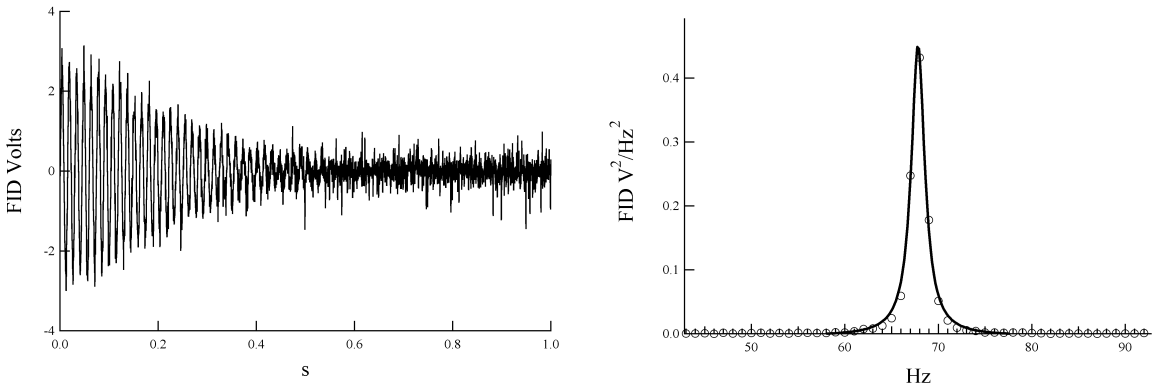

Figure 2.4: Typical free induction decay following NMR pulse. The frequency domain signal is the square of the magnitude of the FFT of the time domain signal. A Lorentzian fit is superimposed on the data.

T_2^* is the coherence time of the ^{129}Xe spins in the transverse plane, which in very high pressure (*i.e.* very low diffusion) experiments is dominated by longitudinal magnetic field inhomogeneities [CSH]:

$$\frac{1}{T_2^*} \approx 2\pi\gamma|\nabla_z B|l. \tag{2.4}$$

For ^{129}Xe , $\gamma = g_{Xe}\mu_B/h = 1.178$ kHz / Gauss, and l is a characteristic length of the system; we take l to be approximately equal to the sense coil diameter, 1 cm.

In the frequency domain, we square the magnitude of the FFT of equation 2.3 to obtain a Lorentzian:

$$|\mathcal{F}(V(t))|^2 = \frac{(V_{FID}/2\pi)^2}{(f-f_0)^2 + (1/2\pi T_2^*)^2}. \tag{2.5}$$

We can fit this Lorentzian to the squared Fourier transformed data using V_{FID}, f_0, and T_2^* as free parameters.

A typical FID signal (figure 2.4) yields $T_2^* \approx 300$ ms, for a longitudinal field gradient $|\nabla_z B| < 1$ mG/cm from equation 2.4. Monitoring T_2^*, then, allows us to estimate the ^{129}Xe relaxation rate due to magnetic field inhomogeneities [GamblinCarver65]

[SchearerWalters65]:

$$\frac{1}{T_1} = D\left|\frac{\nabla_T B}{B_0}\right|^2, \tag{2.6}$$

where D is the diffusion constant for the ^{129}Xe spins ($D = 0.791 \pm .032$ cm^2/s for Xe in one atmosphere of He [Hasson90]), and $\nabla_T B$ is the transverse gradient of the longitudinal (z-oriented) magnetic field B_0. Applying equation 2.6 along with the relation $\nabla_T B \approx \nabla_z B/2$ to our system yields $1/T_1 < 1 \times 10^{-9}$ s^{-1}, much slower than the ^{129}Xe relaxation due to surface interactions.

2.5 Rb polarization

We detect rubidium polarization optically, using both Faraday rotation and circular dichroism. For this purpose, we have constructed a low power probe laser using a 40 mW single mode diode (Sharp LT025MD) in a Littman-Metcalf cavity, with output tunable ∼10 nm on either side of the Rb D2 line (780.23 nm). Either neutral density filters or a $\lambda/2$ plate and polarizing beam splitter cube allow us to cut probe laser intensity sufficiently to produce no detectable perturbation on the Rb polarization.

Our Rb spin-loss measurements were done using this probe laser along with an analyzer designed to detect the Faraday rotation of the linearly polarized probe beam. Located behind the cell, it consists of a $\lambda/2$ plate, a polarizing beam splitter cube, and two photodiodes (one at each output of the cube) wired such that their photocurrents subtract from each other (see figure 2.6). With no optical pumping, the $\lambda/2$ plate is set such that the photodiodes together give zero output current (i.e. equal light to each arm of the analyzer). When the Rb vapor has polarization P ($-1 < P < +1$), it induces a Faraday rotation angle ϕ on the linear probe beam polarization [Wu86]:

$$\frac{d\phi}{dP} = \frac{\pi[\mathrm{Rb}]le^2c}{3mc^2}\left(\frac{\Delta_{3/2}}{\Delta_{3/2}^2 + \gamma_{3/2}^2/4} - \frac{\Delta_{1/2}}{\Delta_{1/2}^2 + \gamma_{1/2}^2/4}\right), \tag{2.7}$$

where $\Delta_{3/2}$ is the probe beam detuning from the Rb D2 line (angular frequency) and $\Delta_{1/2}$ is the probe beam detuning from the Rb D1 line. For $\Delta \gg \gamma$, equation 2.7 reduces to

$$\frac{d\phi}{dP} \approx \frac{\pi[\mathrm{Rb}]le^2c}{3mc^2}\left(\frac{1}{\Delta_{3/2}} - \frac{1}{\Delta_{1/2}}\right). \tag{2.8}$$

The photodiodes put out a current proportional to $\sin(\phi)$, which for small ϕ is proportional to Rb polarization. The resulting current is amplified and converted to a voltage which can be displayed on an oscilloscope. By chopping the optical pumping beam, we can monitor both the buildup and decay of the Rb polarization (figure 2.5).

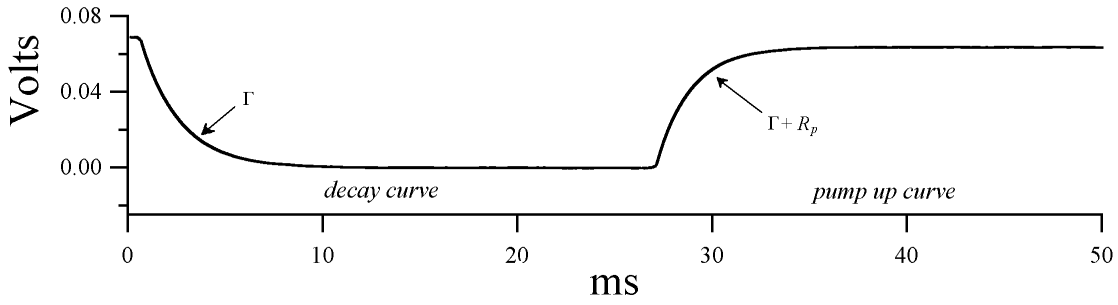

Figure 2.5: Rb polarization decays and then is repumped as the pump beam is chopped (1000 averages).

2.6 Rb polarization and number density

Our Rb spin-exchange and polarization calibration measurements made use of the same analyzer. However, we added a photoelastic modulator (PEM) and a $\lambda/4$ plate to the probe beam path in front of the cell, and a switch to one of the photodiodes which allowed us to either add or subtract photodiode currents. We used a lock-in amplifier (SRS 810) to analyze the amplified photodiodes' output. These extra features allow us

to monitor circular dichroism as well as Faraday rotation, enabling us to measure Rb number density as well as to make absolute Rb polarization measurements.

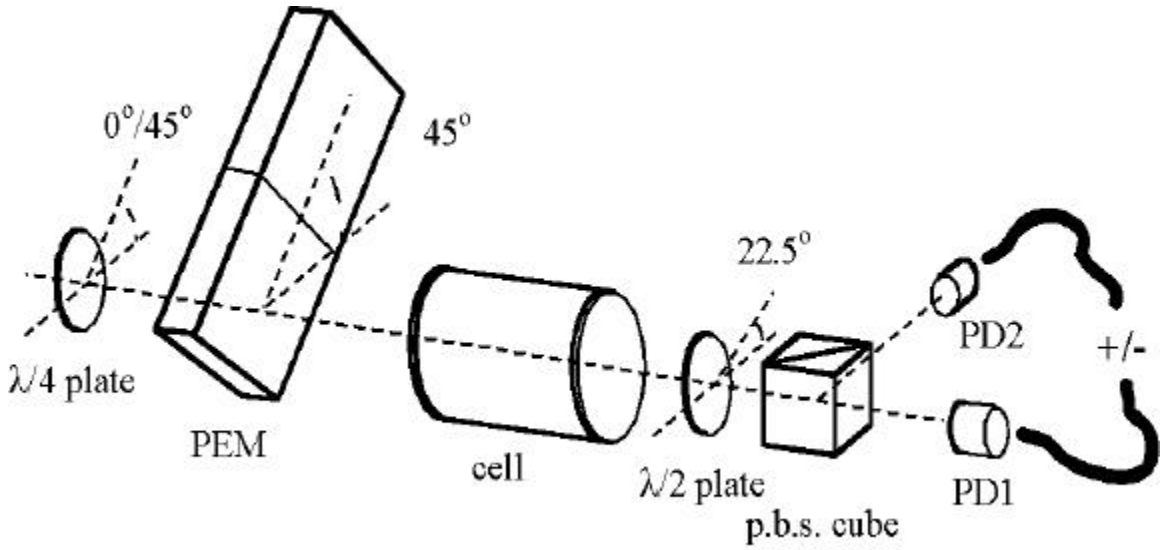

Figure 2.6: Photoelastic modulator and associated polarization analyzer optics. Upper / lower settings for measuring circular dichroism / Faraday rotation. The $\lambda/2$ plate is set such that it forms a +/- 45° polarizer in combination with PD1 / PD2.

2.6.1 PEM circular dichroism measurement

Circular dichroism (differential absorption between left and right circularly polarized light) is a direct consequence of Rb polarization. For light resonant with the Rb D2 line ($5S_{1/2} \rightarrow 5P_{3/2}$),

$$\sigma_+ = \frac{1}{2}\sigma_\circ(2+P) \tag{2.9}$$

$$\sigma_- = \frac{1}{2}\sigma_\circ(2-P), \tag{2.10}$$

where $\sigma_{+/-}$ is the absorption cross section for light circularly polarized along / against the Rb polarization. $\sigma_\circ$ is the absorption cross section for unpolarized atoms.

The probe beam is initially linearly polarized with its electric field vector, $\vec{\varepsilon}$, along $\hat{x}$ (90° in the notation of figure 2.6). With the optics in the upper configuration (for circular dichroism), the $\lambda/4$ plate does not alter the probe polarization. The probe polarization vector before entering the PEM can then be resolved into components along the PEM fast axis, $\hat{f}$, and slow axis, $\hat{s}$, (at ±45° to $\hat{x}$). The effect of the PEM can then be written as modulations on both the $\hat{f}$ and $\hat{s}$ components:

$$\vec{\varepsilon}(t) = \frac{\hat{f}e^{\frac{i\theta(t)}{2}} + \hat{s}e^{-\frac{i\theta(t)}{2}}}{\sqrt{2}}, \tag{2.11}$$

where $\theta(t) = \beta\sin(\omega t)$ (β is the PEM retardation and ω is the PEM modulation frequency, $2\pi\times50$ kHz). More algebra allows us to resolve the (modulated) polarization vector into left- and right-handed circularly polarized components, $\hat{r}_{\pm} = \frac{1}{\sqrt{2}}(\hat{x} \pm i\hat{y})$:

$$\vec{\varepsilon}(t) = \frac{\hat{r}_+}{\sqrt{2}}\left(\cos\frac{\theta(t)}{2} + \sin\frac{\theta(t)}{2}\right) + \frac{\hat{r}_-}{\sqrt{2}}\left(\cos\frac{\theta(t)}{2} - \sin\frac{\theta(t)}{2}\right). \tag{2.12}$$

Now each circularly polarized component is absorbed by the cell as per its own absorption cross section ($\sigma_{\pm}$), leaving a total transmitted intensity, $I(t)$:

$$I(t) = e^{-\frac{1}{2}n(\sigma_+ + \sigma_-)l}\left(\cosh\left(\frac{1}{2}n\left(\sigma_+ - \sigma_-\right)l\right) + \sin\theta\sinh\left(\frac{1}{2}n\left(\sigma_+ - \sigma_-\right)l\right)\right). \tag{2.13}$$

Using equations 2.9 and 2.10 as well as the relation [Abramowitz]

$$\sin\left(\beta\sin\omega t\right) = 2\sum_{k=0}^{\infty} J_{2k+1}(\beta)\sin\left(2k+1\right)\omega t \tag{2.14}$$

leads us to the following form for the transmitted probe intensity:

$$I(t) = e^{-n\sigma_\circ l}\left(\cosh\left(\frac{1}{2}n\sigma_\circ lP\right) + 2J_1(\beta)\sin\omega t\sinh\left(\frac{1}{2}n\sigma_\circ lP\right)\right), \tag{2.15}$$

where, because we will observe only the DC photodiode signal and the fundamental frequency (via lock-in amplifier), we have included only the first term from the sum in equation 2.14. The beam-splitter cube splits the light, but the two photodiodes' outputs are summed, yielding

$$V(t) = V_{DC}\left(\cosh\left(\frac{1}{2}n\sigma_\circ lP\right) + 2J_1(\beta)\sin\omega t\sinh\left(\frac{1}{2}n\sigma_\circ lP\right)\right), \tag{2.16}$$

where V_{DC} is the DC photodiode signal (both channels summed together) with no pump beam ($P = 0$), and sent to the lock-in. The lock-in returns the rms voltage at frequency ω,V_{cd}, given by

$$V_{cd} = \sqrt{2} V_{DC} J_1(\beta) \sinh(\frac{1}{2} n \sigma_\circ l P). \tag{2.17}$$

2.6.2 PEM Faraday rotation measurement

Switching the optics to the lower configuration of figure 2.6 allows us to monitor the Faraday rotation of the probe beam. In this configuration, the light entering the PEM is circularly polarized:

$$\vec{\varepsilon} = \frac{\hat{f} + i\hat{s}}{\sqrt{2}} \tag{2.18}$$

Again we apply modulation to each component, but now we consider the rotation angle, ϕ, of the polarization vector induced by the cell:

$$\vec{\varepsilon}(t) = \frac{1}{\sqrt{2}} e^{-\frac{1}{2} n \sigma_\circ l} \left(\left(\hat{f} \cos\phi + \hat{s} \sin\phi \right) e^{\frac{i\theta(t)}{2}} + i \left(\hat{s} \cos\phi - \hat{f} \sin\phi \right) e^{\frac{-i\theta(t)}{2}} \right). \tag{2.19}$$

The $\lambda/2$ plate angle is set such that the beam splitter cube acts as a polarizer with its axis aligned with either $\hat{f}$ or $\hat{s}$, depending upon which photodiode is being monitored. If we allow only the $\hat{f}$ component of the probe to pass, we see a transmitted intensity I_1 at one photodiode given by

$$I_1(t) = \frac{1}{2} e^{-n\sigma_\circ l} - \frac{1}{2} e^{-n\sigma_\circ l} 2 J_1(\beta) \sin\omega t \sin 2\phi. \tag{2.20}$$

Similarly, the intensity at the second photodiode is given by

$$I_2(t) = \frac{1}{2} e^{-n\sigma_\circ l} + \frac{1}{2} e^{-n\sigma_\circ l} 2 J_1(\beta) \sin\omega t \sin 2\phi. \tag{2.21}$$

The two channels are subtracted and sent to the lock-in, which returns

$$V_{fr} = \sqrt{2} V_{DC} J_1(\beta) \sin 2\phi. \tag{2.22}$$

2.6.3 Rb number density

Measuring V_{DC}, V_{cd}, V_{fr}, and $n\sigma_\circ l$ (simple absorption of the probe beam) allows us to calculate n and P. The Rb number densities, n, obtained in this way tend to be $\sim$ 20% lower than one would expect from measured temperatures and published vapor pressure curves, e.g. those measured by Killian [Killian26]:

$$n = 10^{(3.55-4132/T)}/kT. \tag{2.23}$$

(The units of T are °K, n is given in number per cm^3). This is, however, consistent with observations of laser absorption in our laboratory in this and similar optical pumping cells.

We note that though we have not checked that the pumping light is not generating a coherence between the Rb Zeeman levels ($m_J = \pm 1$), we feel that this is a highly unlikely source of systematic error. High photon absorption and Rb loss rates both tend to destroy any such coherence, as does the large Rb electron precession frequency in our magnetic field (0.467 MHz/G).

Chapter 3

Relaxation on Metal Surfaces

As pointed out in the introduction (equation 1.6), acquiring and storing polarized gas requires a system with a long noble gas relaxation time. Magnetic field gradient induced relaxation [Cates88]

$$\Gamma = D\left|\frac{\nabla_T B}{B}\right|^2 \tag{3.1}$$

can be minimized through the use of fairly uniform holding fields (see section 2.4, for example). Relaxation due to magnetic field noise at the ^{129}Xe resonant frequency [Cates88b] can be minimized by using moderate holding fields (to increase the ^{129}Xe resonant frequency above prevalent low frequency noise), and by surrounding the gas with metal shielding over a skin depth thick. Xe-Xe spin-rotation induced relaxation limits storage times to 56/[Xe] hrs·amagats [Hunt63] [Torrey63], but even this is long compared to relaxation times in most systems. Hyperpolarized ^{129}Xe gas storage times are currently limited chiefly by relaxation on the walls of the container used to store it. With the exception of relaxation on polymer surfaces [Driehuys95], very little is known about xenon surface relaxation mechanisms. Extending theoretical estimates of ^{129}Xe and ^{3}He relaxation on alkali surfaces by Driehuys, Cates, and Happer (private communication), we have explored ^{129}Xe relaxation on select metal surfaces.

Throughout this work, "relaxivity", ϱ, is defined as the relaxation rate, Γ, experienced by a volume V of gas enclosed in a container with surface area S multiplied by the ratio V/S:

$$\varrho = \Gamma V/S \tag{3.2}$$

Relaxivity (with units length/time) is then a property of a surface, and is independent of container geometry.

3.1 Surface Korringa Relaxation

Following Driehuys, Cates, and Happer, we postulate that the mechanism by which noble gas atoms relax on metal surfaces is an extension of the theory put forth by Korringa [Korringa50] for relaxation of nuclei in metallic solids. An excellent derivation of this theory appears in [Slichter]. According to that theory, a nuclear spin relaxes when, during an electron scattering event, the spin state of the nucleus is changed. It is important to note that this nuclear spin state change must be accompanied by a corresponding flip of the scattering electron's spin. This is only allowed by the Pauli exclusion principle if the final electron state is initially unoccupied. Therefore Fermi statistics dictate that only those electrons with energy within approximately kT of the metal's Fermi energy contribute to the nuclear relaxation. The resulting relaxation rate for nuclei in metals is given by [Slichter]

$$\frac{1}{T_K} = \frac{(4\pi)^6}{9h^7}(g_s\mu_B\frac{\mu_K}{K})^2\eta^4 m^3 \epsilon_F kT, \tag{3.3}$$

where the linear temperature dependence is from the Fermi statistics and is considered the signature of Korringa relaxation.

Again following Driehuys *et al.*, we modify this theory to treat noble gas atoms adsorbing and subsequently relaxing upon metal surfaces. We assume that a noble gas

atom, interacting with the metal surface via an attractive atom-surface potential, experiences some reduced conduction electron density at its position due to the electrons' wave functions penetrating outside the metal (the evanescent wave). It is the electrons in this exponentially decreasing Fermi sea which we assume contribute to the noble gas nuclear polarization.

Assuming low surface coverage, the noble gas atoms in the bulk are free to sample the atom-surface potential $U(l)$ (where $l = 0$ is the "edge" of the metal). The Boltzmann factor $e^{-U(l)/kT}$ gives us the ratio of the density of atoms at distance l to the density of atoms in the bulk, N/V. The number dN of noble gas atoms found between distance l and $l + dl$ of the surface is then

$$dN = \frac{N}{V} S e^{-U(l)/kT} dl, \tag{3.4}$$

where S is the surface area of the metal.

The Korringa relaxation rate $1/T_K$ experienced by noble gas atoms is a function of distance, owing to the rapid decrease of the conduction electron density outside the surface. We define $f(l)$ to be the fractional density of conduction electrons outside the surface (referenced to $f(l) = 1$ inside the metal). Then the contribution $d\left(\frac{1}{T}\right)$ to the total relaxation rate of the N gas atoms in the cell due to the atoms between l and $l + dl$ is

$$d\left(\frac{1}{T}\right) = \frac{1}{T_K(l)} \frac{dN}{N} \tag{3.5}$$

$$= \frac{1}{T_K} f(l)^2 \frac{S}{V} e^{-U(l)/kT} dl. \tag{3.6}$$

Integrating both sides gives us the total surface Korringa relaxation rate for the noble gas:

$$\frac{1}{T} = \frac{1}{T_K} \frac{S}{V} \int_0^\infty f(l)^2 e^{-U(l)/kT} dl \tag{3.7}$$

We follow Driehuys, Cates, and Happer in defining a characteristic length parameter, b:

$$b = \int_0^\infty f(l)^2 e^{-U(l)/kT} dl. \tag{3.8}$$

Physically, b is a measure of the amount of overlap between the density of electrons outside the surface and the position of a noble gas atom near the surface. From our definition of relaxivity, the surface Korringa relaxivity of a metal is

$$\varrho = \frac{1}{T_K} b. \tag{3.9}$$

As will become apparent, we have made many gross simplifications and idealizations in our atom-surface interaction calculations; we seek only a rough theoretical framework to describe surface Korringa relaxation. In particular, here we have chosen to treat the metal surface naïvely as an "edge" at $l = 0$. With this assumption, $f(l)$ is easily estimated from the work function ϕ of the metal:

$$f(l) = e^{-\sqrt{\frac{2\phi m}{\hbar}} l}. \tag{3.10}$$

In the interest of generating a table of candidates for polarized gas containers, we have developed a semiempirical algorithm for approximating the atom-surface potential function and resulting surface Korringa relaxivity from the following parameters: noble gas polarizability, metal work function, and metal conduction electron density. We first assume an atom-surface potential of form

$$U(l) = -c_3/l^3 + B/l^6. \tag{3.11}$$

The coefficient of the van der Waals attraction term, c_3, is calculated from the noble gas polarizability. We take as a starting point the potential energy between the noble gas atom and its image in the (perfectly conducting) metal [Bruch]:

$$U_{vdW} = -\frac{\langle p_z^2 \rangle}{4z^3} \tag{3.12}$$

We relate $\langle p_z^2 \rangle$ to the polarizability $\alpha(0)$ of the noble gas atom [Bonin]:

$$\alpha(0) = \frac{2e^2}{3\hbar} \sum_l \frac{|\langle l|\bar{r}|0\rangle|^2}{\omega_{l0}} \tag{3.13}$$

$$\approx \frac{2e^2}{\hbar} \frac{\langle l|z|0\rangle^2}{\omega_{l0}}, \tag{3.14}$$

where in the last step $\hbar\omega_{l0}$ is the energy difference between the noble gas atom ground state and first excited state. Inserting $\langle p_z^2 \rangle = e^2 \langle l|z|0\rangle^2$ into equation 3.12 yields

$$c_3 \approx \frac{\alpha(0)\hbar\omega_{l0}}{8}. \tag{3.15}$$

From equation 3.15, $c_3 = 4$ ev·Å^3 for ^{129}Xe and 0.5 eV·Å^3 for ^{3}He. B is to be determined by comparison with previously measured adsorption energies.

The repulsive term in $U(l)$ arises due to Fermi overlap between the metal's electrons and those of the noble gas atom near the surface. We have chosen the functional form of the repulsion term purely for convenience; with this form we can simply relate c_3, B, the location of the potential minimum l_0, and the binding energy $U(l_0)$:

$$B = \frac{c_3 l_0^3}{2} \tag{3.16}$$

$$U(l_0) = -\frac{c_3}{2l_0^3} \tag{3.17}$$

Due to the physical origin of the repulsive term, we assume further that B is a function of the electron density outside the metal surface. In practice, we have made the observation that accepted potentials for noble gas atoms on metals as different as rubidium and silver exhibit minima at approximately the same fractional electron density, f_0. From equation 3.10, this corresponds to the statement that l_0, the location of the potential minimum, roughly scales like $1/\sqrt{\phi}$. The constant of proportionality obviously depends upon the noble gas; we manually adjusted f_0(Xe) and f_0(He) such that the binding energies of the two agree with accepted binding energies of the two

on silver, and verified that the agreement with other adatom-metal potentials is fairly quantitative.

$$f_0(\mathrm{Xe}) = 0.00735 \tag{3.18}$$

$$f_0(\mathrm{He}) = 0.000361 \tag{3.19}$$

We stress that potential functions derived in this manner are only very crude approximations to actual atom-surface potentials, and that more rigorous theoretical [Nordlander84] [Chizmeshya92] and semiempirical (e.g. Lennard-Jones (12,6)) methods of potential function approximation exist. However, our approximations do agree fairly quantitatively with more rigorous calculations. We note that the trends exhibited by our approximate potentials hold true under more rigorous study [Bruch], and that it is those trends which we hope to use to identify possible polarized noble gas storage materials.

The chief justification for our approximate method is that while work functions have been measured and tabulated for all of the elemental metals [Hölzl79] [Riviere69] [Michaelson77], potentials are available in the literature for only a few. Appendix C contains a table of predicted Korringa relaxivities for ^{129}Xe and ^{3}He on the elemental metals, calculated using our approximations.

Our calculations suggest that ^{3}He surface Korringa relaxivity is not an issue for polarized gas storage; the relaxivities listed in Appendix C lead to storage times (in a practical sized container) of many years. ^{3}He surface relaxation must occur through some other as yet unknown mechanism. Predicted ^{129}Xe surface Korringa relaxivities, however, are sufficiently high on many elemental metals (with the notable exception of very reactive metals) to make Korringa relaxation an important issue for polarized ^{129}Xe storage. In particular, ^{129}Xe surface Korringa relaxation on noble metals is predicted to be the dominant relaxation mechanism in practical sized containers, allowing for

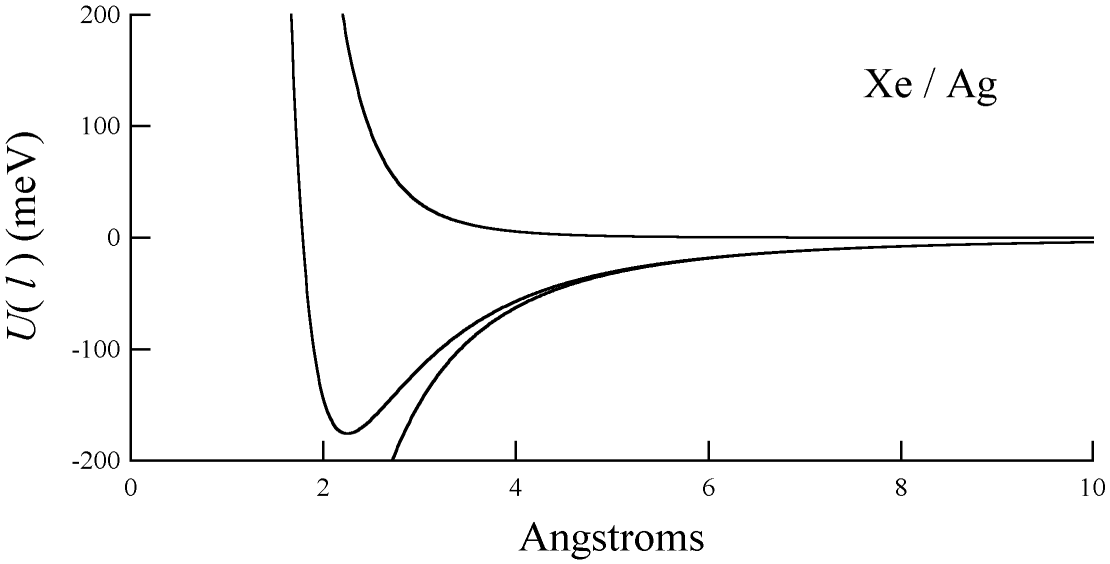
Xe / Ag
200
100
0
-100
-200
0
2
4
6
8
10
U(l) (meV)
Angstroms

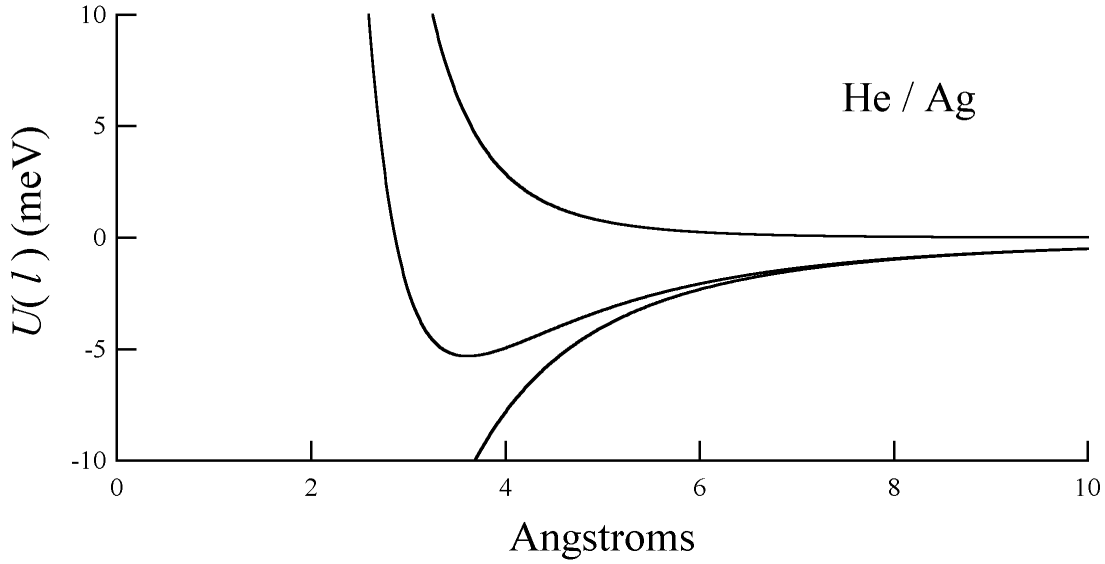
He / Ag
10
5
0
-5
-10
0
2
4
6
8
10
U(l) (meV)
Angstroms

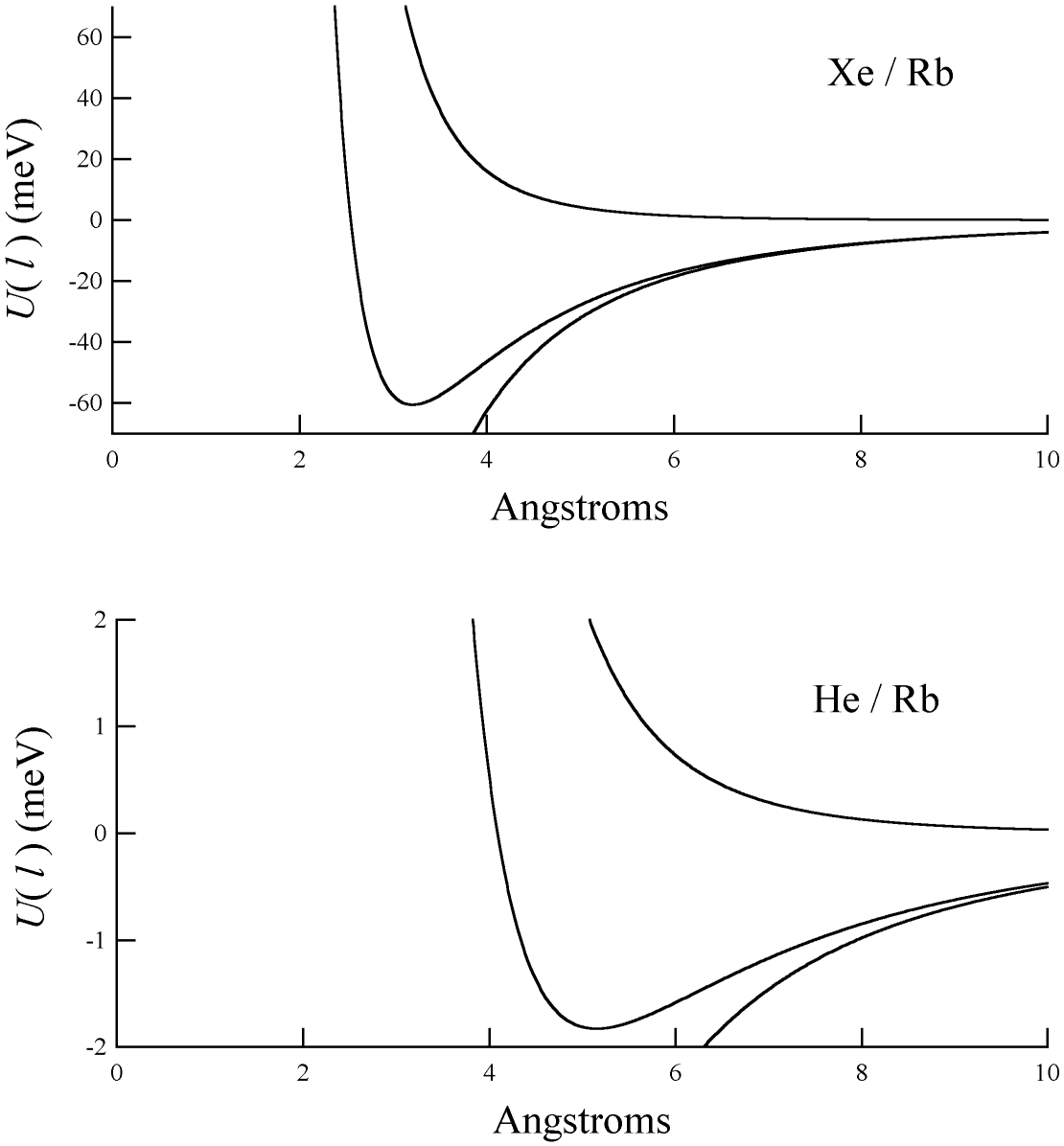

Figure 3.1: Potential functions approximated by the method described in the text. Each graph shows the attractive $-l^{-3}$ van der Waals term, the repulsive l^{-6} Fermi term, and the total potential function.

convenient study.

The very different predicted behavior of ^{129}Xe vs. ^{3}He relaxivities arises from their very different polarizabilities, and deserves comment. The high polarizability of ^{129}Xe leads to strong van der Waals attractive forces between the adatom and the metal substrate. This in turn leads to a ^{129}Xe-metal binding energy which (at moderate temperatures) is large compared to the relevant energy scale, kT. This is particularly true if the surface in question has tightly bound electrons (high work function), allowing the ^{129}Xe atom to approach very near to the surface. The integral expression for b then becomes very nearly equal to

$$b \approx f(l_\circ)^2 e^{-(U(l_\circ)/kT)} \delta l, \tag{3.20}$$

where $\delta l \sim 1$ Ångstrom is the width of the absorption potential well (figure 3.1). More tightly binding surfaces (deeper potential $U(l_\circ)$) therefore are predicted to be more highly relaxing to ^{129}Xe.

Calculated ^{3}He surface Korringa relaxivities, by contrast, exhibit the opposite behavior. The remarkably low polarizability of ^{3}He leads to binding energies on all elemental metal surfaces which are much less than kT. We can then approximate b as

$$b \approx \int l_{cross} f(l)^2, \tag{3.21}$$

where l_{cross} is the distance from the surface at which the ^{3}He-metal potential crosses from positive (repulsive) to negative (attractive). ^{3}He surface Korringa relaxivity, therefore, is predicted to be much higher on metals with loosely bound electrons (low work function), which contribute more to $f(l)$ in the integral.

These considerations also lead to contrasting temperature dependences of the two species' surface Korringa relaxivities (figure 3.2). As we have seen, the characteristic length, b, for ^{3}He on metal surfaces is nearly independent of temperature. The dominant

temperature dependence in its predicted relaxivity on a metal surface arises from the linear temperature dependence of the Korringa rate itself (equation 3.3), leading to calculated relaxivities which increase only slightly faster than linearly with temperature. The dominant temperature dependence of ^{129}Xe relaxation, however, arises from the characteristic length, b, which is approximately an exponentially decreasing function of temperature. We expect ^{129}Xe relaxivities, therefore, to decrease with temperature nearly like $kTe^{-U(l_\circ)/kT}$ (slightly slower than exponentially).

It may be conceptually useful to connect the relaxivity of a surface to the picture of atoms diffusing to and bouncing off of the surface in question. The diffusion equation must govern the transport of the nuclear spins to the walls of their container:

$$\frac{\partial\langle K_z\rangle}{\partial t} = D\nabla^2\langle K_z\rangle - \Gamma\langle K_z\rangle, \tag{3.22}$$

where D is the diffusion coefficient and Γ is the relaxation rate of spins in the bulk. This equation is often solved for alkali spins in optical pumping cells with the boundary condition that the polarization goes to zero at the walls (the highly relaxing walls limit). Here we are interested in the opposite case, the limit of weakly relaxing walls.

The weakly relaxing walls limit is defined as $\tau_{dif} \ll \tau_w$, where τ_{dif} is the diffusion time across the cell and τ_w is equal to $1/\Gamma_w$, the relaxation time due to the walls of the cell. (Though τ_w scales like cell length, τ_{dif} scales like length squared, leading to a cell size dependence to the weakly relaxing walls limit condition.) In the weakly relaxing walls limit, $\langle K_z\rangle$ is very nearly uniform throughout the cell. We therefore average equation 3.22 over the volume of the cell:

$$\frac{\partial\langle K_z\rangle}{\partial t} = -\Gamma\langle K_z\rangle + \frac{D}{V}\int dV\nabla^2\langle K_z\rangle, \tag{3.23}$$

and use Green's theorem to convert the diffusion term to a surface integral:

$$\frac{D}{V}\int dV\nabla^2\langle K_z\rangle = \frac{D}{V}\int dS\mathbf{n}\cdot\nabla\langle K_z\rangle \tag{3.24}$$

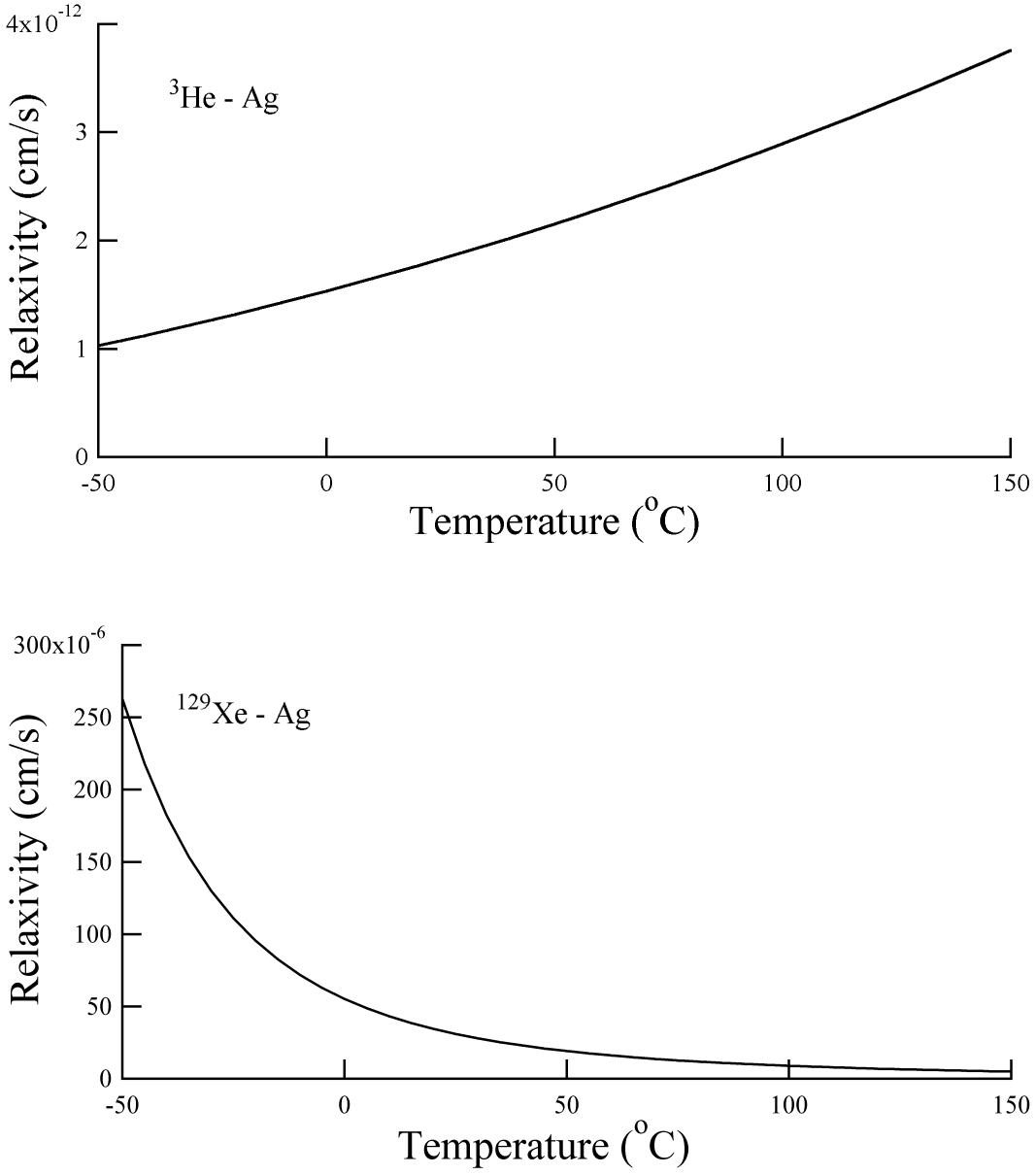

Figure 3.2: Predicted ^{3}He (top) and ^{129}Xe (bottom) relaxivities vs temperature on Ag.

where $\mathbf{n}$ is the outward normal to the surface. We next turn to find an expression for $\mathbf{n} \cdot \nabla \langle K_z \rangle$.

From kinetic theory [Reif], the flux of atoms into the wall must be $[\mathrm{A}]\bar{v}/4$; if $\langle K_z \rangle$ is uniform throughout the cell, the flux of spins into the wall, j_+, must then be

$$j_+ = \frac{[\mathrm{A}]\bar{v}\langle K_z \rangle}{4}. \tag{3.25}$$

We define α to be the fraction of wall bounces which result in the loss of spin. The flux of spin out of the wall in steady state is then

$$j_- = (1-\alpha)\frac{[\mathrm{A}]\bar{v}\langle K_z \rangle}{4}. \tag{3.26}$$

But by the definition of diffusion,

$$-D[\mathrm{A}]\mathbf{n} \cdot \nabla \langle K_z \rangle = j_+ - j_- \tag{3.27}$$

$$= \alpha[\mathrm{A}]\overline{v}/4. \tag{3.28}$$

Solving for $\mathbf{n} \cdot \nabla \langle K_z \rangle$ and inserting the result into equation 3.24 yields the relaxation rate of the nuclear spins:

$$\frac{\partial \langle K_z \rangle}{\partial t} = -\Gamma \langle K_z \rangle - \frac{\alpha \overline{v} S}{4V} \langle K_z \rangle. \tag{3.29}$$

From our definition of relaxivity, ϱ, we obtain

$$\varrho = \frac{\alpha \bar{v}}{4}. \tag{3.30}$$

It is interesting to note that though we started with the diffusion equation, the end result is independent of the diffusion constant, D. Though it retains the velocity dependence, the end result is independent of gas density (assuming that α, the fraction of bounces which relax a spin, is independent of density). This is the signature of the "weakly relaxing walls" limit.

Equation 3.30 connects the relaxivities we have estimated in the previous section to the number of wall bounces it takes to relax a nuclear spin, $1/\alpha$:

$$\varrho = \frac{1}{T_K} b = \frac{\alpha \bar{v}}{4}. \tag{3.31}$$

(The interesting temperature dependence of the Korringa relaxivity in this way translates to an interesting temperature dependence to $\alpha\bar{v}$.) For example, the estimated Korringa relaxivity of Xe on Au at 20°C is 1×10^{-4} cm/s, which translates to

$$\alpha(\mathrm{Xe} - \mathrm{Au}) \approx 10^{-8}. \tag{3.32}$$

It takes an estimated 100 million wall bounces to depolarize a Xe nucleus in a gold container.

3.2 Measured Relaxivities

As a first test of surface Korringa theory, we chose to study ^{129}Xe relaxivity on gold, silver, and indium on the basis of these metals' chemical inactivity and availability in high purity. We prepared thin films of these three metals on microscope cover slips. The cover slips were cleaned successively for ten minutes in an ultrasonic cleaner with trichloroethylene, acetone, and ethanol (all spectroscopic grade), and then blown dry with clean nitrogen. The coverslips were then placed in a thermal deposition chamber which we pumped down overnight to $\sim 10^{-8}$ Torr with an oil diffusion pump fitted with a liquid nitrogen cold trap. We then thermally evaporated the particular metal of interest, depositing it onto cover slips at approximately 10 Å/s (as measured by a crystal deposition monitor). By controlling the exposure time of the cover slips, we were able to produce films approximately 1200 Ångstroms thick.

These thin films have little effect on the low field NMR techniques which we use to measure ^{129}Xe polarization. Both the tipping pulse from the tuned coil and the atom's

signal to the coil are attenuated as a function of the metals skin depth, $\delta(\omega)$:

$$B(\omega) = B_{\circ} e^{-\tau/\delta(\omega)}, \tag{3.33}$$

where τ is the thickness of the coating and $\delta(\omega)$ is given by [Jackson]:

$$\delta(\omega) = (2/\mu\omega\sigma)^{\frac{1}{2}}. \tag{3.34}$$

The skin depth of gold at 25 kHz (our ^{129}Xe NMR frequency) is then 0.45 mm, or a factor of 4000 larger than the thickness of our coatings. It is interesting to note that, due to the frequency dependence of δ, low field NMR has an advantage over high field NMR for performing measurements of hyperpolarized gases inside metal containers. For example, the skin depth of gold at 106 MHz, the ^{129}Xe resonant frequency in a 9 Tesla field, is only 6.9 μm, a factor of 60 smaller than the skin depth in our low 25 kHz field.

The relaxivities of the resulting films were measured at Magnetic Imaging Technologies, Inc., now a division of Nycomed Amersham Imaging. There a Pyrex chamber with walls coated with a siliconizing agent (DMDCS, Pierce Chemical Company) has been constructed in two sections, such that samples may be placed inside and the chamber sealed with an elastomer O-ring. The chamber can be pumped out using a mechanical pump with foreline trap, and polarized ^{129}Xe may be introduced via a high vacuum Pyrex valve with O-ring seal. A low field pulsed NMR system such as has been described in Chapter 2 is used to monitor the ^{129}Xe polarization as a function of time. The measured relaxation rate of the empty chamber is subtracted from the measured relaxation rate of the chamber with sample inside to obtain the relaxation rate due to the sample itself. This relaxation rate is then multiplied by the ratio of the volume of the chamber to the measured (macroscopic) surface area of the sample to obtain the relaxivity of the sample itself. The measured and calculated relaxivities of the three metals appear in Table 3.1.

	Predicted Relaxivity	**Measured Relaxivity**	$\mathbf{T}_{1cc}$ **(min.)**
Gold	1.07×10^{-4}cm·s^{-1}	8.45×10^{-5}cm·s$^{-1} \pm 30\%$	41 ± 12
Silver	3.76×10^{-5}cm·s^{-1}	4.55×10^{-5}cm·s$^{-1} \pm 8\%$	75.6 ± 5.7
Indium	1.13×10^{-5}cm·s^{-1}	6.63×10^{-5}cm·s$^{-1} \pm 20\%$	52 ± 11

Table 3.1: Predicted vs. measured relaxivities for thermally deposited metal films. Also included is the relaxation time of ^{129}Xe in a 1 cm^3 sphere coated with the film (calculated from measured relaxivity).

The measured results for ^{129}Xe relaxation on gold and silver surfaces are within 20% of the predicted values, however the measured relaxivity of the indium surface is $\sim 6\times$ the predicted value. However, though the gold and silver samples appeared mirror-like to the eye, the indium surface seemed to sparkle, suggesting a less than atomically smooth surface. Indeed, upon examination under an atomic force microscope (AFM), the indium surface can be seen to be made up of many granules, with characteristic size approximately 1 μm (figure 3.3).

This observation underscores the possible difficulty associated with assigning a macroscopic surface area to a surface with microscopic features. Though this difficulty is minimized by the use of gold and silver samples (thermal deposition of these metals produces relatively smooth surfaces), we might expect that the true microscopic surface area of even these samples is somewhat larger than the macroscopic area of the cover slip substrate.

Though we cannot properly call this data evidence either for or against surface Korringa relaxation as the dominant relaxation mechanism, we are encouraged that the measured relaxivities are even the correct order of magnitude. Though previous work has suggested long ^{3}He relaxation times in metal coated cells [Heil95], it was commonly believed that ^{129}Xe would relax much more strongly on metals than our work

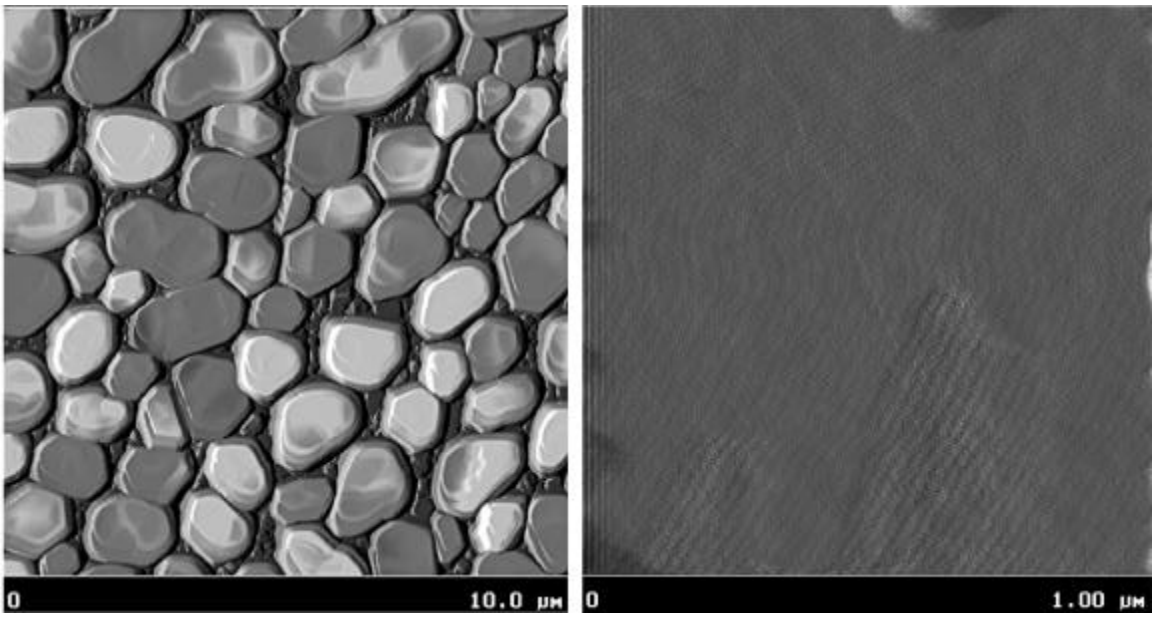

Figure 3.3: AFM images comparing indium and gold surfaces. The height scale for the indium image is 200 nm, while that for the gold surface is 10 nm. The faint "ripple" in the gold image is an instrumental artifact.

has shown to be the case [DriehuysPC]. Indeed, as a result of this work, a commercial polarized gas production system has been redesigned, with aluminum fittings replacing the fragile glass fittings previously used to handle polarized ^{129}Xe [DriehuysPC].

3.3 Temperature Dependence

It is the temperature dependence of equation 3.3, due to Fermi statistics, which is considered evidence for Korringa relaxation in solid state systems. Though we expected this temperature dependence to be somewhat obscured in surface Korringa relaxation due to the temperature dependence of the characteristic length, b, we chose to explore the temperature dependence of ^{129}Xe relaxation on a gold surface. We want a system in which the metal surface is the dominant source of ^{129}Xe relaxation; of the three metal surfaces we have examined, gold is the most chemically inert and most relaxing. For this experiment, we designed a two-chambered Pyrex cell, with a high vacuum Pyrex valve positioned between the two chambers (figure 3.4). The flattened two-piece spin-down chamber has a 50 cm^3 volume (obtained by measuring the volume of water which fit in the chamber prior to the coating process) and an 80 cm^2 surface area (approximated by measuring the linear dimensions of the chamber interior), yielding $S/V = 1.6$ cm^{-1} ($\sim 1/3$ that of a 1 cm^3 sphere).

We thermally deposited a thin gold film on the interior of the spin-down chamber using the technique detailed above. Owing to the shape of the chamber interior, some areas received a much thicker coating than others; in order to assure that the coating was at least several hundred Ångstroms thick everywhere, some areas were likely coated microns thick. Therefore we might expect the chamber coating to be less smooth than our earlier coverslip coatings.

We then attached the cell to a glass vacuum manifold via a tipoff on the spin-up

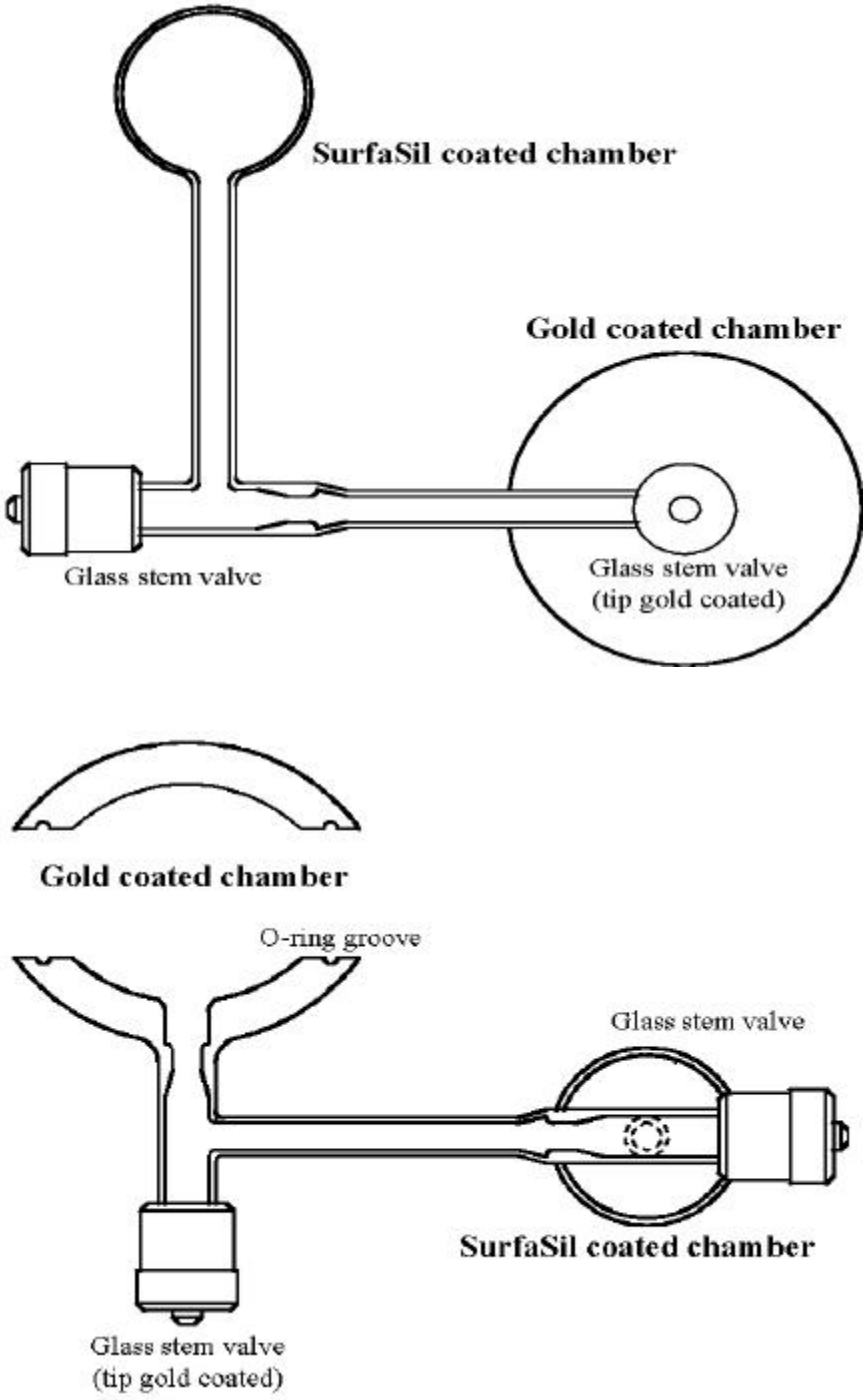

Figure 3.4: Surface studies cell.

chamber, and coated the interior of the spin-up chamber with SurfaSil, as was described in Chapter 2. We fabricated an aluminum clamp with brass hardware, and used it to make an O-ring seal between the two halves of the spin-down chamber. At this point, we pumped the entire cell down to 10^{-7} Torr using a turbomolecular pump and baked at 120°C for approximately one week. We then chased a small amount of Rb metal into the spin-up chamber and filled the cell with the desired gas composition in the following manner: we filled the entire manifold and cell with 4 amagats of natural abundance Xe, closed the valve to isolate the spin-down chamber, and pumped out the remaining Xe. We then filled the manifold and spin-up cell with 150 Torr of N_2 and pulled the cell off of the manifold with a small hot flame.

Because the freezing point of Xe, 161 K, is significantly higher than the boiling point of nitrogen, 77.2 K, we were able to freeze the Xe into the spin-up chamber by simply holding that chamber several inches above liquid nitrogen with the isolation valve open. We could then close the valve and allow the xenon to thaw, leaving us with 8 amagats Xe and ∼50 Torr N_2 in the spin-up chamber and ∼50 Torr of N_2 in the spin-down chamber. We placed the spin-up chamber in a temperature controlled forced air oven centered in 1 m diameter Helmholtz coils. The oven was designed with a hole through which the tubing connecting the two chambers could protrude. Anti-reflection coated windows provided straight-through optical access to the cell.

We illuminated the spin-up chamber at 80°-100°C with 24 Watts of circularly polarized light from two fiber-coupled diode arrays, and allowed time for the ^{129}Xe polarization to build up through spin-exchange with the Rb vapor. We then allowed the cell and oven to cool to 40°-50°C while continuing to optically pump any Rb still in the vapor. After turning off the pumping light, we reversed the cell so that the spin-down chamber was in the oven and briefly opened the isolation valve to allow polarized ^{129}Xe to flow into the spin-down chamber. After allowing the oven and spin-down chamber

to equilibrate at the desired temperature, we used the low field NMR detection system described in Chapter 2 to observe the ^{129}Xe polarization decaying as a function of time (figure 3.5).

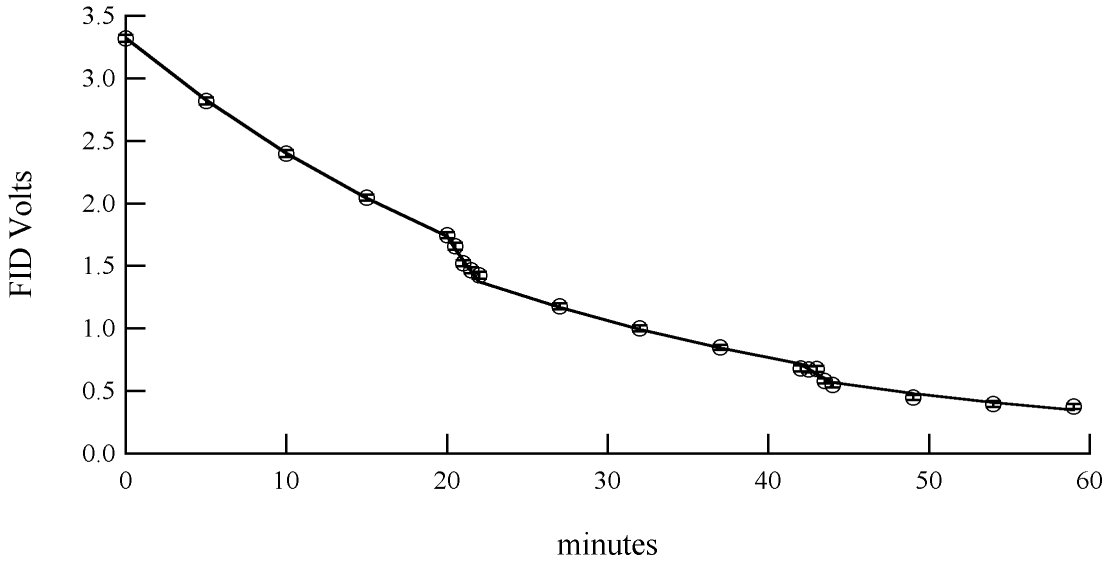

Figure 3.5: FID voltage received by NMR coil as a function of time at 60°C, including fit.

Because some fixed fraction of the total ^{129}Xe magnetization is lost with each pulse, we avoided using uniform pulse rates, instead staggering the pulses as shown and including the fixed fraction of polarization lost with each pulse as a parameter of the fit. For example, the fit to the data displayed in figure 3.5 yields a relaxation time T_1 of 43.5 minutes ±2.5 minutes and 4.6% ±0.4% of magnetization lost with each pulse. This relaxation rate corresponds to a relaxivity of 2.4×10^{-4} cm·s^{-1}.

We repeated this process at temperatures ranging from -40°C to 120°C. In order to reach temperatures below room temperature, we directed the oven air through copper tubing immersed in liquid nitrogen prior to flowing it through the process air heater on its way to the oven. Our results for ^{129}Xe relaxation rate in the gold-coated spin-down

chamber as a function of temperature appear in figure 3.6, along with the relaxation rate predicted by the Korringa theory.

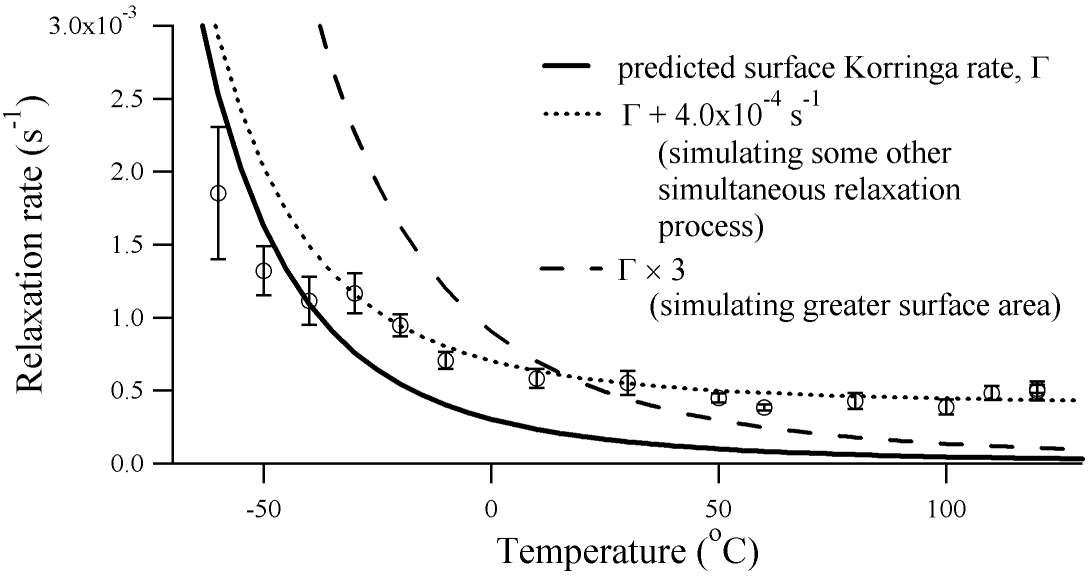

Figure 3.6: Measured ^{129}Xe relaxation rate in gold-coated chamber, including three theory curves (see text).

The solid theory curve has been plotted using the previously measured $S/V = 1.6$ cm^{-1} and includes no free parameters. This surface area to volume ratio was obtained by simply measuring the interior dimensions of the gold-coated chamber, and so reflects the macroscopic surface area of the gold surface; the actual microscopic surface area of the gold coating could only be larger, and is most likely much larger, as was discussed above. It is obvious that the data deviates from the theory by being significantly flatter (less dependence upon temperature).

There are two obvious parameters in the theory which we could vary in an attempt to explain the data: 1) we could increase the surface area to volume ratio, S/V, to take into account surface roughness; and/or 2) we could add a constant (positive) offset to the theory curve to represent other (temperature independent) relaxation processes

which might be affecting the ^{129}Xe (e.g. magnetic field inhomogeneities and magnetic field noise). The long dashed theory curve is the solid curve multiplied by a factor of three, in order to simulate larger surface area (this factor was chosen for agreement at $\sim$20°C). We see that applying a larger surface area to the theory curve results in a steeper theoretical temperature dependence (and an even poorer fit to the data).

Adding 4×10^{-3} s^{-1} to the solid theory curve to represent other relaxation generates the short dashed curve (again, this factor was chosen for agreement at $\sim$20°C). Once again, the data is obviously less temperature dependent than the theory. (We note that relaxation on the O-ring, which likely would be temperature dependent [Driehuys95], is assumed to be negligible, as the O-ring surface area exposed to the ^{129}Xe is $< 1\%$ of the area of the gold surface.)

A third option is to suppose that the measured relaxation is due to the surface, but the mechanism is not Korringa relaxation. Assuming a simple exponential temperature dependence of relaxation rate (as we might expect without the Korringa relaxation mechanism) results in even stronger temperature dependence.

It is clear that by any of these reasonable analyses, the data is less temperature dependent than equation 3.9 predicts. This has lead us to question the implicit "low fractional surface coverage" assumption made in equation 3.9.

A simple argument leads us to conclude that the fraction of filled ^{129}Xe adsorption sites on the gold surface under our experimental conditions is not negligible. We first calculate the 2D ^{129}Xe density on the surface assuming that the surface coverage is low. Under this assumption, the surface density, s, is related to the 3D gas density ,[Xe], via the relation

$$s = [\mathrm{Xe}]\lambda, \tag{3.35}$$

where λ is a characteristic length reflecting the strength of the atom-surface potential

compared to kT:

$$\lambda = \int_0^\infty e^{-U(l)/kT} dl \tag{3.36}$$

Performing this integration using our Xe-Au potential yields the surface density vs. temperature curve shown in figure 3.7.

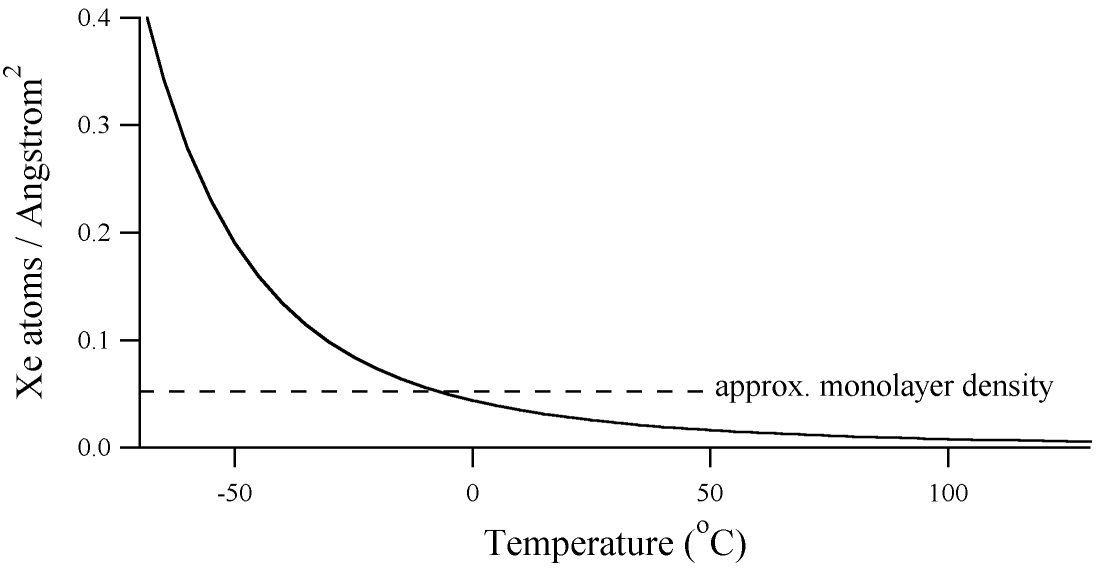

Figure 3.7: Surface density of Xe on Au from equation 3.36 (low fractional coverage assumption).

We expect that the 2D lattice constant for a Xe monolayer adsorbed on Au is approximately equal to that in the 3D solid [Bruch], or $\sim$ 4.4 Ångstroms. Allowing 19.4 Å^2 per atom yields 0.052 atoms per Å^2, or approximately the surface density which our low coverage assumption suggests as high as 0°C . Of course, this does not mean that we should expect a full Xe monolayer on the gold surface, only that our low coverage adsorption theory is inadequate to predict the actual coverage.

We must modify equation 3.9 to reflect that there is a finite number of possible ^{129}Xe adsorption sites on the gold surface, corresponding to a surface density s_{max}, while that equation predicts the relaxivity due to a surface density [Xe]λ. If a fraction

f_s of the s_{max} sites are filled, then the surface Korringa relaxivity equation is

$$\varrho = \frac{1}{T_K} b \left(\frac{f_s s_{max}}{[\mathrm{Xe}]\lambda} \right). \tag{3.37}$$

We estimate f by setting the flux into the surface equal to the flux leaving the surface:

$$\frac{[\mathrm{Xe}]v}{4}(1 - f_s) = \frac{f_s s_{max}}{\tau}, \tag{3.38}$$

where we have assumed that because a fraction $(1 - f_s)$ of sites are unfilled, a fraction $(1 - f_s)$ of atoms incident on the surface "stick"; and τ is the average time an adatom stays on the surface. However, $v\tau/4$ is just the characteristic length, λ, from equation 3.36. We find, then, that

$$f_s = \frac{[\mathrm{Xe}]\lambda}{[\mathrm{Xe}]\lambda + s_{max}}, \tag{3.39}$$

yielding the following form for surface Korringa relaxivity:

$$\varrho = \frac{1}{T_K} b \left(\frac{s_{max}}{s_{max} + [\mathrm{Xe}]\lambda} \right). \tag{3.40}$$

In the low coverage limit ($[\mathrm{Xe}]\lambda \ll s_{max}$), equation 3.40 reduces to equation 3.35. In the high coverage limit ($[\mathrm{Xe}]\lambda \gg s_{max}$), equation 3.40 yields the relaxivity due to a full Xe monolayer:

$$\lim_{([\mathrm{Xe}]\lambda/s_{max} \to \infty)} \varrho = \frac{1}{T_K} b \left(\frac{s_{max}}{[\mathrm{Xe}]\lambda} \right). \tag{3.41}$$

It is perhaps interesting to note that in the high coverage limit, the coating relaxivity (and therefore the cell relaxation time) is expected to be inversely proportional to gas pressure. We concern ourselves only with the first monolayer for two reasons: first, a xenon atom approaching an already occupied adsorption site experiences a much weaker van der Waals attractive force to the surface, decreasing the odds of "sticking"; and second, ^{129}Xe atoms in the second and higher layers experience less interaction with the metal's conduction electrons due to the exponential decay of the factor $f(l)$ in equation 3.8.

We fit the data of figure 3.6 to the following function:

$$\frac{1}{T} = \frac{1}{T_K} b \left(\frac{s_{max}}{s_{max} + [\mathrm{Xe}]\lambda} \right) \frac{S}{V}, \tag{3.42}$$

allowing 0.052 Xe atoms per Å^2, and with S/V as a free parameter. The results of this fit appear in figure 3.3. The value for S/V from the fit, 170 ± 18 cm^{-1}, is two orders of magnitude larger than our measured value. This suggests that the chamber coating is much rougher than we had hoped. In any case, it is obvious that the effect of including the maximum surface coverage in our theory is to flatten the temperature dependence of the theoretical relaxation rate (better agreement with experiment). The qualitative agreement between theory and experiment is encouraging.

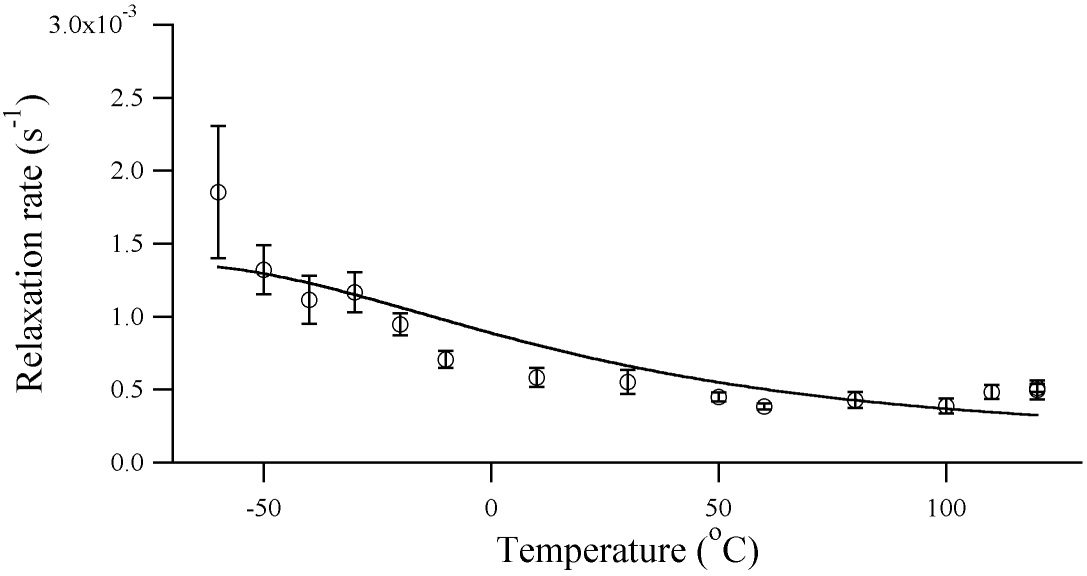

Figure 3.8: Fit to data of figure 3.6 using revised theory.

3.4 Surface Conclusions

In light of our new appreciation for Xe monolayer effects on metals, we must change the predicted relaxivities of table 3.1. Appendix C contains columns for estimated

^{129}Xe surface Korringa relaxation times both with and without the modifications of equation 3.40. The theoretical estimates for the relaxivity of gold, silver, and indium films are seen to decrease by up to a factor of three (for gold) at 20°C. We believe that for the cases of our gold and silver coverslips, this decrease is most likely made up for by surface roughness — the microscopic surface area is likely a factor of ∼3 larger than the macroscopic surface area we measured. For the case of indium, the obvious surface roughness leads us to believe that the microscopic surface area is easily a factor of 6 (or more) larger than the macroscopic area we measured.

We note that the interiors of Pyrex spin exchange cells are often visibly coated with alkali metal films, and yet the relaxivities of these cells are orders of magnitude smaller than the alkali relaxivities predicted in appendix C. This could perhaps be due to paramagnetic impurities in the alkali or chemical compounds formed between the alkali atoms and impurities in the cells — the same loosely bound electrons which cause noble gases to be so weakly physically bound to alkalis make those alkalis very chemically reactive.

We are encouraged by the rough agreement between our calculations and measurements, and hope that this work will help lead to not only better hyperpolarized gas storage and handling techniques, but also a greater understanding of fundamental surface relaxation mechanisms.

Chapter 4

External Cavity Lasers

Our research group and others have made use of Ar^+-pumped titanium::sapphire lasers [Anthony93] and commercially available high power fiber-coupled diode arrays [Driehuys96] [Rosen99] [Phillips99] to optically pump Rubidium vapor for purposes of spin-exchange optical pumping. These light sources are not optimal for this application; they are either needlessly narrow and underpowered (Ti::Sapph) or too broad to be efficiently utilized (arrays). An ideal light source would provide high power (e.g. tens of Watts) well matched to the pressure broadened Rb linewidth (17 GHz/amagat). This is the motivation for our work frequency-narrowing high power broad area lasers (BAL's) and diode laser arrays using novel external cavity designs. We have ultimately succeeded in obtaining 16.5 Watts of tunable 85 GHz wide output from a commercially available 40 Watt, 19-element array (Coherent B1-79-40C-19-30-A), and have produced ^{129}Xe polarizations in a 25 ml optical pumping cell roughly 3 times that produced by a 15 Watt fiber-coupled (unnarrowed) array.

4.1 Broad Area Lasers (BALs)

As a first step toward narrowing a diode array, we applied external cavities to single- and dual-stripe BAL's. BAL's we have worked with have had either a single rectangular active region (200 microns by 1 micron) or two such regions separated by a small isolation region. The significant astigmatism inherent to these devices makes accurate collimation by use of noncylindrical lenses (as is customary with lower power devices) impossible. Instead, we used a 0.68 numerical aperture aspheric lens to collimate the fast axis (initially exhibiting a 35° divergence angle), leaving the slow axis slightly divergent. When using a BAL with only one active region, we found it unnecessary to correct for this remaining divergence. A Littrow or Littman-Metcalf [Littman78] oriented 1800 lines/mm holographic diffraction grating provided the frequency-selected feedback to the device. We often added a $\lambda/2$ plate to the cavity, taking advantage of the polarization dependence of the grating efficiency to cut back excessive feedback and maximize narrowed output power [Lotem92].

Applying this design to a Coherent Semiconductor Group 2 W BAL (SS-79-2000C-150-H) yields 1.4 W output with a 40 GHz bandwidth (as measured by a home-built parallel plate Fabry Perot cavity with finesse $\sim$20). This is a significant improvement over the diode's free running bandwidth of 700 GHz. It should be noted that because the output exhibited an irregular lineshape, the bandwidth that we quote is the frequency window containing 64% of the output power. The output frequency tuned smoothly from 792 nm to 798 nm, and though no temperature control and only low-cost commercial mounts were used, the device ran stably for days. We obtained similar results with a 4 W Semiconductor Laser International BAL at 808 nm (SLI-CW-SLD-C1-808-4M-R).

We then turned our attention to a 4W Spectra Diode Labs diode (SDL-2380).

This diode has a 500 μm by 10 μm active region which is actually two active regions separated by an isolation space. The two active regions are indeed isolated, as we found that we could produce two independently tunable, narrow bandwidth beams in a manner analogous to reference [Hsu99] (though with less complexity and more output power at the expense of bandwidth). We collimated the fast axis of the BAL as before with a 0.68 NA aspheric collimating lens. The laser intensity several centimeters from the collimating lens exhibited two distinct lobes, corresponding to the two active regions of the device. We were able to use two 1800/mm holographic diffraction gratings, one intercepting each of the lobes, to narrow and tune each active region independently of the other. Each beam contained approximately 1 Watt of power within a 70 GHz bandwidth. The authors of reference [Wang95] have examined the utility of a lower power dual-wavelength diode laser source for producing TerraHertz radiation.

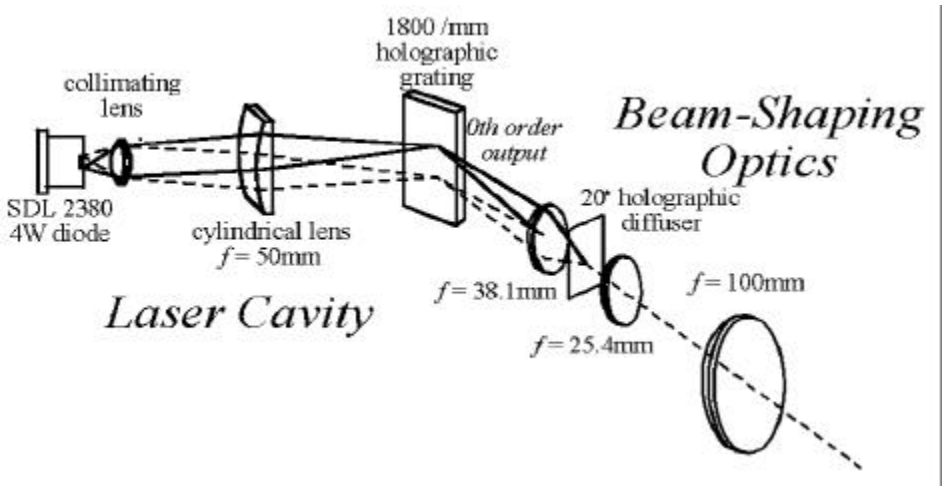

Figure 4.1: External cavity we have applied to narrowing dual-stripe BALs.

Inserting a cylindrical lens into the cavity allows us to narrow and tune both active regions with one grating. The key to this design (see figure 4.1) is the placement of the cylindrical lens. Rather than collimating the laser light, the lens images the diode onto the grating. In this way, the first order diffraction feedback forms an image of the BAL

back on itself with positive magnification (in contrast to the negative magnification that occurs in a standard Littrow cavity). The result is that each of the two active regions is imaged back on itself, rather than on the other. In this way, we have produced a 2.5 Watt output beam with a bandwidth of 70 GHz, tunable over roughly 4 nm (see figure 4.2). The emission of this device is polarized along the fast axis; adding the half-wave plate to the cavity allows us only to increase the feedback, resulting in lower power output with only modest gains in narrowing and tunability.

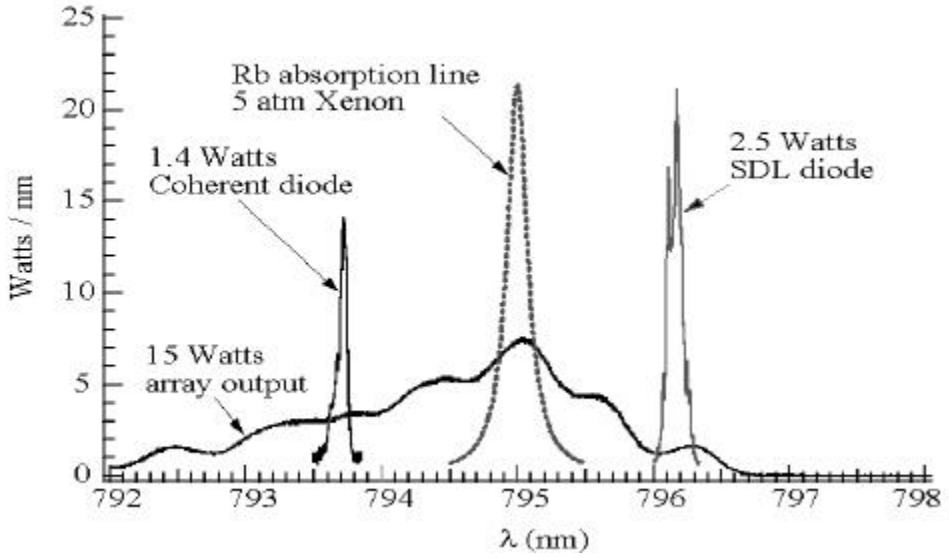

Figure 4.2: Fabry-Perot spectra of frequency-narrowed BALs.

We compared the optical pumping performance of the frequency narrowed 4 Watt diode to a commercially available 15 Watt diode array (OPC-A015-FCPS, OptoPower Corporation). The optical pumping cell is a sealed uncoated 4 cm diameter Pyrex sphere with a small stem. It contains 1.3 amagats of natural abundance xenon, 50 Torr of nitrogen quenching gas, and a small amount of Rb metal. It is located in a forced air oven with AR coated windows, and carefully centered in a pair of 1 meter diameter Helmholtz coils which provide the DC field.

We used the custom pulsed NMR method described in Chapter II to measure the polarization of the ^{129}Xe as a function of the oven temperature. In order to make a valid comparison, each of the two laser sources was used to illuminate the cell with a uniform 2 cm diameter beam. The irregular beam profile of the narrowed diode necessitated the use of the beam-shaping optics shown in figure 4.1. Losses at the beam-shaping optics lead to only 1.4 Watts actually being delivered to the cell. Nevertheless, the maximum polarization achieved with the 1.4 W narrow band laser is nearly identical to that achieved with the 15 W array. Removing the beam shaping optics results in even higher xenon polarizations, as the entire 2.5 Watts is delivered to the cell. The narrow band 2.5 W device then produces polarizations 40% greater than that of the 15 W array.

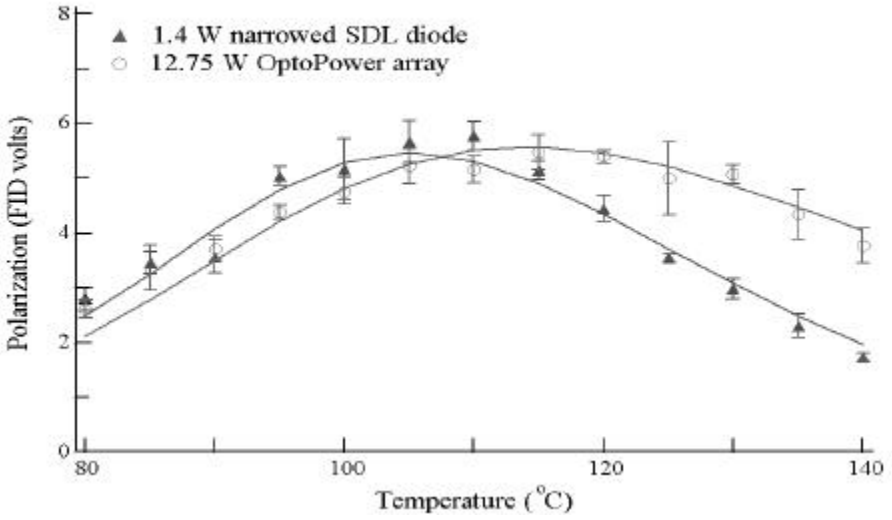

Figure 4.3: Relative ^{129}Xe polarization induced using frequency-narrowed BAL as compared to 15 Watt unnarrowed array.

4.2 Diode Laser Arrays

The arrays we have narrowed consist of multiple BALs arranged in an approximately straight line along the individual diodes' slow axes. The inactive regions between the elements are larger than the elements themselves for adequate heat removal, making the fill factor (ratio of active region to inactive region along the length of the array) typically only 30%. The output from an array typically has a 10° divergence angle along the length of the array (slow axis) and a diffraction-limited 40° divergence angle perpendicular to the array (fast axis). These features, coupled with the 1 cm length of the array, lead to difficulty collecting output light and providing efficient feedback (even leading some to state that it is impossible [Zerger00]). We were the first group to overcome these difficulties and realize an external cavity diode laser array (ECDLA).

Our external cavity (figure 4.4) uses a fast cylindrical microlens (Doric Lenses) to collimate the fast axis of the array. An afocal telescope images the slow axis of the array onto a Littrow-oriented diffraction grating with magnification M while expanding the collimated fast axis by the same factor M. The frequency-selected first order feedback from the grating is then imaged back onto the elements, while the output is taken from the zeroth order reflection off the grating.

The two dominant contributions to the bandwidth of our cavity are slow axis divergence angle and array "smile". "Smile" refers to irregular curvature of the array induced during the manufacturing process. We have measured the smile of several arrays in the following manner: We first collimated the fast axis using a 0.73 mm focal length cylindrical microlens. We then used a 75.6 mm cylindrical lens to image the slow axis onto a sheet of 2 mm ruled graph paper at a distance of 58 cm from the array. We photographed the image with a digital camera (figure 4.5). The amount of array smile is then approximately equal to the amount of smile in the photos times

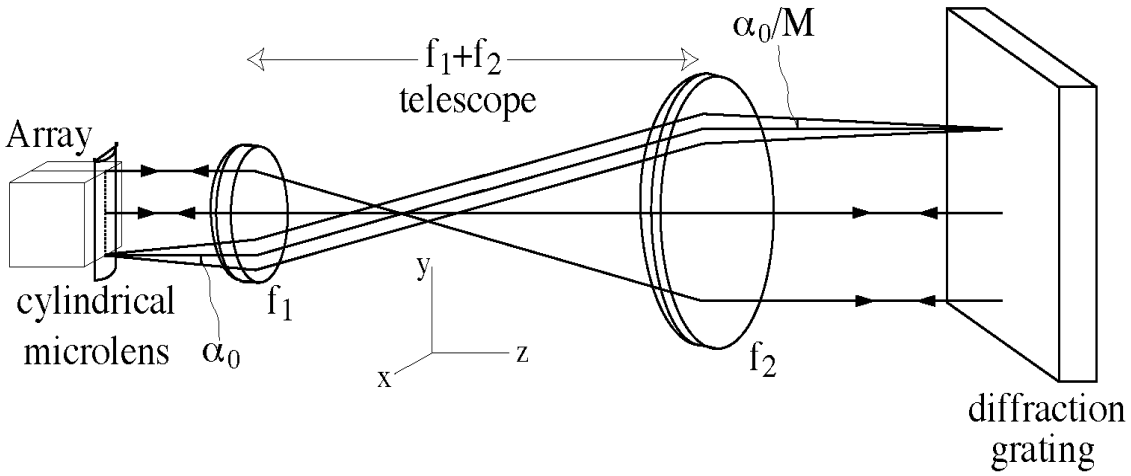

Figure 4.4: Afocal imaging cavity for narrowing arrays.

the ratio of collimating lens focal length to image distance. For our optics, this ratio is 0.73/580 = .00126, yielding an array smile of approximately 8.8 μm for the IMC Silver Bullet and $\sim$1 μm for the hand-picked IMC Silver Bullet. Array smile (spread in position x_i with respect to the center line of the cavity) is converted by the collimating microlens (focal length f_c) to a spread in angles $\phi_i = x_i/f_c$ of the collimated light from each element i.

For light striking the grating with direction $\hat{z}\cos\alpha\cos\phi + \hat{y}\sin\alpha + \hat{x}\sin\alpha\sin\phi$ with respect to the optical axis, the Littrow feedback condition can be derived with the aid of figure 4.6. That figure shows two optical rays incident on a diffraction grating, both with angle of inclination α. The first ray strikes a groove of the grating at point F. The second ray strikes an adjacent groove of the grating at B. As given by the usual derivation of the Littrow condition [Hecht], the projection on the xz-plane of the extra distance the second ray travels to the grating is given by $d\sin(\theta - \phi)$, where angle θ is the angle between the grating normal and the optical axis. Referring to figure 4.6, the

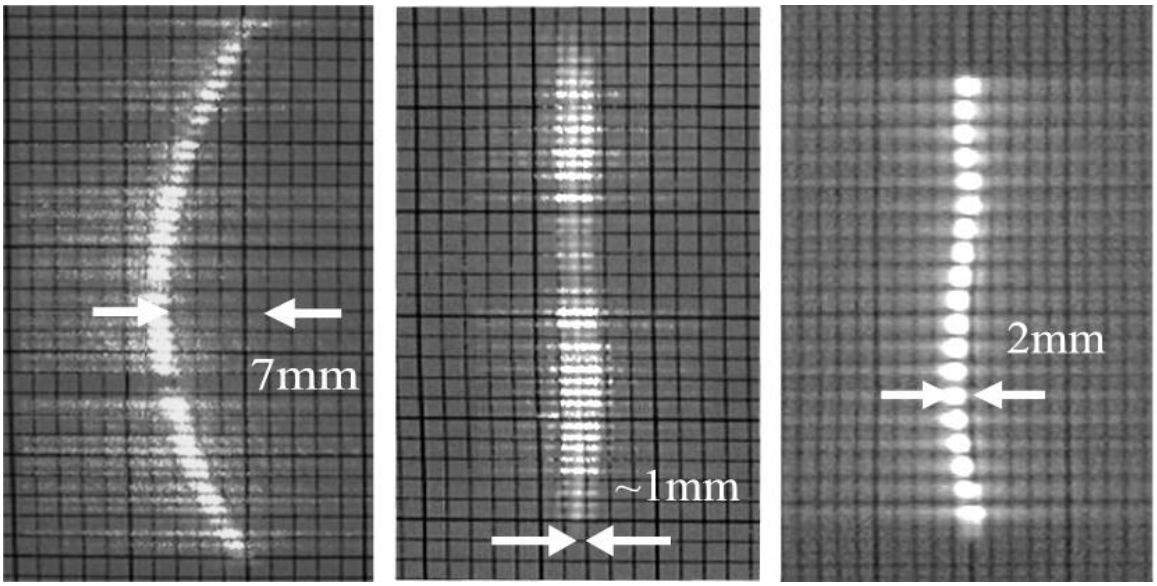

Figure 4.5: Photographs showing "smile" of (left to right) stock IMC Silver Bullet, hand picked IMC Silver Bullet, and hand picked Coherent 40 Watt array.

optical path length difference, Δ(o.p.l.), is given by

$$\Delta(\text{o.p.l.}) = DF - 2BC = \lambda. \tag{4.1}$$

Length AB, as mentioned above, is given by reference [Hecht]:

$$AB = d\sin(\theta - \phi), \tag{4.2}$$

so we can immediately write

$$BC = \frac{d\sin(\theta - \phi)}{cos\alpha} \tag{4.3}$$

and

$$EF = 2AC = 2d\sin(\theta - \phi)\tan\alpha. \tag{4.4}$$

It then follows that

$$DF = EF\sin\alpha = 2d\sin(\theta - \phi)\frac{\sin^2\alpha}{\cos\alpha}. \tag{4.5}$$

The Littrow condition is then

$$\lambda = 2d\sin(\theta - \phi)\cos\alpha, \tag{4.6}$$

or

$$\delta\lambda/\lambda_0 \approx -\alpha^2/2 - \phi\cot\theta \tag{4.7}$$

where $\lambda_0 = 2d\sin\theta$, $\delta\lambda = \lambda - \lambda_0$, and the angles α and ϕ are assumed small. Thus spreads in α (from the divergence of the light emitted from the laser) and ϕ (from smile) both result in broadening of the laser spectrum.

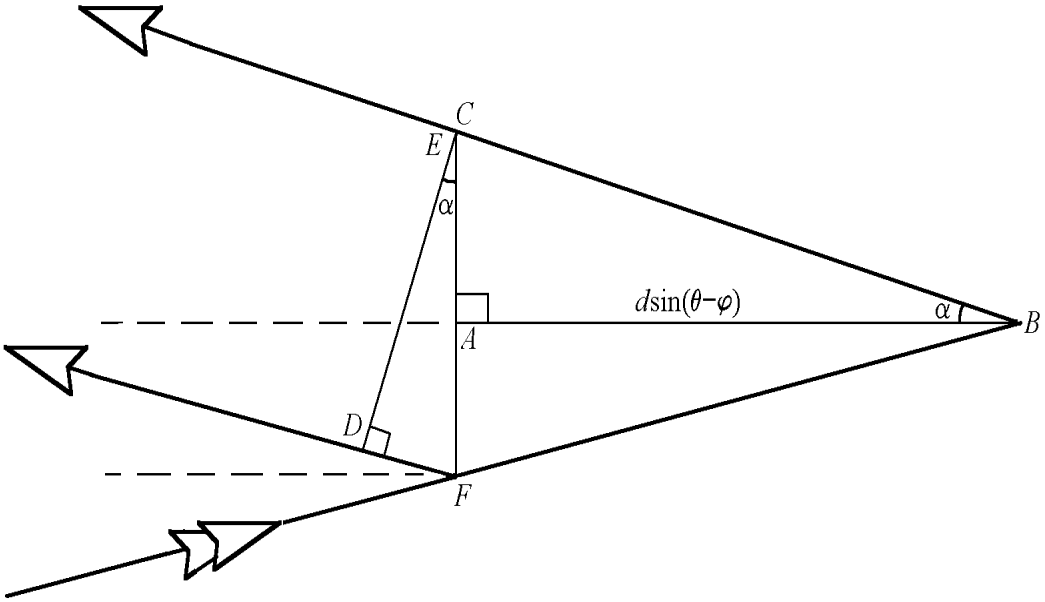

Figure 4.6: Two optical rays with angles of inclination α incident on adjacent grooves of a diffraction grating . (Refer to figure 4.4 for orientation.)

The telescope reduces the angular spread in the $\hat{y}$-direction from α_0 at the laser to $\alpha = \alpha_0/M$ at the grating. From equation. 4.7, this reduces the broadening by a factor of M^2. More importantly, the afocal nature of the telescope means that the angular spread of rays at the grating from on- *and off*-axis elements is symmetrically centered around zero. We tried a number of imaging methods with finite focal length

lens systems, and were unable to reduce the linewidth below 150 GHz.

The telescope also reduces the spread in angles resulting from smile to $\phi = x/Mf_c$, where x represents the amount of smile. From equation 4.7, the resulting laser linewidth due to smile is

$$\frac{\delta\lambda}{\lambda} = \frac{x\cot\theta}{Mf_c}. \tag{4.8}$$

Thus in order to minimize the contribution of smile to the linewidth, it is desirable to use a long f_c, a large magnification, and large diffraction angle. However, because the slow axis is imaged onto an angled grating, we have found that large magnification (with correspondingly large depth of focus) is the preferred means to reducing cavity linewidth. In practice, we have used the largest magnification possible, 5×, being limited by the size of inexpensive diffraction gratings (5 cm × 5 cm).

Our best ECDLA results have been achieved using a hand-picked low smile 20 Watt 46-element IMC array (IMC ARR26C020W0795). IMC's manufacturing process produces an array with output polarized with electric field vector along the length of the array. The diffraction grating is less efficient with this polarization, making it possible to couple out a greater fraction of narrowed light. In addition, IMC was able to supply us with the flattest (lowest smile) array we have worked with (see figure 4.5), with smile less than 1 micron. This array ran freely at 801.2 nm, with a 1.4 nm linewidth. We used a 0.73 mm focal length cylindrical lens and a 4× telescope constructed from a 25.4 mm diameter 50 mm focal length achromat and a 50.8 mm diameter 200mm focal length plano-convex lens. A 50 mm × 50 mm, 2400 lines/mm holographic grating provided the feedback to the array. In this configuration, approximately 80% of the array emission is coupled out of the cavity, though with only 68% of that output frequency-narrowed. We therefore included a $\lambda/2$ plate in the cavity in order to increase the feedback to the array slightly to obtain maximum narrowed output power. In this way, the ECDLA puts 66% of the array's emission into a frequency-narrowed output.

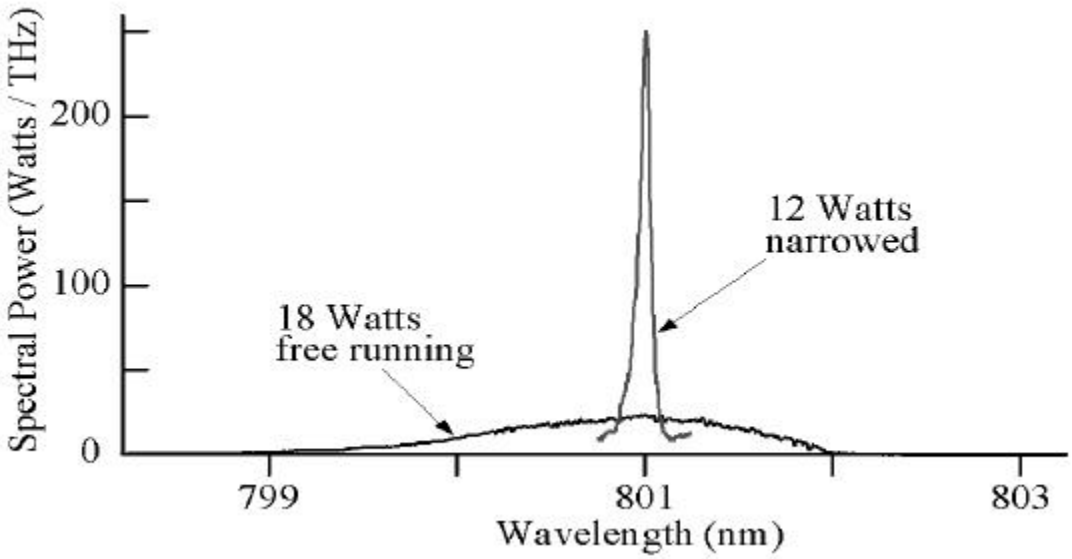

Figure 4.7: Frequency-narrowed array output vs. the output of the same array without external cavity.

We measured the linewidth of the ECDLA output using a home-built parallel plate Fabry-Perot cavity with finesse ∼20. Care was taken to measure the total array linewidth as opposed to the linewidth of a few select elements. The output from the grating was focused onto a ground glass diffuser. The diffused light was then passed through a second ground glass diffuser before then being sent through the Fabry-Perot etalon. (Again, we quote the linewidth as the frequency window which contains 64% of the power.) Figure 4.7 shows the typical output of this ECDLA as compared to the free-running output. In order to keep intracavity power below the array's specified rating (20 Watts at 30 Amps), we have run the array at only 27 Amps (18 Watts output).

We have also demonstrated the tunability of the ECDLA. Figure 4.8 illustrates the approximately 4 nanometers of tuning that we are able to produce by changing the angle of the feedback grating. This, when combined with temperature tuning, allows

our ECDLA to reach wavelengths 3 to 4 nanometers away from its free-running peak without significant loss of narrowed output power.

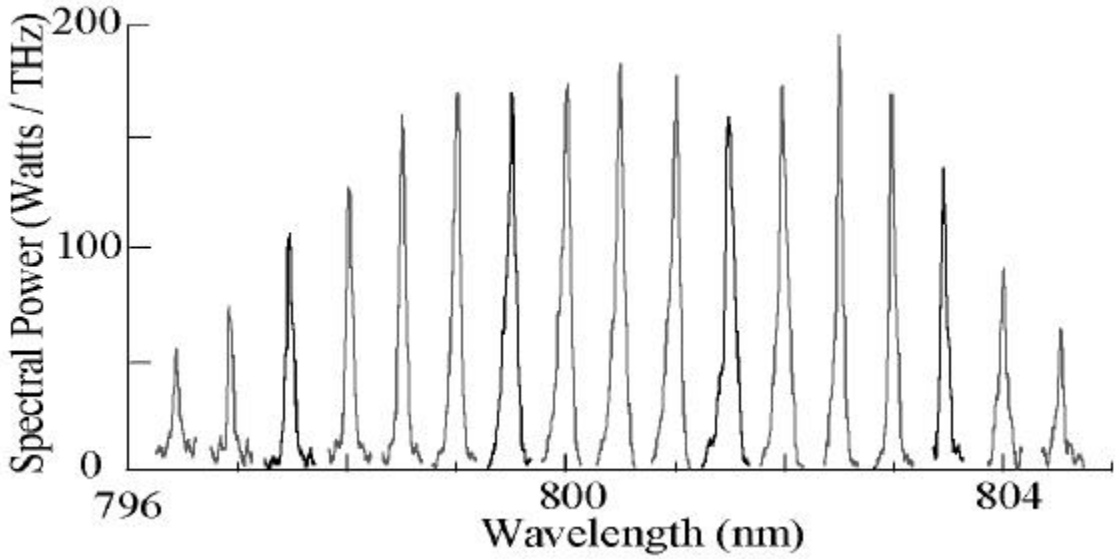

Figure 4.8: Tuning the ECDLA via grating rotation. The unnarrowed portion of the spectrum has been subtracted off in each case.

For producing polarized ^{129}Xe, we constructed an ECDLA using a hand-picked 40 Watt, 19 element Coherent Semiconductors Group array (part # B1-79-40.0C-19-30-A). This array exhibited a 1.5 nanometer wide free-running peak centered at 796.4 nanometers. Coherent's diode arrays emit light with polarization along the fast axis of the array. Without an intracavity $\lambda/2$ plate, only 10% of the light emitted by the array is coupled out of the cavity. Indeed, setting the $\lambda/2$ plate for maximum output yields only 66% of the array emission in the ECDLA output. The smile of this array was somewhat larger than that of the IMC array, at 2.5 microns (see figure 4.8). We constructed the ECDLA cavity from a 1.5 mm diameter graded index microlens (f =1.027 mm), a 25.4mm diameter, 50mm focal length achromat, and a 100mm diameter, 250mm focal length biconvex lens. These parameters yield a 60 GHz cavity bandwidth

due to smile. We were able to obtain 16.5 Watts output power in 86 GHz linewidth (figure 4.9) when providing the array with 30 Amps (corresponding to an output power of approximately 30 Watts). We then compared the ^{129}Xe polarization produced by our ECDLA to that produced by a commercially available 15 Watt fiber-coupled diode array (Optopower Corporation OPC-A015-FCPS).

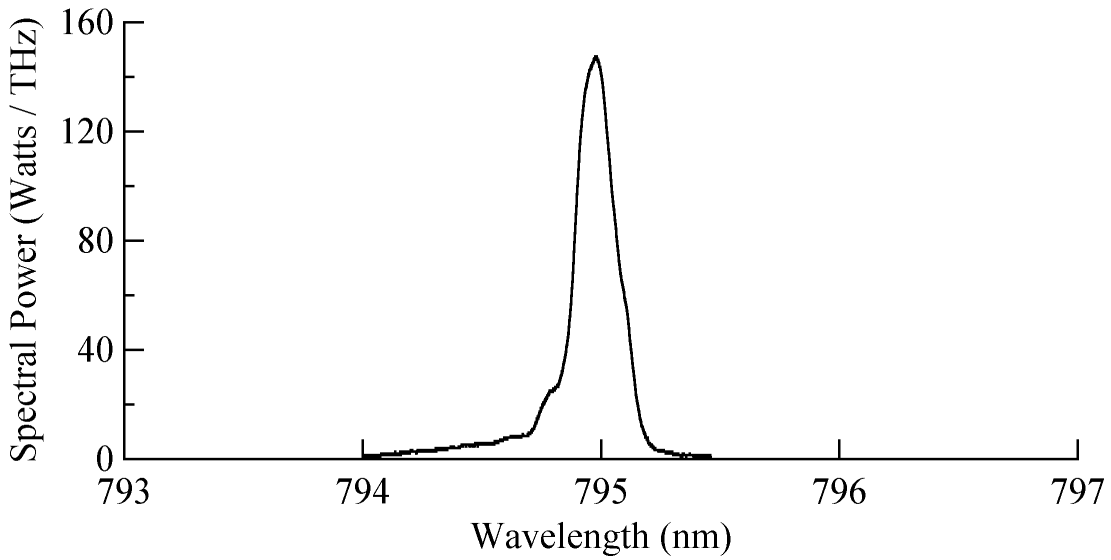

Figure 4.9: Best output obtained from Coherent array. The peak shown contains 16.5 Watts and has FWHM = 86 GHz.

Several additions to the ECDLA allowed efficient coupling of the output to the optical pumping cell. In order that the output angle of the ECDLA did not change with grating angle (tuning), we attached a mirror to the grating mount such that the mirror always has a fixed orientation relative to the grating itself. In this way, changing the tuning angle only translates the output a small amount, rather than changing its angle. A 60mm tall, 200mm focal length cylindrical lens immediately after the mirror collected the (slowly diverging) slow axis of the output. The focal length of this lens was chosen to provide a 5mm tall spot size in its Fourier plane (to match the 5mm

wide collimated fast axis). This 5mm x 5mm square was then imaged onto the cell via a 63 mm focal length plano-convex lens with magnification 4 in order to provide a 2cm x 2cm area of illumination. A $\lambda/4$ plate imposed the desired circular polarization upon the beam.

We used the ECDLA output to optically pump the cell used previously to measure the performance of our frequency-narrowed BAL. ^{129}Xe polarization was again measured as a function of cell (oven) temperature for each source. The ECDLA results have been added to the graph of the previous results to produce figure 4.10. We see that the ECDLA produces approximately 3 times as much polarization as does the fiber-coupled array. The ECDLA output for these measurements consisted of a $\approx$130 GHz wide peak containing 14 Watts superimposed on the unnarrowed 7 Watts of remaining power. The theory curve in figure 4.10 was produced assuming a 1.5 nm wide gaussian lineshape for the unnarrowed light and a 130 GHz wide lorentzian lineshape for the narrowed peak. The relatively poor agreement with the model may be due to the relaxivity of the Pyrex walls degrading over time.

The ECDLA we have demonstrated is clearly more ideally matched to the special constraints of spin-exchange optical pumping than are any commercially available light sources. Its features include low cost, high power output, and bandwidth well matched to the pressure-broadened rubidium linewidth. We expect that its full potential will be realized by producing highly polarized ^{129}Xe at lower pressures and temperatures than is currently feasible using unnarrowed diode arrays.

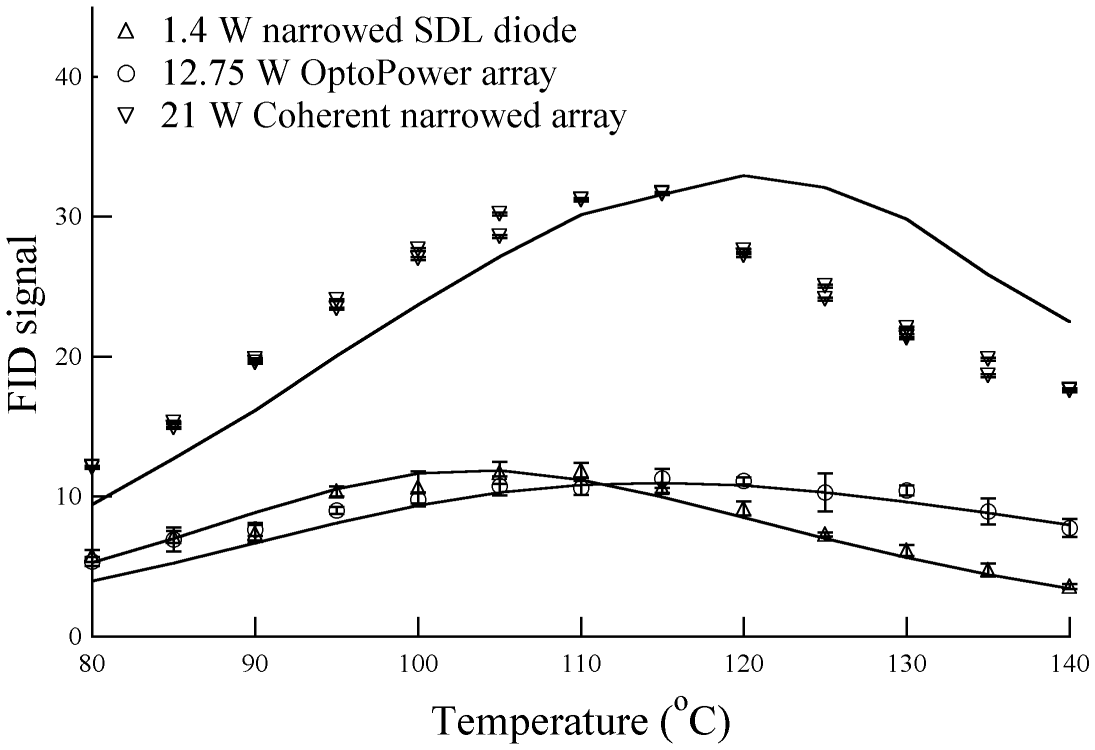

Figure 4.10: Relative ^{129}Xe polarization induced by frequency-narrowed array compared to that induced by other light sources

Chapter 5

Rate Measurements

Though spin-exchange optical pumping of ^{129}Xe has been a widely known laboratory technique for over twenty years [Grover78], it has only recently been employed in the interest of producing large quantities of hyperpolarized gas for practical applications [Driehuys96]. The performance of a practical spin exchange optical pumping system must be evaluated in terms of both the final nuclear polarization of the noble gas delivered as well as the speed (liters per second) with which it can be delivered. From chapter 1, the polarization of the ^{129}Xe is given by

$$2\langle K_z\rangle = 2\langle S_z\rangle\left(\frac{\Gamma_{SE}}{\Gamma_{SE}+1/T_1}\right) \tag{5.1}$$

$$= \left(\frac{R_p}{R_p+\Gamma}\right)\left(\frac{\Gamma_{SE}}{\Gamma_{SE}+1/T_1}\right), \tag{5.2}$$

while the rate at which it is produced is given by $(\Gamma_{SE}+1/T_1)V[\mathrm{Xe}]/[\mathrm{G}]$. As in chapter 1, Γ_{SE} is the rate at which ^{129}Xe acquires spin from the Rb, Γ is the rate at which Rb loses spin, R_p is the optical pumping rate per Rb atom, and $1/T_1$ is the ^{129}Xe relaxation rate. In addition, V is the volume of the spin exchange cell and [G] denotes total gas density. It is clear that in order to accurately model the performance of a gas polarizer, we must have accurate values for both Γ_{SE} and Γ, and we must also have

some information about how these factors change with temperature, gas density, and gas composition.

High power high bandwidth lasers have driven the recent trend toward higher temperatures, pressures, and lean mixtures of xenon [Driehuys96]. Unfortunately, this trend has made much of the excellent early work in this field [Bouchiat72] [Cates92], done at relatively low temperatures, pressures, and with different gas compositions, perhaps somewhat less useful for predicting the performance of practical spin-exchange systems [Shah00]. For this reason, we have undertaken to extend that work into higher temperature and pressure regimes.

We find that while the Rb spin loss rate is nearly entirely due to binary Rb-Xe collisions, the spin exchange rate is dominated by spin exchange during the lifetimes of Rb-Xe van der Waals molecules. We have measured the temperature and gas density dependences of both Γ and Γ_{SE}, and have found a surprisingly large temperature dependence to the van der Waals molecule spin exchange rate which has dramatic implications for modeling hyperpolarized ^{129}Xe gas production systems.

I have described the spin-exchange system we have used for these measurements in Chapter 2. The commercially premixed gas composition we have studied (1% natural abundance Xe, 1% N_2, balance ^{4}He, Spectra Gases) was chosen for its practical relevance. It reflects the composition used in much recent work [Shah00] [Driehuys96]. We experimentally verified the Xe fraction in the gas to better than 5% by freezing a known density of the total mixture in a cell with liquid N_2, pumping out the unfrozen gas, warming, and remeasuring the density. We have measured the Rb loss rates and spin-exchange rates in this mixture at several temperatures between 80°C and 120°C, and over densities ranging from 0.006 to 3.2 amagats (1 amagat = $2.69 \times 10^{19}/\text{cm}^3$ is the density of an ideal gas at 0°C and 1 atmosphere of pressure).

5.1 Rb Spin Loss Rate

The dominant collisional processes affecting Rb spin loss are Rb-Rb spin-exchange collisions, Rb-Xe binary collisions, and formation and breakup of Rb-Xe van-der-Waals molecules. The Rb-Rb spin-exchange collisions to a good approximation conserve the spin-angular momentum, but redistribute it between nuclear and electron spins. It is nonetheless extremely important, as it is this redistribution of angular momentum which, when much faster than all spin loss processes present, leads to a single spin-temperature for all alkali atoms [Anderson60]. Under this condition, both stable Rb isotopes (^{85}Rb and ^{87}Rb) share the same slowest spin decay rate, making analysis of measured decay transients much simpler (compare subsection 5.1.2 to subsection 5.1.1).

Rb-Xe binary collisions in principle lead to loss of Rb spin polarization $\langle F_z \rangle$ to either the ^{129}Xe nuclear spin polarization $\langle K_z \rangle$ or to the angular momentum of the colliding pair, $\mathbf{N}$. The Fermi contact interaction, $\alpha \mathbf{K} \cdot \mathbf{S}$, is responsible for the spin exchange, and tends to equalize $\langle K_z \rangle$ and $\langle S_z \rangle$, the Rb electron polarization, while the spin-rotation interaction, $\gamma \mathbf{N} \cdot \mathbf{S}$, reduces Rb polarization independently of $\langle K_z \rangle$. We can describe the effects of these two interactions respectively in terms of two simple velocity-averaged cross sections, σ_{se} and σ_{sr}:

$$\frac{d}{dt}\langle F_z \rangle = [\mathrm{Xe}]\Big(\langle \sigma_{se} v \rangle \left(\langle S_z \rangle - \langle K_z \rangle \right) - \langle \sigma_{sr} v \rangle \langle S_z \rangle \Big). \tag{5.3}$$

For this work, we are careful to maintain low ^{129}Xe polarization. We therefore describe the loss of Rb spin via all binary collisional processes by a single velocity-averaged rate coefficient $\langle \sigma v \rangle = \langle \sigma_{se} v \rangle + \langle \sigma_{sr} v \rangle$:

$$\frac{d}{dt}\langle F_z \rangle = [\mathrm{Xe}] \langle \sigma v \rangle \langle S_z \rangle. \tag{5.4}$$

Rb spin relaxation in van der Waals molecules is more complex, depending strongly on the average correlation time of Rb-Xe van der Waals molecules in the spin-exchange

cell. The important time scales here are the relatively long time scale set by the spin rotation interaction, $\gamma \mathbf{N} \cdot \mathbf{S}$, and the shorter time scale set by the Rb hyperfine interaction, $A\mathbf{I} \cdot \mathbf{S}$ Together, these two characteristic timescales divide the range of possible van der Waals molecule correlation times into three regimes [Happer84]. Throughout this work, we have made the assumption that the correlation time for the spin rotation interaction is equal to the correlation time for the hyperfine interaction, denoting them both by a single variable, τ_c.

In the "very short" lifetime limit, defined by

$$\left(\frac{A\tau_c(2I+1)}{2\hbar}\right) \ll 1, \tag{5.5}$$

molecular formation and breakup is sudden with respect to both the spin rotation and hyperfine interactions. In particular, it is sudden with respect to the Rb nuclear polarization, and transitions can occur between $\Delta f = 0, \pm 1$ hyperfine levels, where $f = I \pm \frac{1}{2}$.

In the long lifetime limit, τ_c is long compared to both the hyperfine interaction time $\hbar/A$ and the spin rotation time $\hbar/\gamma$:

$$\left(\frac{\gamma\tau_c}{(2I+1)\hbar}\right)^2 \gg 1. \tag{5.6}$$

$\mathbf{S}$ may precess through large angles due to both the spin rotation and hyperfine interactions during the molecular lifetime. Because $\mathbf{S}$ is strongly coupled to $\mathbf{I}$ during the molecular lifetime, only "F-damping" transitions, which leave the total Rb angular momentum quantum number unchanged ($\Delta f = 0$) may occur. ($\Delta f = \pm 1$ transitions are correspondingly termed "S-damping".)

In the intermediate regime (often called the "short lifetime limit") [Happer84], molecular formation and breakup is sudden with respect to the spin rotation interaction, but $\mathbf{S}$ may still precess about $\mathbf{I}$ many times during the molecular lifetime. Once again, only F-damping transitions may occur.

van der Waals molecules inducing F-damping transitions relax the total Rb spin of isotope i, $\langle F_{iz}\rangle$, as per the following rate equation (where we have taken into account the ^{129}Xe nuclear spin $K = \frac{1}{2}$) [Happer84]:

$$\left.\frac{d\langle F_{iz}\rangle}{dt}\right|_{FD} = -\frac{1}{T_A}\left[\frac{2}{3}\left(\frac{\phi_\gamma}{2I_i+1}\right)^2\langle F_{iz}\rangle + \eta_{129}\left(\frac{\phi_\alpha}{2I_i+1}\right)^2\left(\frac{\langle F_{iz}\rangle}{2} - \langle F_i^2 - F_{iz}^2\rangle\langle K_z\rangle\right)\right]. \tag{5.7}$$

S-damping van der Waals molecules yield a similar rate equation [Happer84]:

$$\left.\frac{d\langle F_z\rangle}{dt}\right|_{SD} = -\frac{1}{T_A}\left[\frac{2}{3}\left(\phi_\gamma\right)^2\langle S_z\rangle + \eta_{129}\left(\phi_\alpha\right)^2\left(\frac{\langle S_z\rangle}{2} - \frac{\langle K_z\rangle}{2}\right)\right]. \tag{5.8}$$

T_A is the formation rate of van der Waals molecules per Rb atom, η_{129} is the isotopic fraction of ^{129}Xe ($\eta_{129} = 0.264$ in our natural abundance gas mixture), and the angles ϕ_γ and ϕ_α are, respectively, the rms precession angles of the Rb electron spin around the molecular spin and the Rb nuclear spin:

$$\phi_\gamma = \frac{\gamma N \tau_c}{\hbar}, \tag{5.9}$$

and

$$\phi_\alpha = \frac{\alpha \tau_c}{\hbar}. \tag{5.10}$$

We follow Cates *et al.* [Cates92] in defining a rate Γ_{vdW} to parameterize the effects of van der Waals molecules:

$$\Gamma_{vdW} = \left(\frac{2\phi_\gamma^2/3 + \eta_{129}\phi_\alpha^2/2}{T_A}\right). \tag{5.11}$$

Γ_{vdW} can be thought of as the "very short" lifetime van der Waals molecule contribution to the relaxation rate of an alkali atom with arbitrary I (or as the "short" lifetime van der Waals molecule contribution to the relaxation rate of a fictitious alkali isotope with $I = 0$). Γ_{vdW} contains density dependences in the factor $1/T_A$ as well as in the ϕ's, so it is helpful to write equation 5.11 in terms of gas densities. We can first use

detailed balance to rewrite $1/T_A$ in terms of gas densities and the chemical equilibrium coefficient, $\mathcal{K}$:

$$\frac{1}{T_A} = \frac{[\mathrm{RbXe}]}{[\mathrm{Rb}]\tau} \tag{5.12}$$

$$= \frac{\mathcal{K}[\mathrm{Xe}]}{\tau}, \tag{5.13}$$

where τ is the van der Waals molecule lifetime. We also use the parameter $x = \gamma N/\alpha$ [Zeng85] to write

$$\Gamma_{vdW} = \frac{\mathcal{K}[\mathrm{Xe}]}{\tau}(2/3 + \eta_{129}/2x^2)\left(\frac{\gamma N \tau_c}{\hbar}\right)^2 \tag{5.14}$$

$$= (2/3 + \eta_{129}/2x^2)\mathcal{K}[\mathrm{G}]_0 \frac{\gamma N}{\hbar}\frac{[\mathrm{Xe}]}{[\mathrm{G}]}, \tag{5.15}$$

where in the last step, we have assumed that collisions violent enough to reorient **N** or **I** are sufficient to break up the van der Waals molecule [Happer84]. Therefore we set the correlation time τ_c equal to the van der Waals molecular lifetime, τ. $[\mathrm{G}] = [\mathrm{He}] + [\mathrm{N_2}] + [\mathrm{Xe}]$ is the total gas density, while $[\mathrm{G}]_0$ is a characteristic density, defined below, which depends upon the composition of the gas. Γ_{vdW} can be seen to be gas composition dependent ($[\mathrm{Xe}]/[\mathrm{G}]$, $[\mathrm{G}]_0$), but density *independent* for a particular gas mixture. We note here that throughout this work we quote gas density rather than the (more ambiguous) gas pressure, as questions about to which temperature a quoted pressure is referenced abound in the spin exchange optical pumping literature.

We describe the fractions of van der Waals molecules inducing S-damping vs. F-damping transitions in terms of the (Rb isotope dependent) parameters f_1 and f_0, where [Appelt98]

$$f_1 = \frac{1}{1 + (\omega_{hf}\tau)^2} = \frac{1}{1 + ([\mathrm{G}]_1/[\mathrm{G}])^2} \tag{5.16}$$

and

$$f_0 = \frac{1}{1 + \left(\frac{\omega_\gamma \tau}{2I+1}\right)^2} = \frac{1}{1 + ([\mathrm{G}]_0/[\mathrm{G}])^2/(2I+1)^2}. \tag{5.17}$$

$[\mathrm{G}]_0$ and $[\mathrm{G}]_1$ are characteristic total gas densities defined via

$$\omega_{hf,i}\tau = [\mathrm{G}]_{1,i}/[\mathrm{G}] \tag{5.18}$$

$$\frac{\gamma N \tau}{\hbar} = [\mathrm{G}]_0/[\mathrm{G}]. \tag{5.19}$$

Physically, f_1 may be thought of as the fraction of van der Waals molecules whose lifetimes are "very short", ($\omega_{hf}\tau \ll 1$), while $(1-f_0)$ can similarly be thought of as the fraction of van der Waals molecules whose lifetimes are "long", ($\omega_\gamma \tau/(2I+1) \gg 1$). $[\mathrm{G}]_1$, then, marks the "short" to "very short" transition, while $[\mathrm{G}]_0$ marks the "long" to "short" transition. The authors of reference [Wu85] have measured $\gamma N/h = 135 MHz$. This, combined with the Rb hyperfine frequencies ($\omega_{hf,85} = 2\pi \times 3.0357$ GHz, $\omega_{hf,87} = 2\pi \times 6.8347$ GHz) suggests that the two transitions are well separated.

With these definitions in place, and assuming that we are careful to maintain low ^{129}Xe polarization ($\langle K_z \rangle \approx 0$), we can write a simple expression for the total spin relaxation of Rb isotope i:

$$\frac{d\langle F_{iz}\rangle}{dt} = -(f_{0,i} - f_{1,i})\Gamma_{vdW}\frac{1}{(2I_i+1)^2}\langle F_{iz}\rangle - f_{1,i}\Gamma_{vdW}\langle S_z\rangle - [\mathrm{Xe}]\langle\sigma v\rangle\langle S_z\rangle, \tag{5.20}$$

valid for $\omega_{hf} \gg \omega_\gamma/(2I_i+1)$. The three terms arise respectively from F-damping van der Waals molecules, S-damping van der Waals molecules, and (S-damping) binary collisions.

5.1.1 High Temperature

The Rb isotopic dependence of equation 5.20 leads in general to four different relaxation rates in a Rb vapor [Appelt98]. However, if Rb-Rb spin exchange is sufficiently rapid compared to S-damping and F-damping relaxation rates ($\Gamma_{se} \gg \Gamma_{FD}, \Gamma_{SD}$), the polarization of the total Rb vapor (both isotopes) may be described by a single spin-temperature [Anderson60]. In this limit, we can relate the total Rb spin to the electron

spin via the "paramagnetic coefficient", ϵ_i [Happer84]:

$$\langle F_{iz}\rangle = (1+\epsilon_i)\langle S_z\rangle, \tag{5.21}$$

where

$$\epsilon_i = 2\langle I_i^2 - I_{iz}^2\rangle. \tag{5.22}$$

In the low polarization limit, this reduces to

$$\epsilon_i = \frac{4}{3} I_i(I_i+1). \tag{5.23}$$

.

We can then perform an isotopic average of equation 5.20 to write a simple form for the expected spin-temperature fundamental relaxation rate of a Rb vapor:

$$\frac{d\langle S_z\rangle}{dt} = \tfrac{1}{1+\bar{\epsilon}} \textstyle\sum_{85,87} \eta_i \frac{d\langle F_{iz}\rangle}{dt} \tag{5.24}$$

$$= -\tfrac{1}{1+\bar{\epsilon}}\Big(\textstyle\sum_{85,87} \eta_i \Gamma_{vdW}\Big[(f_{0,i}-f_{1,i})\frac{(1+\epsilon_i)}{(2I_i+1)^2} + f_{1,i}\Big] + [\mathrm{Xe}]\langle\sigma v\rangle\Big)\langle S_z\rangle \tag{5.25}$$

$$= -\Gamma_0\langle S_z\rangle \tag{5.26}$$

where $\bar{\epsilon} = \eta_{85}\epsilon_{85}+\eta_{87}\epsilon_{87}$. The sum over ^{85}Rb ($\eta_{85}=0.72$, $I_{85}=\frac{5}{2}$) and ^{87}Rb ($\eta_{87}=0.28$, $I_{87}=\frac{3}{2}$) yields

$$\Gamma_0 = (0.0234 f_{0,85}+0.00972 f_{0,87}+0.0432 f_{1,85}+.0162 f_{1,87})\Gamma_{vdW}+0.0926[\mathrm{Xe}]\langle\sigma v\rangle. \tag{5.27}$$

Our full high temperature fitting function is

$$\Gamma = \Gamma_0 + \Gamma_{corr} + \gamma_{inv}/[\mathrm{G}], \tag{5.28}$$

where, for the analysis of our data, we have included Γ_{corr}, the first order (Γ_{vdW}/Γ_{se}, Γ_{bin}/Γ_{se}) corrections to Γ_0 (see Appendix A):

$$\Gamma_{corr} = -0.0449\Gamma_{bin}^2/\Gamma_{se} +$$

$$+\Big(-0.0483 f_{1,85} - 0.0331 f_{1,87} + 0.0067 f_{0,85} - 0.0151 f_{0,87}\Big)\Gamma_{bin}\Gamma_{vdW}/\Gamma_{se} +$$
$$+\Big(-0.0238 f_{1,85}^2 - 0.0127 f_{1,87}^2 + 0.00497 f_{1,87} f_{0,85} - 0.000933 f_{0,85}^2 -$$
$$-0.00145 f_{1,85} f_{1,87} - 0.000609 f_{0,85} f_{1,85} + 0.00137 f_{0,87} f_{1,85} - 0.0112 f_{1,87} f_{0,87} +$$
$$+0.0042 f_{0,85} f_{0,87} - 0.00473 f_{0,87}^2\Big)\Gamma_{vdW}^2/\Gamma_{se}. \tag{5.29}$$

Γ_{corr} represents the deviation of our system from spin-temperature equilibrium, and yields a $\approx$5% correction at the highest gas densities studied. Fluctuations in Γ_{corr} due to vapor pressure fluctuations dominate the experimental errors.

We also include a fit parameter, γ_{inv}, in order to include an inverse pressure dependent relaxation rate. Physically, this parameter represents Rb spin loss both through diffusion to the cell walls and through Rb-Rb singlet molecules. We can estimate the magnitude of the diffusion contribution to this term through solving the diffusion equation for our cylindrical cell geometry with the boundary conditions of perfectly relaxing walls ($\langle F_z \rangle = 0$ at the walls).

$$\frac{d\langle F_z \rangle}{dt} = D\nabla^2\langle F_z \rangle - \Gamma\langle F_z \rangle \tag{5.30}$$

Keeping only the first longitudinal and first radial mode yields a diffusion dependent wall relaxation rate [Wagshul94]

$$\Gamma_{dif} = \left(\frac{x_{01}^2}{R^2} + \frac{\pi^2}{L^2}\right) D, \tag{5.31}$$

where R and L are the cell radius and length, and $x_{01} = 2.405$ is the first zero of the Bessel function J_0. Our cell dimensions yield a diffusion dependent loss term

$$\Gamma_{dif} = (1.61\text{cm}^{-2}) D_0/[\text{G}], \tag{5.32}$$

where D_0 is the diffusion constant at one amagat.

We first measured Rb spin decay rates at an oven temperature of 150°C, corresponding to a Rb density of $\sim 7 \times 10^{13}$ cm^{-3} (measured as described in section 2.6).

At this temperature, the spin exchange rate between alkali atoms is approximately 6×10^4/s [Walker97], significantly greater than even the highest loss rate we have measured. It is therefore a good approximation to describe the Rb polarization by a single spin-temperature distribution, and fit relaxation transients to a single exponential.

Our experiment follows closely the design of other recent spin-relaxation experiments in our laboratory [Kadlecek98] [Erickson00]. The spin-exchange cell, oven, and polarization analyzer have been described in Chapter 2. The Rb atoms are spin-polarized using circularly polarized light from a broad-band diode array, intentionally tuned 1.2 nm off the atomic $5S_{1/2} \rightarrow 5P_{1/2}$ (795 nm) resonance to produce a spatially homogeneous, low (<5%) Rb spin polarization. The Rb spin-polarization is deduced by Faraday rotation of 0.5 mW of diode laser light tuned 2 nm off the $5S_{1/2} \rightarrow 5P_{3/2}$ (780 nm) resonance. The large probe detuning was selected to produce a light-induced relaxation rate of < 1/s at the highest gas pressures. A mechanical chopper periodically blocked the pump light and relaxation transients "in the dark" were digitized and averaged by a digital oscilloscope. The relaxation transients were fit to single exponentials $\exp[-\Gamma t]$ (as expected, given our low spin polarization, no evidence was found for multiple relaxation times) with a typical statistical uncertainty in the fitted decay rates of 1/s.

We periodically verified that the light-induced relaxation rate was indeed negligible by adding an additional 1/10 neutral density filter to the probe beam and remeasuring Γ. Though statistical error was increased (due to smaller, noisier signals), no significant change in Γ was detected.

We also checked that each averaged transient did consist of only a single exponential. First, we visually checked the residuals of each exponential fit for any signs of another exponential. Second, we designed a short computer program to fit each transient from a number of different starting points, starting progressively farther down the decay

curve with each point. We recorded both the value of Γ and the statistical uncertainty in Γ at each point. As expected, the uncertainty in Γ increases as less of the transient is fit, but the value of Γ is (within error) unchanged.

The decay rates are shown as a function of gas density in Fig. 5.1. We find that the transient decay rates are highly reproducible, with the caveat that we found when fresh gas was put into the cell the relaxation rates sometimes temporarily decreased by 5-10/s due to reduced Rb vapor pressure. The decrease in Γ is well explained by reduced vapor pressure affecting Γ_{corr}, and is likely due not to Rb-Rb relaxation [Kadlecek98] [Erickson00]. We made certain that the cell had returned to equilibrium each time by measuring Γ every ten minutes after adding gas, stopping when 4 sequential measurements agreed to within 1%.

We fit equation 5.27 to the data of figure 5.1, using the 4 free parameters γ_{inv}, $\langle\sigma v\rangle$, Γ_{vdW}, and a characteristic density parameter $[\mathrm{G}]_1$, where we have defined a single $[\mathrm{G}]_1 \equiv [\mathrm{G}]_{1,85}$. Because the inverse pressure relaxation rate obscures the "long" to "short" lifetime transition in the data of 5.1, we have forced the relation

$$[\mathrm{G}]_1/[\mathrm{G}]_0 = \omega_{hf,85}/\left(\gamma N/\hbar\right) \tag{5.33}$$

by setting $[\mathrm{G}]_0 = [\mathrm{G}]_1/22.5$ from the ^{85}Rb hyperfine splitting and the previously measured $\gamma N/h = 135$ MHz [Wu85]. If we fit without this constraint (with $[\mathrm{G}]_0$ as a fifth free parameter), the values obtained for $[\mathrm{G}]_0$ and γ_{inv} have statistical errors associated with them many times their own magnitude; we don't have the low density data needed to sort out the contribution from these two competing effects. However, the other three fit parameters are left essentially unchanged.

The fit to the data is excellent, and gives

$$\gamma_{inv} = 2.66 \pm 0.64\ (-0.1/+0.37)\ \mathrm{s}^{-1}\mathrm{amagat} \tag{5.34}$$

$$\langle\sigma v\rangle = (2.44 \pm 0.02\ (-0.07/+0.16)) \times 10^5\ \mathrm{s}^{-1}\mathrm{amagat}^{-1} \tag{5.35}$$

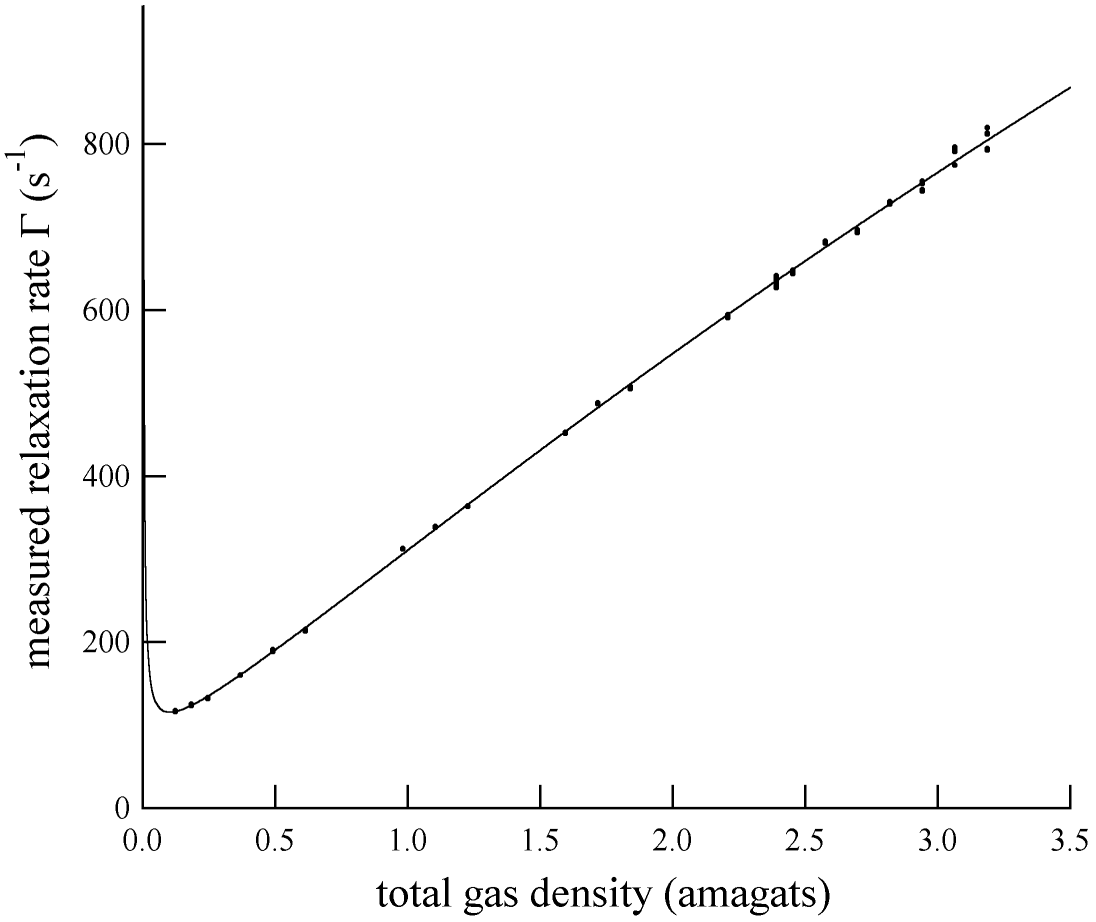

Figure 5.1: Measured transient decay rates as a function of total gas density at 150°C, for a mixture of 98% He, 1% N_2, and 1% Xe. The results of approximately four measurements are shown at each gas density.

$$\Gamma_{vdW} = 2049 \pm 110\ (+40/-120)\ \mathrm{s}^{-1} \quad (5.36)$$

$$[\mathrm{G}]_1 = 1.95 \pm 0.20\ (-0.21/+0.66)\ \text{amagat} \quad (5.37)$$

The last two numbers are specific to a He(98%)-N_2(1%)-Xe(1%) mixture. The first error quoted is statistical, while the second (in parentheses) is systematic. The largest source of systematic error is fluctuating Rb number density affecting our spin-exchange corrections. We have set systematic error bars, therefore, by assuming ±30% error in Γ_{SE} and simply refitting the data at each extreme. The systematic error shown then gives the deviation at 30% greater [Rb] and 30% smaller [Rb], respectively.

To emphasize the contribution of van der Waals molecules to Rb spin loss, we have applied the first order ($\Gamma_{vdW}/\Gamma_{SE}, \langle\sigma v\rangle[\mathrm{Xe}]/\Gamma_{\mathrm{SE}}$) corrections to the data points themselves (increasing the highest pressure measured values by ≈5%). We then subtracted the binary spin loss contribution, $[\mathrm{Xe}]\langle\sigma v\rangle$, and the diffusion/singlet molecule loss contribution, $\gamma_{inv}/[\mathrm{G}]$, from the data. This corrected data appears in figure 5.2 along with the fit from figure 5.1, altered in the same manner.

We note here that this value of γ_{inv}, if assumed to be entirely due to diffusion (no Rb-Rb singlet molecule relaxation), yields a diffusion constant $D(\mathrm{Rb} -^4 \mathrm{He})|_{1\ \text{amagat},150^\circ\mathrm{C}} = 1.65 \pm 0.5\ \mathrm{cm}^2/\mathrm{s}$. This is consistent with the D_0 obtained in the work of reference [Wagshul94], where the authors made this assumption and measured $D_0(\mathrm{Rb} -^3 \mathrm{He}) = 1.5 \pm 0.4\ \mathrm{cm}^2/\mathrm{s}$ at 150°C by similar methods (we can expect

$$D_0(\mathrm{Rb} -^3 \mathrm{He})/D_0(\mathrm{Rb} -^4 \mathrm{He}) = 1.25 \pm 0.1$$

from reference [Aymar69]). However, Aymar *et. al.* measured $D_0(\mathrm{Rb} -^4 \mathrm{He}) = 0.42 \pm 0.06\ \mathrm{cm}^2/\mathrm{s}$ at 27°C [Aymar69], where Rb number density is so low that Rb singlet molecule relaxation is entirely negligible. Scaling their result by $T^{1/2}$ yields $D_0 = 0.50\ \mathrm{cm}^2/\mathrm{s}$ at 150°C, a factor of three smaller than our result under the above assumption.

However, if we assume $D_0 = 0.50\ \mathrm{cm}^2/\mathrm{s}$, equation 5.32 yields a wall relaxation

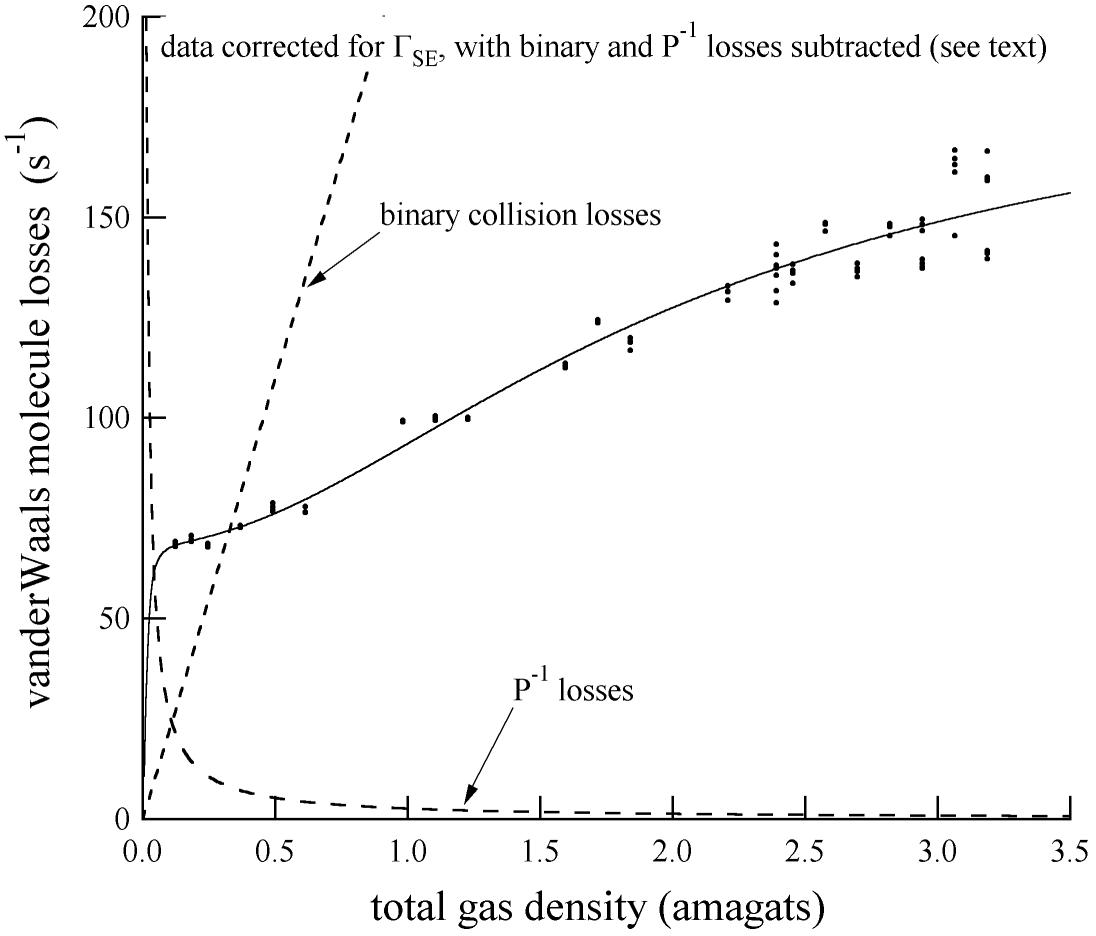

Figure 5.2: Data of figure 5.1, corrected for Γ_{SE}, and with $\langle\sigma v\rangle$[Xe] and $\gamma_{inv}P$ subtracted off.

rate $\Gamma_{dif} = 0.81$ s^{-1}·amagats. The remaining γ_{inv} relaxation, 1.85 s^{-1}·amagats, can be compared with the Rb-Rb singlet molecule relaxation in N_2 buffer gas as measured by Kadlecek *et. al.* in ref. [Kadlecek98]. From that reference, we can expect 1.2 out of every 1000 Rb atoms to be contained in a singlet dimer at any time (the binding energy of these Rb singlet dimers, 500 meV, is much greater than kT [Krauss90]). At this dimer fractional density, 1.85 s^{-1}·amagats implies a dimer spin-reorientation cross section for ^{4}He collisions equal to $3.6\mathring{A}^2$, or approximately half that measured for N_2 (a reasonable value).

5.1.2 Low Temperature

In natural isotopic mixtures of Rb vapor at low densities ([Rb]), interpretation of spin-relaxation transients is considerably complicated by the two isotopes having different nuclear spin. At high densities, spin-exchange collisions occur at a higher rate than spin is lost, and simplify the interpretation of the experiments as described above. At lower densities, when the spin-exchange rate is comparable to the relaxation rates, however, it is necessary to make a precise measurement of the Rb density and to account for multiple time constants in the decay transients. To avoid having to measure the Rb density, we have chosen to repeat the measurements of the previous section at a low enough temperature (80 °C) that the spin-exchange rates are much less than the spin-relaxation rates.

When spin-exchange collisions can be ignored, the ^{85}Rb and ^{87}Rb populations relax independently, with two relaxation rates per isotope. However, one rate for each isotope, the "fundamental" rate, is much faster than the other [Appelt98]. Application of equation (186) of that reference with the spin exchange rate $1/T_{ex} = 0$ reduces to the following result for the fundamental relaxation rate of an alkali vapor in the low spin

exchange limit:

$$\Gamma_{i\,fun} = \frac{1}{(2I_i+1)^2 T_{FD}} + \frac{2}{(2I_i+1)^2 T_{SD}}, \tag{5.38}$$

where, in the notation of that reference, $1/T_{FD}$ is the F-damping rate and $1/T_{SD}$ is the S-damping rate. For the two Rb isotopes, equation 5.38 yields

$$\Gamma_{85\,fun} = \frac{1}{18}\left(\langle\sigma v\rangle[\mathrm{Xe}] + \frac{f_{1,85}+f_{0,85}}{2}\Gamma_{vdW}\right) \tag{5.39}$$

$$\Gamma_{87\,fun} = \frac{1}{8}\left(\langle\sigma v\rangle[\mathrm{Xe}] + \frac{f_{1,87}+f_{0,87}}{2}\Gamma_{vdW}\right). \tag{5.40}$$

The ratio of these two rates would be simply 2.25 were it not for the f factors, but the f's are of course to be determined from the data.

We have therefore chosen to analyze our data in the following way. We first fit the transients to a sum of exponentials $\exp -\Gamma_{85}t + r\exp -2.25\Gamma_{85}t$, with the fit value of r checked to be sure it is approximately the ratio of the isotopic fractions, η_{87}/η_{85}. We take a series of such relaxation transients to determine Γ_{85} at various pressures, and fit the pressure dependence to equation 5.41 with $\langle\sigma v\rangle$, $[\mathrm{G}]_1$, $[\mathrm{G}]_0$, and Γ_{vdW} as free parameters. We then use the fit values so determined to calculate the ratio $g = \Gamma_{87}/\Gamma_{85}$ as function of pressure and refit our transients to $\exp -\Gamma_{85}t + r\exp -g\Gamma_{85}t$. On the first iteration of this procedure, the relaxation rates changed by less than 5% at all pressures, and after the second iteration the rates changed by only 1%. Our measured Rb density was 5×10^{10} cm^{-3}, implying spin-exchange corrections of less than 1%.

We fit the resulting data to the following equation:

$$\Gamma_{85} = \frac{1}{18}\left(\langle\sigma v\rangle[\mathrm{Xe}] + \frac{f_{1,85}+f_{0,85}}{2}\Gamma_{vdW}\right) + \gamma_{inv}/[\mathrm{G}], \tag{5.41}$$

where we have included γ_{inv} as neither F-damping nor S-damping, but instead as a mechanism which simply removes all angular momentum from atoms striking the walls of the cell (at this low Rb number density, Rb singlet dimers should contribute less than

a tenth as much relaxation as at 150°C (barely 1 out of 10000 Rb atoms is contained in a dimer)[Kadlecek98]).

The spin-relaxation rate Γ_{85} is shown in Fig. 5.3 as a function of density. The

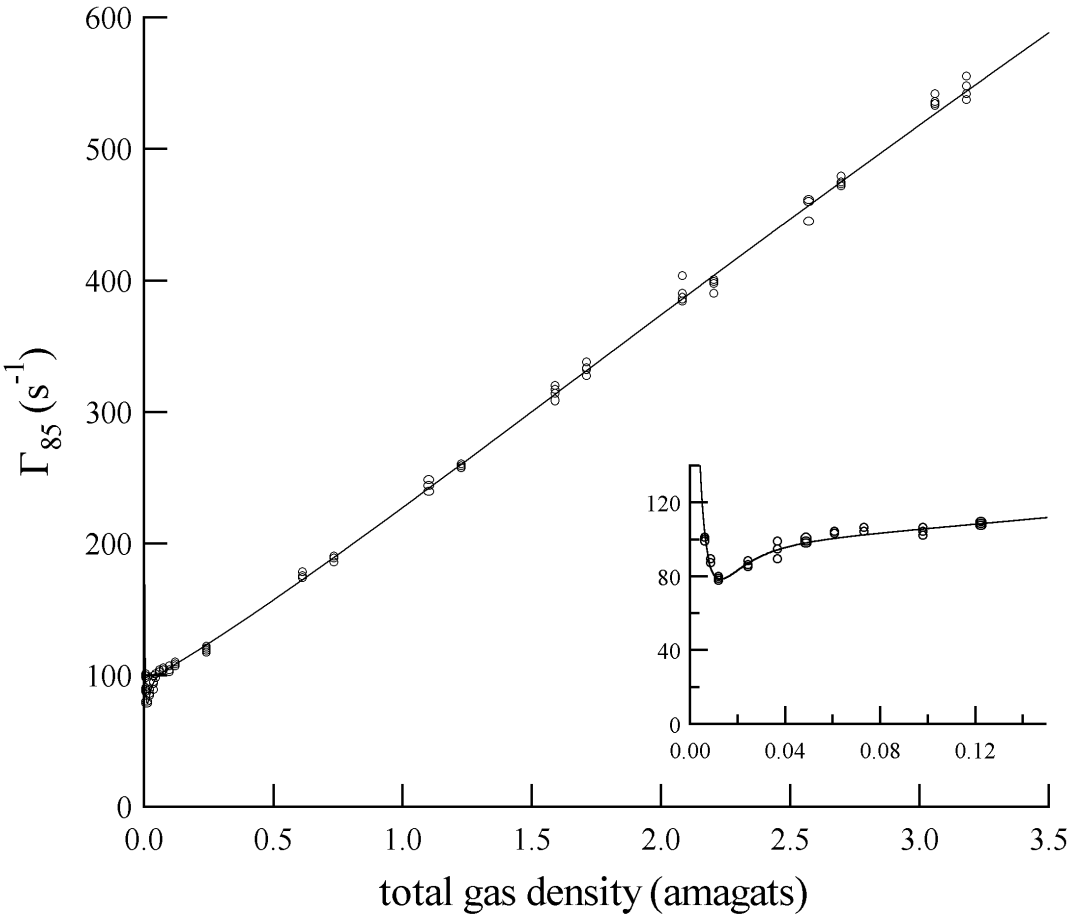

Figure 5.3: Spin-relaxation rate Γ_{85} as a function of total gas density, with fit. The inset shows the low pressure portion of the data.

data qualitatively resemble the high temperature data, but at the lower temperature the singlet molecule contribution to the relaxation is smaller and we are able to see the decrease in the van der Waals molecule contribution to the relaxation rate at low densities.

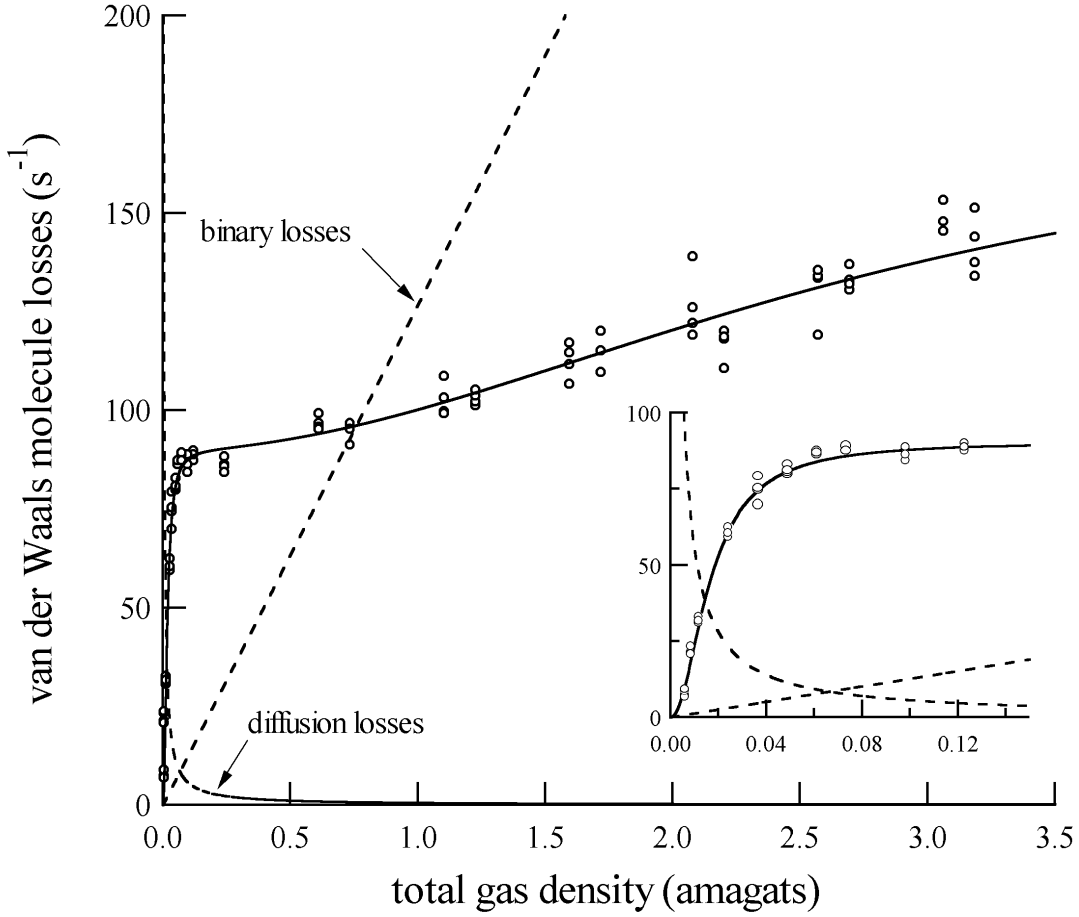

Figure 5.4: Data of figure 5.3, with binary and diffusion losses (obtained from the fit) subtracted off.

We find at a temperature of 80°C

$$\gamma_{inv} = 0.56 \pm 0.01 \text{ s}^{-1}\text{amagat} \quad (5.42)$$

$$\langle \sigma v \rangle = 2.28 \pm 0.07 \times 10^5 \text{ s}^{-1}\text{amagat}^{-1} \quad (5.43)$$

$$\Gamma_{vdW} = 3240 \pm 100 \text{ s}^{-1} \quad (5.44)$$

$$[\text{G}]_1 = 2.80 \pm 0.60 \text{ amagat} \quad (5.45)$$

$$[\text{G}]_0 = 0.100 \pm 0.010 \text{ amagat}, \quad (5.46)$$

where the quoted errors are statistical.

As stated earlier, we were unable to extract a measurement of D_0 from our high temperature data (most likely due to relaxation in Rb singlet molecules). The value of γ_{inv} we obtained at 80°C, when inserted into equation 5.32, yields $D_0 = 0.35 \pm 0.03\text{cm}^2/\text{s}$. This is in reasonable agreement with the measurement of Aymar *et al.* [Aymar69], whose result at 27°C yields $D_0 = 0.46 \pm .07$ when scaled by $T^{1/2}$ to 80°.

5.1.3 Analysis

Our two binary spin loss rate coefficient measurements are consistent with the expected $T^{1/2}$ temperature dependence (see figure 5.5), yielding

$$\langle \sigma v \rangle \Big|_{300^\circ K} = (2.08 \pm 0.17) \times 10^5 \text{ s}^{-1}\text{amagat}^{-1} \quad (5.47)$$

$$= (7.72 \pm 0.64) \times 10^{-15} \text{ cm}^3\text{s}^{-1}. \quad (5.48)$$

Bouchiat previously measured $\sigma = (16.41 \pm 0.87) \times 10^{-4} \mathring{A}^2$, or $\langle \sigma v \rangle = (5.73 \pm 0.30) \times 10^{-15}$ cm^3/s, at low pressure (<1 Torr) at 27°C [Bouchiat72], significantly lower than our result. It is pointed out in reference [Bouchiat72] that because γ is actually a function of interatomic distance, there is reason to suspect that σ/γ^2 is a constant. Our results, combined with that of Bouchiat *et al.* suggest an approximately linear tem-

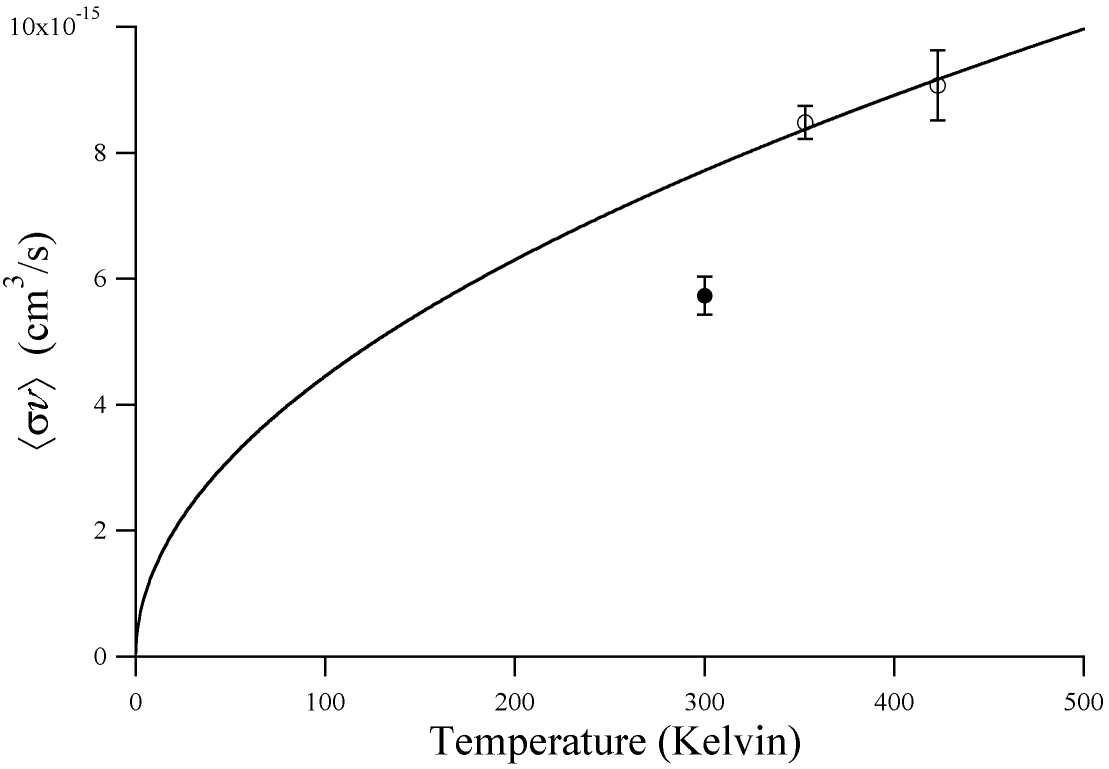

Figure 5.5: Measured binary collision spin loss rate coefficients. The open circles are from this work, while the filled circle is from reference [Bouchiat72]. The solid line shows a $T^{1/2}$ temperature dependence.

perature dependence to $\langle \sigma v \rangle$, which in turn suggests a weak temperature dependence ($T^{1/4}$) to $\langle \gamma(r) \rangle$.

The ratio of the characteristic pressures at 80°C is $[\mathrm{G}]_1/[\mathrm{G}]_0 = 28 \pm 5$, in reasonable accord with the expected 22.5 from the Rb hyperfine splitting and the previously measured $\gamma N/h = 135$ MHz [Wu85]. The ratio of Γ_{vdW} to $[\mathrm{G}]_1$ yields

$$\frac{(\Gamma_{vdW}/[\mathrm{G}]_1)_{150^\circ\mathrm{C}}}{(\Gamma_{vdW}/[\mathrm{G}]_1)_{80^\circ\mathrm{C}}} = 0.91 \pm 0.25$$

Within errors, this is consistent with the $T^{-3/2}$ scaling that would predict 0.76 for this ratio. The $T^{-3/2}$ dependence assumes (see equation 5.15) $\frac{\gamma N}{\hbar}$ and $[\mathrm{G}]_0/[\mathrm{G}]_1$ are temperature independent and the temperature dependence of $\mathcal{K}$ is dominated by the

$T^{-3/2}$ phase-space factor.

The strong temperature variation of $[\mathrm{G}]_1$ (and, presumably, $[\mathrm{G}]_0$ as well) is somewhat surprising, as it suggests that the breakup cross section for RbXe molecules is strongly temperature dependent. Indeed, our two data points suggest a $T^{-2.0}$ temperature dependence for $[\mathrm{G}]_1$.

Our two measurements of Γ_{vdW} suggest a temperature dependence of $T^{-2.5}$. From equation 5.15 and our assumed $T^{-3/2}$ temperature dependence of $\mathcal{K}$, this in turn suggests a T^{-1} temperature dependence to $[\mathrm{G}]_0\gamma N/\hbar = (\gamma N/\hbar)^2\tau$. We must assume that the temperature dependence of $[\mathrm{G}]_1$ ($\sim T^{-2}$) is due to τ, which leads us to a $T^{1/2}$ dependence of $\frac{\gamma N}{\hbar}$. The only other direct measurement of Γ_{vdW} is that of reference [Cates92]; the gas composition in that work was almost entirely xenon (a small amount of N_2 buffer gas was also present). Though it is possible in theory to connect the two results, doing so requires knowledge of $[\mathrm{G}]_0$ in pure xenon, $[\mathrm{G}]_0$ in pure helium, and $[\mathrm{G}]_0$ in pure nitrogen [Schaefer90].

A direct comparison of our high temperature results can be made with recent work on polarization imaging of dense (> 7 amagat) optically pumped cells with similar gas compositions to ours [Baranga98b] [Shah00]. For these experiments the width of magnetic resonance lines depends on the spin-relaxation rate. The quoted relaxation rates are total spin relaxation rates γ where $d\langle F_z\rangle/dt = -\gamma\langle S_z\rangle$. At these high pressures, $f_{1,85} = 0.94$ so we can assume the high pressure limit (all f's $= 1$) and find $\gamma \approx \langle\sigma v\rangle[\mathrm{Xe}] + \Gamma_{vdW}$. For the 7.8 atm, 1.34% Xe cell of Ref. [Baranga98b] we predict 2.6×10^4 s^{-1}, somewhat smaller than the observed 3×10^4 s^{-1}. For the 7.0 atm, 1% Xe cell of ref. [Shah00], our results predict 1.97×10^4 s^{-1} which is in close agreement with the observed 1.84×10^4 s^{-1}.

5.2 Rb-^{129}Xe Spin Exchange Rate

The dominant terms in the Hamiltonian for our Rb-Xe system in a magnetic field **B** is

$$H = A\mathbf{I}\cdot\mathbf{S} + \gamma\mathbf{N}\cdot\mathbf{S} + \alpha\mathbf{K}\cdot\mathbf{S} + \cdots,$$

where $A\mathbf{I}\cdot\mathbf{S}$ is the Rb hyperfine interaction between the Rb electron spin **S** and its nuclear spin $A\mathbf{I}$, $\alpha\mathbf{K}\cdot\mathbf{S}$ is the Fermi contact interaction between **S** and the Xe nuclear spin **K**, and $\gamma\mathbf{N}\cdot\mathbf{S}$ is the spin-rotation interaction between **S** and the angular momentum **N** of a Rb-Xe colliding pair. It is the Fermi contact term, $\alpha\mathbf{K}\cdot\mathbf{S}$, which is responsible for Rb-Xe spin exchange. This spin exchange can in principle occur in either binary collisions or in Rb-^{129}Xe van der Waals molecules.

As has been discussed in section 5.1, there are three important regimes for the van der Waals molecules' lifetimes in our system: the long lifetime limit set by the spin rotation interaction, the "very short" lifetime limit set by the Rb hyperfine interaction, and the intermediate short lifetime regime. While previous work has explored the short lifetime limit [Cates92], the trend toward higher pressures in spin-exchange systems has made measurements in the transition region between the short and "very short" lifetime limits particularly desirable. This consideration has driven us to measure Rb-^{129}Xe spin-exchange rates between 0.6 and 3.1 amagats. This pressure range allows us to observe the transition from the short to the "very short" regime, while always staying well above the short to long lifetime transition at gas density $[\mathrm{G}]_0$ (measured in section 5.1.2 above).

The rate of change of $\langle K_z\rangle$ due to spin exchange with a Rb vapor is given by [Happer84] [Appelt98]

$$\begin{aligned}\frac{d}{dt}\langle K_z\rangle &= \sum_i \frac{(f_{0,i}-f_{1,i})\phi_\alpha^2}{2(2I_i+1)^2 T_{Xe}}\left(\langle F_{iz}\rangle - \langle 2F_i^2 - 2F_{iz}^2\rangle\langle K_z\rangle\right) + \\ &\quad \frac{f_{1,i}\phi_\alpha^2}{2T_{Xe}}(\langle S_{iz}\rangle - \langle K_z\rangle) + [Rb]\langle\sigma_{SE}v\rangle(\langle S_{iz}\rangle - \langle K_z\rangle) - \Gamma'\langle K_z\rangle. \quad (5.49)\end{aligned}$$

The first term is responsible for relaxation in short lived molecules (F-damping), where $(1 - f_{1,i})$ is the fraction of van der Waals molecules which break up in a time long compared to the characteristic hyperfine interaction time of Rb isotope i. The second term describes very short lived molecules (S-damping), where $f_{1,i}$ is the fraction of van der Waals molecules which break up in a time short compared to the characteristic hyperfine interaction time of Rb isotope i. (For the work described in this section, the gas density is always well above the short to long lifetime transition, so we will set $(1-f_{0,i})$, the fraction of molecules which live longer than the characteristic spin rotation interaction time, equal to 1.) Γ' represents all other ^{129}Xe relaxation mechanisms that may be present, and $\langle \sigma_{SE} v \rangle$ is a velocity averaged binary spin exchange rate coefficient.

We can make several simplifications to this equation. First, we watch K_z decay in the absence of optical pumping. Therefore we are assured that $F_{iz}, S_{iz} \ll 1$. We are then able to make the substitution [Happer84]

$$\langle F_i^2 - F_{iz}^2 \rangle = \frac{1}{2} + \frac{2}{3} I_i (I_i + 1). \tag{5.50}$$

Assuming further that $\langle S_{iz} \rangle \ll \langle K_z \rangle$ (guaranteed just after optical pumping is turned off) allows us to write

$$\frac{d}{dt} \langle K_z \rangle = -\Gamma \langle K_z \rangle, \tag{5.51}$$

where

$$\Gamma = \sum_{85,87} \frac{\phi_\alpha^2 \eta_i}{2 T_{Xe}} \left(\frac{1 + \frac{4}{3} I_i (I_i + 1)}{(2 I_i + 1)^2} (1 - f_{1,i}) + f_{1,i} \right) + [\mathrm{Rb}] \langle \sigma_{SE} v \rangle + \Gamma'. \tag{5.52}$$

We perform the sum in equation 5.52 over the two stable Rb isotopes, ^{85}Rb and ^{87}Rb:

$$\Gamma = \frac{\phi_\alpha^2}{2 T_{Xe}} \left(0.358 + \frac{0.648 \eta_{85}}{1 + (\frac{[\mathrm{G}]_1}{[\mathrm{G}]})^2} + \frac{0.625 \eta_{87}}{1 + (\frac{2.25 [\mathrm{G}]_1}{[\mathrm{G}]})^2} \right) + [\mathrm{Rb}] \langle \sigma_{SE} v \rangle + \Gamma'. \tag{5.53}$$

We point out that the factor of 2.25 which appears in the denominator of equation 5.55 is simply the ratio of the ^{87}Rb hyperfine frequency to that of ^{85}Rb, and appears

because we have again chosen to redefine a single $[\mathrm{G}]_1$ as equal to the characteristic density for ^{85}Rb. We also note that equation 5.53 agrees with references [Happer84] and [Cates92] in the proper limits.

We rewrite the multiplier of the first term in terms of the chemical equilibrium coefficient, $\mathcal{K}$, (recall $\mathcal{K} = [\mathrm{RbXe}]/([\mathrm{Rb}][\mathrm{Xe}])$, and the characteristic density $[\mathrm{G}]_1$:

$$\frac{\phi_\alpha^2}{2T_{Xe}} = \frac{\mathcal{K}\alpha[\mathrm{Rb}]}{2\hbar}\frac{[\mathrm{G}]_1}{[\mathrm{G}]}. \tag{5.54}$$

Finally, we assume that the spin exchange rate is much higher than any other rate Γ', and so we fit our data to

$$\Gamma_{SE}/[\mathrm{Rb}] = \frac{\mathcal{K}\alpha}{2\hbar x}\frac{[\mathrm{G}]_0}{[\mathrm{G}]_1}\frac{[\mathrm{G}]_1}{[\mathrm{G}]}\left(0.358 + \frac{0.648\eta_{85}}{1+(\frac{[\mathrm{G}]_1}{[\mathrm{G}]})^2} + \frac{0.625\eta_{87}}{1+(\frac{2.25[\mathrm{G}]_1}{[\mathrm{G}]})^2}\right) + \langle\sigma_{SE}v\rangle. \tag{5.55}$$

We verified that $\Gamma' \ll \Gamma_{SE}$ by measuring the relaxation rate of the ^{129}Xe in our cell after it had cooled to approximately 40°C. We obtained $\Gamma' \approx .0012$ s^{-1}, a factor of 6 less than the slowest decay rate measured at 120°C, and a factor of 25 less than the slowest decay rate measured at 150°C.

We have written the multiplier of the first term of equation 5.55 in this way because we assume that the ratio $[\mathrm{G}]_0/[\mathrm{G}]_1 = \omega_{hf,85}/\omega_{\gamma N}$ is largely temperature independent. We will then assume that the temperature dependence of equation 5.55 is entirely contained within three parameters: $\mathcal{K}$, which we assume has a $T^{-3/2}$ dependence; $\langle\sigma v\rangle$, for which we assume $T^{1/2}$; and $[\mathrm{G}]_1$ (recall that the data of section 5.2 suggested $[\mathrm{G}]_1 \propto T^{-2.0}$).

5.2.1 Γ_{SE} Measurements

As others have previously done [Cates92], we have measured Γ_{SE} by observing the decay of the ^{129}Xe nuclear polarization in our cell just after optical pumping light has been turned off. However, we have chosen to observe the ^{129}Xe nuclear polarization decay by

observing the Rb repolarization induced by the ^{129}Xe via the spin-exchange interaction $\alpha\mathbf{K}\cdot\mathbf{S}$ in the absence of pumping light [Zeng85]. In spin-temperature equilibrium, the small Rb repolarization follows the ^{129}Xe with a proportionality given by

$$\langle S_z\rangle = \langle K_z\rangle \frac{\Gamma_{SE}}{\Gamma_{SE}+\Gamma_{SD}}, \tag{5.56}$$

where here Γ_{SE} is the rate at which Rb acquires spin from ^{129}Xe, and the sum $\Gamma_{SE}+\Gamma_{SD}$ (Γ_{SD} is the spin destruction rate, and describes angular momentum lost from the $\langle S_z\rangle$, $\langle K_z\rangle$ system) is exactly the total Rb spin loss rate measured in section 5.1. When not in spin-temperature equilibrium, the Rb polarization continues to follow the ^{129}Xe polarization, although the constant of proportionality is more complicated [Zeng85].

This method offers two significant advantages over observing the ^{129}Xe polarization $\langle K_z\rangle$ directly via NMR. Firstly, unlike NMR techniques, optical observation of Rb polarization $\langle S_z\rangle$ is a completely lossless method of tracking $\langle K_z\rangle$. Secondly, a minimal change in our polarization analyzer (as described in chapter 2) allows us to *measure* [Rb], as opposed to being forced to infer [Rb] from oven temperature and published vapor pressure data. This has been the dominant source of error in previous similar Γ_{SE} measurements [Cates92]. We note that recent evidence and our own observations as well suggest that high power laser absorption leads to significant internal heating of spin-exchange cells [Walter01], casting further suspicion on the method of inferring [Rb] from measured oven temperatures; though the actual relaxation transients in [Cates92] were recorded in the dark, we note that our experience suggests that it takes several minutes for [Rb] to equilibrate after a strong pump beam is switched off.

The spin-exchange cell, oven, and polarization diagnostics have been described previously (see Chapter 2). For the Faraday rotation measurements of the previous section, we were able to use a significant fraction of a milliwatt of probe power without fear of perturbing the Rb polarization — we simply detuned the probe from resonance until

the Rb loss rate did not depend upon the probe power (until probe absorption was negligible). However, for the circular dichroism measurements of this section, some significant fraction of the probe must be absorbed. The Rb spin loss rate is determined by the number of photons absorbed:

$$\Gamma_{probe} = \frac{1}{2}\frac{N_\gamma}{[\mathrm{Rb}]\pi r^2 l}, \tag{5.57}$$

where N_γ is the number of photons absorbed and $\pi r^2 l$ is the volume of the cell filled by the probe beam. We therefore reduced our probe beam intensity to 25 μW through the use of a $\lambda/2$ plate and a polarizing beam splitter cube. If we assume complete absorption of our 25 μW, 2mm diameter probe beam over the 8 cm length of the cell, the Rb loss rate due to absorption is at most 5 per second (for [Rb] = 10^{13} cm^{-3}), much less than the minimum loss rate due to collisions in the cell (see section 5.1).

We used a single 15 Watt fiber coupled diode array as the pumping light source for these measurements. The unpolarized output of the fiber bundle is approximately 1000 GHz (2 nm) wide, centered around 795 nm. We first imaged the end of the fiber bundle onto a chopper wheel with unit magnification. We then collimated the beam to approximately 2 cm diameter with a 5 cm focal length lens, and passed it through a polarizing beam splitter cube. In order to minimize heating associated with pump light absorption, we wished to avoid excessive amounts of pumping light. For this reason, we simply blocked one of the beams from the cube. We passed the other beam through a $\lambda/4$ plate and imaged the collimating lens onto the cell with magnification $\sim$4 (grossly overfilling the cell). In this way, we delivered only $\sim$3 Watts of spatially uniform light to the cell.

For each temperature and pressure, we first allowed the cell to equilibrate with the pump beam on for approximately ten minutes. We then measured $[\mathrm{Rb}]\sigma_\circ l$ by comparing the total voltage V_{DC} on the analyzer photodiodes (with pump beam and

PEM off) to a baseline voltage V_0, recorded with the cell at or near room temperature (such that the Rb vapor pressure is negligible).

$$[\mathrm{Rb}]\sigma_\circ l = -\ln \frac{V_{DC}}{V_0} \tag{5.58}$$

We retuned the probe beam occasionally so as to maintain 30%-70% absorption ($[\mathrm{Rb}]\sigma_\circ l$ changed with cell pressure as well as temperature). We rechecked V_0 frequently (approximately daily), so as to verify that our $[\mathrm{Rb}]\sigma_\circ l$ measurements were not affected by any systematic drift (*e.g.* in probe laser output power or frequency).

We then chopped the pump beam at approximately 10 Hz and used the analyzer in the upper configuration of figure 2.6. The lock-in amplifier then puts out an approximately square wave at the chopper frequency, which we display on an oscilloscope. The amplitude of this square wave, V_{cd}, is given by equation 2.17. Background circular dichroism (of cell windows and/or optics) is automatically corrected for by means of this chopper technique. We can then calculate the quantity $[\mathrm{Rb}]\sigma_\circ lP$:

$$[\mathrm{Rb}]\sigma_\circ lP = 2\sinh^{-1}\left(\frac{V_{cd}}{\sqrt{2}V_{DC}J_1(\beta)}\right) \tag{5.59}$$

The ratio of equation 5.59 to equation 5.58 gives us the polarization P of the Rb.

After changing the optics to the lower configuration of figure 2.6 and measuring the new amplitude of the square wave from the lock-in amplifier, V_{FR}, we calculate $[\mathrm{Rb}]P$ from equations 2.8 and 2.22:

$$[\mathrm{Rb}]P = \frac{1}{2}\left(\frac{\pi l e^2 c}{3mc^2}\left(\frac{1}{\Delta_{3/2}}\right)\right)^{-1} \sin^{-1}\left(\frac{V_{fr}}{\sqrt{2}V_{DC}J_1(\beta)}\right), \tag{5.60}$$

where it is assumed that $\Delta_{1/2} \gg \Delta_{3/2} \gg \gamma_{3/2}$. Having previously calculated P, this gives us a *measurement* of the Rb number density [Rb].

Leaving the analyzer in the lower configuration, we then turned off the chopper wheel and pumped the cell for approximately two spin-exchange times (2-5 minutes

depending on Rb number density) before turning off the pump beam. The oscilloscope records the subsequent decay $V_{FR}(t)$. A sample of this data appears in figure 5.6. We fit each decay curve to a single exponential $\exp(-\Gamma t)$, and divided the rate from the fit by our measured Rb density to obtain the spin exchange rate coefficient at each temperature and pressure.

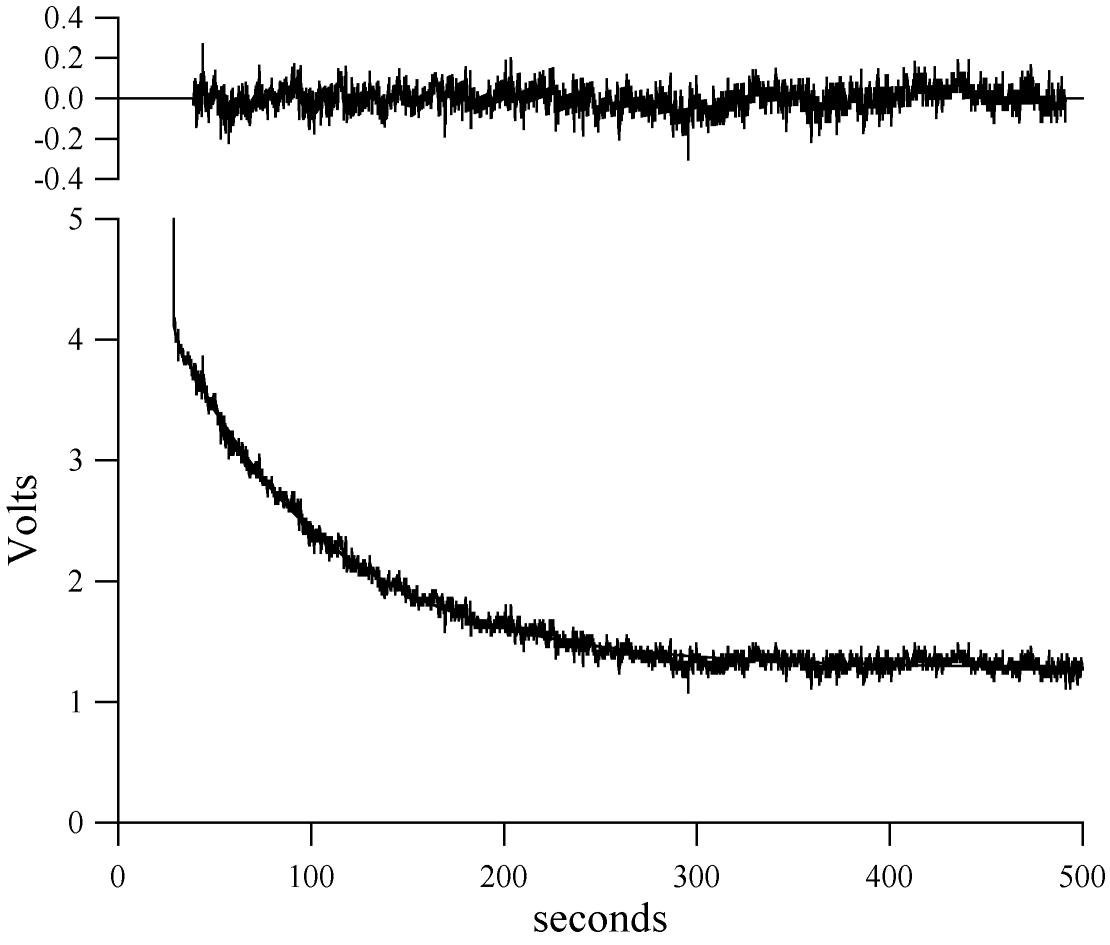

Figure 5.6: A sample of our spin exchange data (130°C, 1.84 amagats). The Rb repolarization signal is shown along with the exponential fit and the residuals from that fit. The spin exchange rate given by the fit is 0.01237 s^{-1}.

We initially made use of an 780 nm band pass interference filter to isolate the

analyzer optics from the pump beam. However, we found that the filter was heated by the pump beam during the pumping up cycle, changing its transmission of the 780 nm probe beam. During the decay cycle the filter would again cool, causing a characteristic drift in $V_{FR}(t)$. We found it necessary to remove the filter and instead isolate the analyzer from the pump beam by making use of the small angle at which the probe passes through the cell; a pair of ≈5 mm apertures placed after the cell approximately 1 meter apart both passed the probe beam while blocking all direct pump light.

In an attempt to cancel any unnoticed systematic drifts, we took each decay curve four times, twice with the ^{129}Xe atoms aligned along the field and twice with the ^{129}Xe atoms aligned against the field. Changing the polarization changes the polarity of the decay curve; any systematic drift not associated with the ^{129}Xe polarization would be averaged out. We noticed no such systematic difference between the two pairs of decay curves at each temperature and pressure, and the standard deviations of the averages at each point were typically 5-10%.

Our measured spin-exchange rate coefficients are shown as a function of 1/[G] in figure 5.7.

5.2.2 Analysis

We fit the entire data set shown in figure 5.7 to equation 5.55 by assuming that we the temperature dependence of $\mathcal{K}$ is $T^{-3/2}$ and that of $\langle\sigma v\rangle$ is $T^{1/2}$. We then used six free parameters:

$$\gamma_{SE}\Big|_{20^\circ\mathrm{C}}, \langle\sigma_{SE}v\rangle\Big|_{20^\circ\mathrm{C}}, [\mathrm{G}]_1\Big|_{120^\circ\mathrm{C}}, [\mathrm{G}]_1\Big|_{130^\circ\mathrm{C}}, [\mathrm{G}]_1\Big|_{140^\circ\mathrm{C}}, \text{ and } [\mathrm{G}]_1\Big|_{150^\circ\mathrm{C}}, \tag{5.61}$$

where we have defined $\gamma_{SE} = \mathcal{K}\alpha/\left(2\hbar x\right)\frac{[\mathrm{G}]_0}{[\mathrm{G}]_1}$. Note that then the slope of each line approaches $\gamma_{SE}[\mathrm{G}]_1$ in the low density limit (*i.e.* the right hand side of the graph),

and the y-intercept is $\langle \sigma_{SE} v \rangle$ at 20°C. The fit to the data is shown in figure 5.7, and provides the following values:

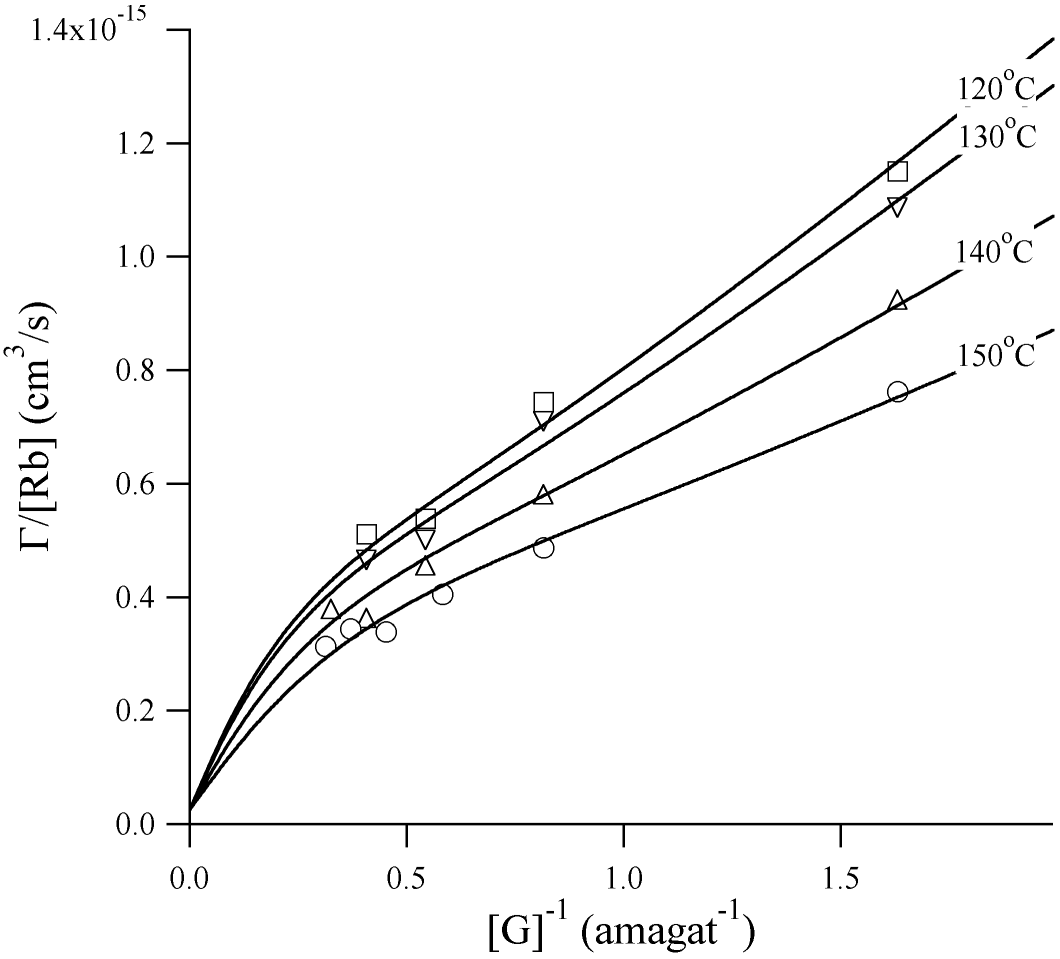

Figure 5.7: Spin-exchange rates at various temperatures and densities. For clarity, the four measurements at each point are averaged to produce a single data point with errors ∼10%.

$$\gamma_{SE}\Big|_{20°\mathrm{C}} = \frac{\mathcal{K}\alpha}{2\hbar x}\frac{[\mathrm{G}]_0}{[\mathrm{G}]_1}\Big|_{20°\mathrm{C}} = (1.16 \pm 0.16) \times 10^{-15}\mathrm{cm}^3/\mathrm{s} \quad (5.62)$$

$$\langle \sigma_{SE} v \rangle\Big|_{20°\mathrm{C}} = (2.2 \pm 2.5) \times 10^{-17}\mathrm{cm}^3/\mathrm{s} \quad (5.63)$$

$$[\mathrm{G}]_1\Big|_{120°\mathrm{C}} = 2.42 \pm 0.35 \text{ amagats} \quad (5.64)$$

$$\left[\mathrm{G}\right]_1\Big|_{130^\circ\mathrm{C}} = 2.36 \pm 0.34 \text{ amagats} \quad (5.65)$$

$$\left[\mathrm{G}\right]_1\Big|_{140^\circ\mathrm{C}} = 1.96 \pm 0.28 \text{ amagats} \quad (5.66)$$

$$\left[\mathrm{G}\right]_1\Big|_{150^\circ\mathrm{C}} = 1.57 \pm 0.22 \text{ amagats} \quad (5.67)$$

$$(5.68)$$

We can immediately compare these values of $[\mathrm{G}]_1$ to those obtained in section 5.2 (where $[\mathrm{G}]_1$ was obtained by observing Rb loss rates). Figure 5.8 contains both sets of values for $[\mathrm{G}]_1$, plotted vs. temperature. The fit shown is $\propto T^p$, where the temperature dependence $p = -2.64 \pm 0.60$. This large temperature dependence is somewhat surprising, as it represents a $T^{-2.64}$ temperature dependence to the van der Waals molecule correlation time (or lifetime, as we have assumed that the two are equivalent) at constant density. We might expect the lifetime to scale like the time between collisions from kinetic theory, $1/([\mathrm{G}]\sigma v)$, or like $T^{-1/2}$. Nevertheless, the agreement between the two data sets displayed in figure 5.8 is compelling.

This work represents the first measurement of $[\mathrm{G}]_1$ — there are no previous measurements in any gas composition with which to compare. We do, however, expect that $[\mathrm{G}]_1/[\mathrm{G}]_0 = 22.5$ (from previous measurements of $\gamma N/h$ [Wu85]). Ramsey *et al.* measured $[\mathrm{G}]_0$ in helium at $T = 85.3^\circ$C to be 0.21 amagats [Ramsey83]. Our 80°C spin loss measurements suggest $[\mathrm{G}]_0 = 0.10 \pm 0.01$ amagats at 80°C, while our $[\mathrm{G}]_1$ data suggest $2.9/22.5 = 0.13$ amagats, both significantly lower than the results of reference [Ramsey83].

We can also compare the binary cross section $\langle \sigma_{SE} v \rangle$ obtained here to previous work. Walker has made theoretical estimates of σ_{SE} [Walker89] from time dependent perturbation theory, obtaining 1.5×10^4 barns. Multiplying by a reasonable Rb-Xe relative velocity, 4×10^4 cm/s, yields $\langle \sigma_{SE} v \rangle \approx 6 \times 10^{-16}$. Cates *et al.* [Cates92] measured $\langle \sigma_{SE} v \rangle = 3.7 \times 10^{-16}$ by observing ^{129}Xe relaxation in the dark; however, their analysis

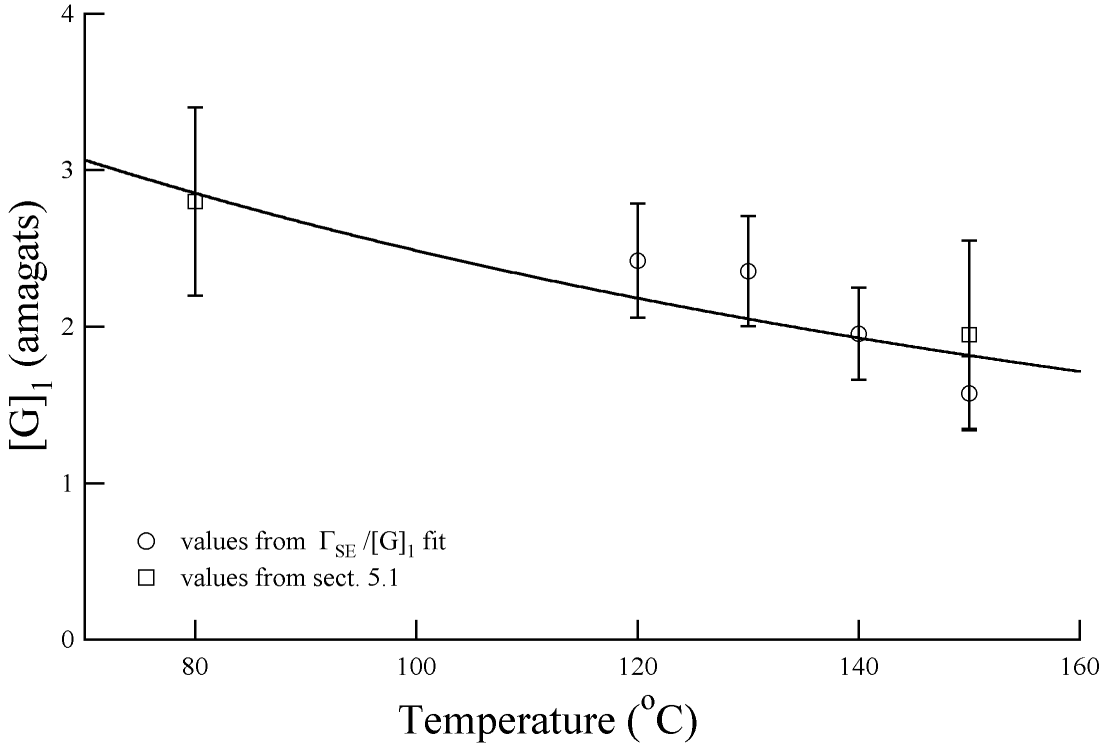

Figure 5.8: Characteristic density $[G]_1$ obtained by two different methods.

differs somewhat from our method. Zeng *et al.* [Zeng85] estimate $\langle \sigma_{SE} v \rangle = 4.1 \times 10^{-16}$ based on their measurements of van der Waals molecules and earlier measurements of $\langle \sigma v \rangle$, the binary Rb spin loss rate coefficient [Bouchiat72].

Though our measurement should properly be called an upper limit on $\langle \sigma_{SE} v \rangle$ owing to its large statistical error, the value of that upper limit, $\langle \sigma_{SE} v \rangle < 5.0 \times 10^{-17}$, is nearly an order of magnitude smaller than that obtained in any previous work. While it is unclear why the estimated rates of references [Walker89] and [Zeng85] disagree with the results obtained here, we feel that the analysis of reference [Cates92] may be neglecting nonnegligible temperature dependences of $\mathcal{K}$ and $\langle \sigma_{se} v \rangle$, and perhaps extrapolating data taken in the short van der Waals lifetime regime through the "very short" lifetime regime improperly. It is difficult to see, given our data and the high density behavior of Γ_{SE}, how $\langle \sigma_{SE} v \rangle$ could be as high as previously estimated to be.

Our measurements of $[\mathrm{G}]_1$ and knowledge of the ^{85}Rb hyperfine frequency immediately allow us to calculate the van der Waals molecule lifetime, τ:

$$\tau = \frac{[\mathrm{G}]_1}{[\mathrm{G}]} \frac{1}{\omega_{hf,85}} \tag{5.69}$$

$$= 0.103 \text{ ns} \cdot \text{amagats} \left(\frac{T + 273}{413} \right)^{-2.64}. \tag{5.70}$$

From this and $[\mathrm{G}]_0$ we can calculate $\gamma N/h$:

$$\frac{\gamma N}{h} = \frac{[\mathrm{G}]_0}{[\mathrm{G}]_1} \omega_{hf,85} \tag{5.71}$$

$$= 108.4 \text{ MHz}, \tag{5.72}$$

where we have used the characteristic densities as measured at 80°C. This is in fair agreement with measurements by Wu (135 MHz) [Wu85], Ramsey (120MHz) [Ramsey83] and Bhaskar (120 ± 10MHz) [Bhaskar83].

The ratio of Γ_{vdW} (see equation 5.15) to our fit parameter γ_{SE}, along with $[\mathrm{G}]_1$,

provides us with a measure of x:

$$\frac{\Gamma_{vdW}}{\gamma_{SE}} = \left(\frac{4}{3}x^2 + \eta_{129}\right)\frac{[\mathrm{Xe}]}{[\mathrm{G}]}[\mathrm{G}]_1 \tag{5.73}$$

or

$$x^2 = \frac{3}{4}\left(\frac{\Gamma_{vdW}}{\gamma_{SE}}\frac{[\mathrm{G}]}{[\mathrm{Xe}]}\frac{1}{[\mathrm{G}]_1} - \eta_{129}\right) \tag{5.74}$$

Our 150°C data yields $x = 2.2 \pm 0.3$, while our 80°C data yields $x = 1.9 \pm 0.2$, both substantially lower than previous measurements made by Zeng *et al.* [Zeng85], $x = 3.2 \pm 0.3$. In that work, the authors calculated x from measured [Rb] and the ratio of Rb decay rates to ^{129}Xe decay rates. It may or may not be significant that that work was performed at gas densities below $[\mathrm{G}]_0$ (in the long lifetime regime), where F-damping transitions are dominant and contributions to both decay rates from binary collisions are small.

From x and $\gamma N/h$, we find

$$\frac{\alpha}{h} = \frac{\gamma N}{h}\frac{1}{x} \tag{5.75}$$

$$= 57 \text{ MHz}. \tag{5.76}$$

Note that this value depends upon four fit parameters, $[\mathrm{G}]_0$, $[\mathrm{G}]_1$, Γ_{vdW}, and γ_{SE}. This value is significantly higher than that reported elsewhere [Bhaskar83] because our value for x is significantly lower [Zeng85].

Finally, using equation 5.15 and the same four fit parameters, we obtain $\mathcal{K}$ at 80°C:

$$\mathcal{K}|_{80°C} = 6.76 \times 10^{-3} \text{ amagats}^{-1} \tag{5.77}$$

$$= 2.51 \times 10^{-22} \text{ cm}^3, \tag{5.78}$$

smaller than the value obtained by Bhaskar *et al.*, 9.4×10^{-22} [Bhaskar83]. Walker has previously used semiempirically calculated RbXe potentials to estimate $\mathcal{K}$ to be 310 Å^3

at 100°C [Walker89] — scaled by $T^{-3/2}$ to 80°C this is 3.37 $\times 10^{-22}$ cm^3, in reasonably good agreement with our result.

This work represents the first measurement of $\langle \sigma_{SE} v \rangle$ using rubidium number densities measured in this way. As an exercise, we also refit our data using [Rb] from the vapor pressure curve of Killian [Killian26]. Because the $[\mathrm{G}]_1$'s were not determined by this fit, we fixed the $[\mathrm{G}]_1$'s at values from figure 5.8. The revised data and fit are displayed in figure 5.9. That fit yields

$$\gamma_{SE}\Big|_{20^\circ\mathrm{C}} = \frac{\mathcal{K}\alpha}{2\hbar x}\frac{[\mathrm{G}]_0}{[\mathrm{G}]_1}\Big|_{20^\circ\mathrm{C}} = (7.45 \pm 0.43) \times 10^{-16}\mathrm{cm}^3/\mathrm{s} \quad (5.79)$$

$$\langle \sigma_{SE} v \rangle\Big|_{20^\circ\mathrm{C}} = (4.3 \pm 1.9) \times 10^{-17}\mathrm{cm}^3/\mathrm{s} \quad (5.80)$$

This γ_{SE} is ∼70% of that obtained using the measured number densities. From equation 5.74, this would have the effect of raising x^2 to 6.2, or x to 2.5, in closer agreement with previous work. This value of $\langle \sigma_{SE} v \rangle$, though slightly larger than that obtained using measured number densities, is within error bars of that value, and does little to bring this work into agreement with previous estimates and measurements.

It is worth noting again here that we assumed in fitting our data that the spin exchange rate significantly exceeded any other ^{129}Xe relaxation rate in our system. Including a [Rb]-independent rate Γ' would have an unusual effect on the data, as it is $\Gamma/[\mathrm{Rb}]$ which is plotted in figure 5.7. Including a constant Γ' leads to an offset, $\Gamma'/[\mathrm{Rb}]$, which is constant within each constant temperature curve (it would not change each slope, $\gamma_{SE}[\mathrm{G}]_1$), but which would be nearly 10× larger at 120° than at 150°). The excellent fit to the data as well as the agreement with the Rb spin loss data (sect. 5.2) seem to argue against the presence of such an offset. Also, the effect of such an offset introduced to the fit is only to make $\langle \sigma_{se} v \rangle$ smaller and even less in agreement with previous work. A ^{129}Xe relaxation rate proportional to [Rb] would be indistinguishable in our experiment from ^{129}Xe-Rb spin exchange, and so would tend to decrease x;

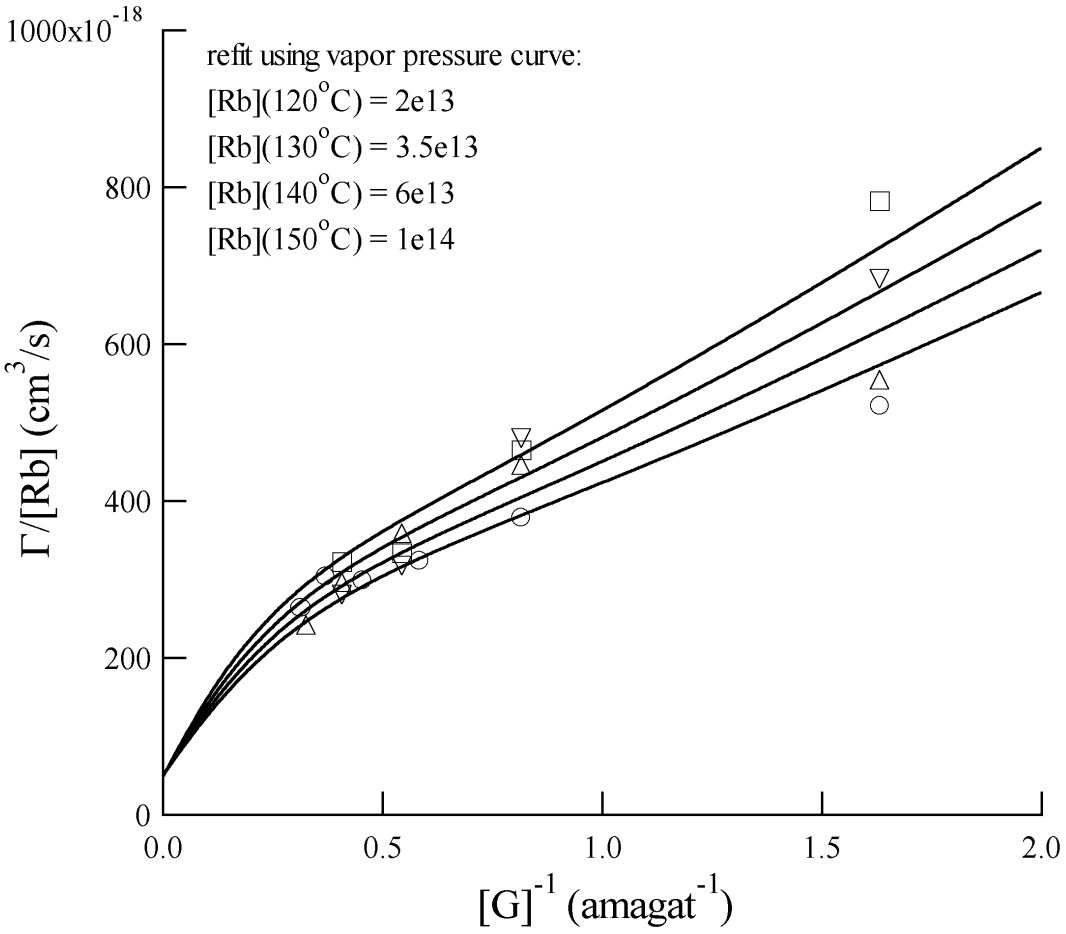

Figure 5.9: Data of figure 5.7 refit using [Rb] from vapor pressure curve rather than the measured values.

however, we know of no such relaxation mechanism.

5.3 NMR Calibration and Spin Exchange Efficiency

Though they have proven to be highly interesting themselves, our original motivation for these spin loss and spin exchange measurements was a calibration of our NMR system. Equation 5.56 illustrates how a knowledge of the Rb polarization (in spin temperature equilibrium) and the rates we have measured allows us to calculate the ^{129}Xe polarization:

$$\langle K_z \rangle = \langle S_z \rangle \frac{\Gamma_{SE} + \Gamma_{SD}}{\Gamma_{SE}}. \tag{5.81}$$

We can then measure the FID voltage V_{FID} following a pulse from our NMR coil, and thereby calibrate an NMR signal to a nuclear polarization.

We can also use the results of the previous sections to obtain the spin-exchange efficiency for RbXe, which is simply the ratio of the spin-exchange and spin-relaxation rates. In the spin-temperature limit, the spin-exchange rate equations become

$$\frac{d\langle F_z \rangle}{dt} = R\left(\frac{1}{2} - \langle S_z \rangle\right) - \Gamma \langle S_z \rangle + \eta_{129}\kappa_{SE}[\mathrm{Xe}]\langle K_z \rangle \tag{5.82}$$

$$\frac{d\langle K_z \rangle}{dt} = \kappa_{SE}[\mathrm{Rb}]\left(\langle S_z \rangle - \langle K_z \rangle\right) \tag{5.83}$$

where $R(1 - 2\langle S_z \rangle)$ is the rate at which the atoms absorb photons from the laser. The spin exchange rate coefficient, κ_{SE}, is exactly what was measured in section 5.2 ($\kappa_{SE} = \Gamma_{SE}/[\mathrm{Rb}]$), and Γ is the Rb spin loss rate measured in section 5.1. The spin-exchange efficiency is defined as the ratio of the initial rate of increase of angular momentum stored in the nuclei to the steady-state rate at which photons are deposited into the vapor:

$$\epsilon = \left.\frac{[\mathrm{Xe}]d\langle K_z \rangle/dt}{[\mathrm{Rb}]R(1 - 2\langle S_z \rangle)}\right|_{\langle K_z \rangle = 0} = \frac{\eta_{129}\kappa_{SE}[\mathrm{Xe}]}{2\Gamma} \tag{5.84}$$

The factor of 2 arises from the Rb optical pumping process, so we can define a collisional efficiency

$$\epsilon_c = \eta_{129}\kappa_{SE}[\mathrm{Xe}]/\Gamma. \tag{5.85}$$

In practice, we have combined these two measurements. We measured V_{FID}, Rb polarization P_a, and the Rb repolarization P_a' at five different gas densities at 150°C. Again, in order to avoid heating the cell with the pump beam, we used only a fraction of the available power (≈3 Watts). As a result, the ^{129}Xe polarizations attained were fairly low (typically ≈5%). This, coupled with the already lean ^{129}Xe gas mixture ($\eta_{129} \times 1\% = 0.264\%$), made the FID signals quite small; an example of a single frequency domain FID appears in the inset of figure 5.10. We therefore averaged 10 of these frequency domain signals (see figure 5.10) and calculated V_{FID} from the resulting trace (as described in section 2.4). We then calculated P_a'/V_{FID} at each point and fit these points to the efficiency obtained from equation 5.85 and our rates measured in the previous sections (at 150°C), with a constant of proportionality as the free parameter. This constant of proportionality then gives us the scaling factor between V_{FID} and P_{Xe}, good to 5%:

$$^{129}\mathrm{Xe\ Polarization\ (\%)} = 55.8 \times V_{FID}\ \mathrm{(volts)}. \tag{5.86}$$

The rescaled points are shown in figure 5.11, along with the collisional efficiency predicted from our measured rates.

Also included in figure 5.11 are experimental lower limits on ϵ_c, obtained by measuring the ratio P_a'/P_a. This is a lower limit since the probe samples the center of the cell, which presumably is the region with the highest Rb polarization when the light is on. With the light off, the Rb polarization should be very isotropic since it is being produced by the isotropic ^{129}Xe polarization. The experimental lower limits are about 10% lower than the efficiency predicted from the separate loss and spin-exchange mea-

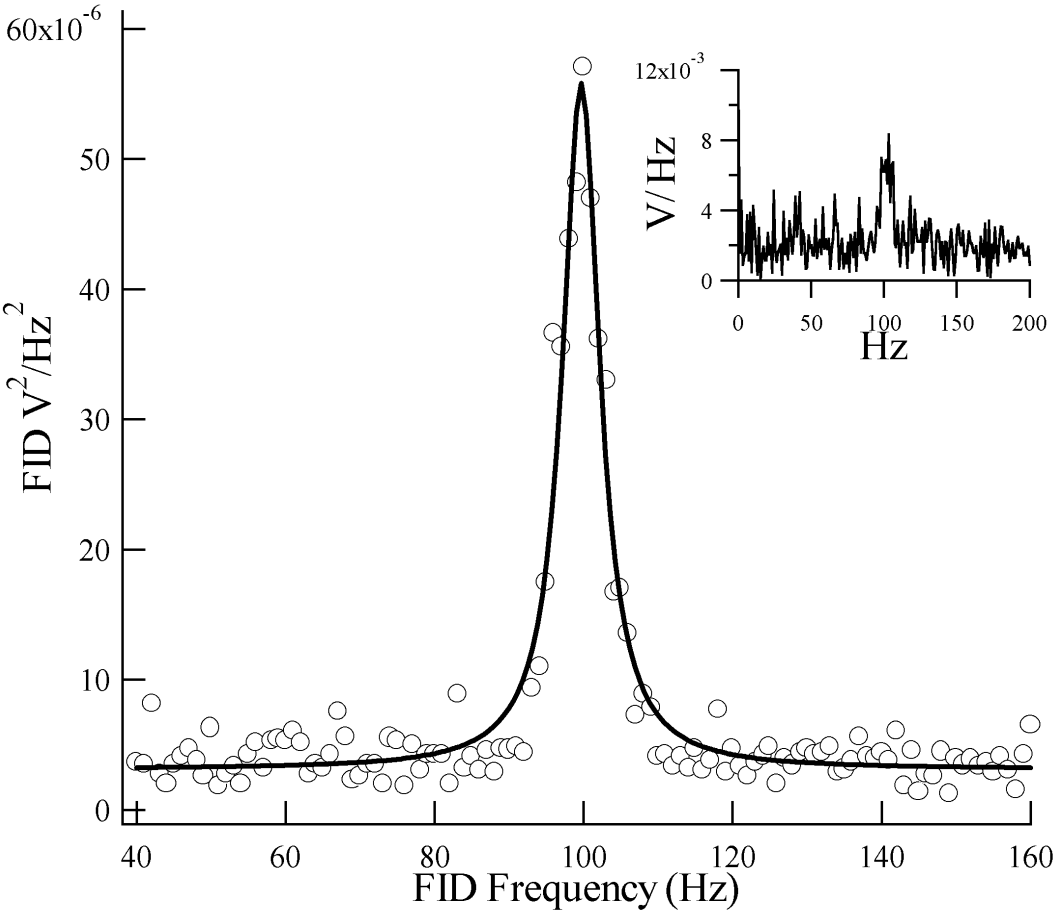

Figure 5.10: Average of 10 frequency domain FID signals. The inset shows an example of the individual FIDs.

surements. Note that obtaining these lower limits does not involve either a Rb vapor pressure measurement or an NMR calibration — it is simply the ratio of the Faraday rotation angles with the pump on vs. off, and as such is an extremely robust limit. Expanding the probe beam to fill the entire cell to obtain the volume averaged Rb polarization with the light on vs. off would make efficiencies measured this way no longer lower limits but robust efficiency measurements.

These efficiency measurements serve three purposes: they provide a check on the earlier measurements, they provide a ^{129}Xe NMR calibration, and, perhaps most importantly, they underscore the dramatic pressure dependence of the spin exchange efficiency. The efficiency decreases rapidly with pressure essentially because the Rb spin loss process is dominated by Rb-Xe binary collisions (rate proportional to gas density), while the spin exchange process is dominated by van der Waals molecules (rate independent of gas density within each lifetime regime).

5.4 Conclusions

The measurements in this section represent the first systematic measurements of spin loss and spin exchange rates of Rb atoms in He-dominated buffer gas mixtures of Xe, He, and N_2. We have observed for the first time the transition from the short to "very short" molecular lifetime regime for van der Waals molecules. Our spin loss results agree with two recent measurements at a single pressure, using RF spectroscopy, of spin loss rates in high pressure spin-exchange optical pumping experiments. Our spin exchange measurements in particular suggest that the present spin exchange optical pumping theory is inadequate for predicting fundamental rate parameters (*e.g.* $\langle \sigma_{SE} v \rangle$). The surprising temperature dependences suggested by our data also are not predicted by current theory. These results will be useful for modeling and for the design of Rb-^{129}Xe

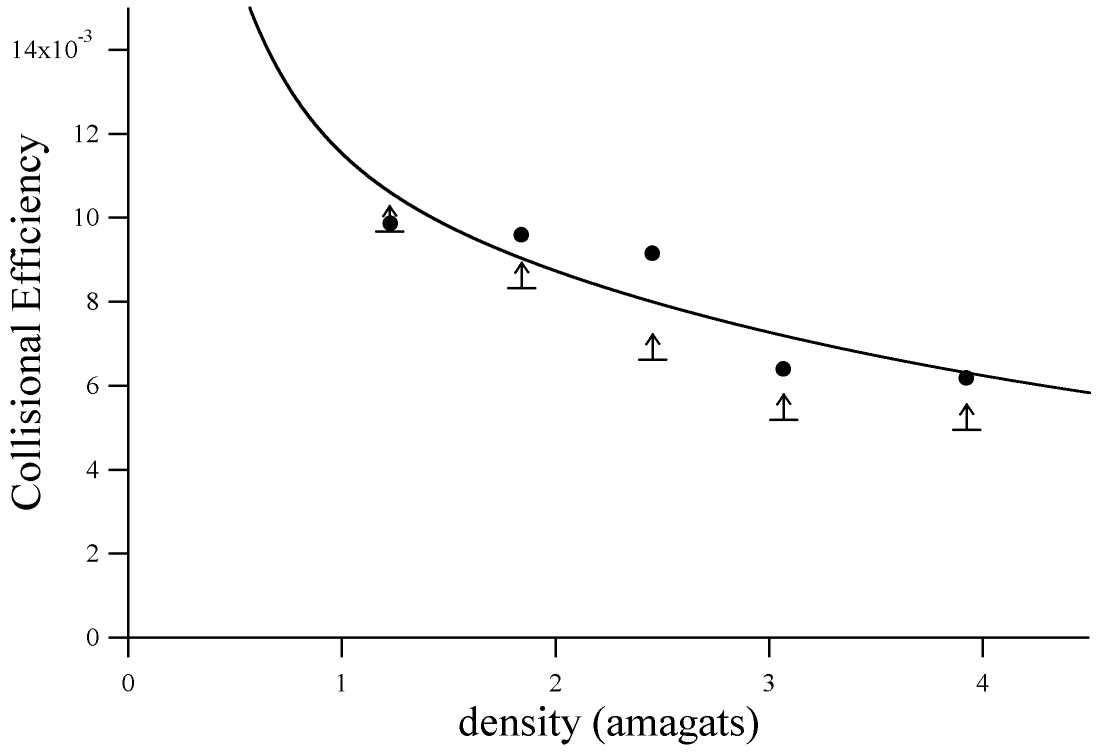

Figure 5.11: The solid line is the collisional spin-exchange efficiency at 150°C deduced from measurements of Fig.5.1 and Fig.5.7, for natural abundance Xe in a 1% Xe mixture. Arrow symbols are experimental lower limits on the efficiency found from the ratio of the Rb polarization with and without the optical pumping laser on. Filled circles are absolute collisional efficiencies (with the ^{129}Xe NMR signal calibrated via comparison to the solid line.

polarizers.

Chapter 6

Implications

Throughout this work, a common theme has been basic physics research with immediate impact on a practical problem: maximizing production of hyperpolarized gas (^{129}Xe in particular). With this in mind, this chapter is meant to clarify just what that impact is expected to be.

The current state of the art hyperpolarized ^{129}Xe production system, as utilized for example in references [Shah00] and [Baranga98b], is first described in reference [Driehuys96]. The gas mixture in these systems is either identical or similar to that which we have studied (1% Xe, 1% N_2, and 98% He), and gas pressures quoted are 7-10 atmospheres. Optical pumping light is provided by fiber coupled diode laser arrays, typically providing 60-140 Watts of power with ~2 nm linewidth. Oven temperatures quoted are 130°C-180°C.

These systems have been designed to optimize production of hyperpolarized ^{129}Xe constrained by the best available 1) technology, 2) theoretical understanding, and 3) measurements. The biggest technological constraint has been the lack of availability of high power, narrow linewidth lasers. The high power diode arrays currently commercially available necessitate the use of high ^{4}He pressures and high temperatures in

order to absorb a significant fraction of the light due to their ∼2 nm linewidths, as first described in [Driehuys96].

The problem associated with the currently understood theory is that it fails to predict the actual performance of systems in the references above. The ^{129}Xe polarization measured in reference [Shah00], for example, is less than a third of the volume averaged Rb polarization measured. Though this suggests that the (wall) relaxation time of the ^{129}Xe atoms is less than the spin exchange time, the authors of that reference imply that the spin exchange time is expected to be much shorter. They postulate a wall relaxation mechanism which increases with temperature in such a way as to always maintain $\Gamma_{SE} < 1/T_w$.

Perhaps the major problem with applying the theory to model polarizer performance is that nearly all of the fundamental rates needed had previously been measured at vastly lower pressures and/or temperatures. For example, the first (and only, until this work) measurements of $\langle \sigma v \rangle$ [Bouchiat72] were conducted at 27° and at pressures less than 1 Torr. The work of reference [Ramsey83], measurements of $[\mathrm{G}]_0$ for He and N_2, also were done at a much lower temperature (85.3°C) than is common in current polarizers. In addition, no measurements of temperature dependences of any of the fundamental rates are to be found in the literature — our work is the first of any kind. Previously, best guesses at temperature dependences had been made for the sake of modeling higher temperature systems.

6.1 Implications for Modeling

The measurements we present in this work, in particular the surprisingly large temperature dependences and small binary spin exchange rate coefficient, seem to suggest that models based on previous measurements should overestimate ^{129}Xe polarizations

(at least in systems similar to ours at high temperatures and pressures). As a means of illustrating this, we have used our data with its suggested temperature dependences to calculate collisional spin exchange efficiency vs. density at various temperatures. For the purpose of generating these estimates, we have assumed $T^{-2.64}$ temperature dependences for $[\mathrm{G}]_1$ and Γ_{vdW} (as suggested by the data of section 5.1.1), $T^{-3/2}$ for γ_{SE}, and $T^{1/2}$ for both binary rate coefficients $\langle\sigma v\rangle$ and $\langle\sigma_{SE} v\rangle$. Figure 6.1 shows the resulting efficiencies.

We can recalculate each efficiency curve making only the following changes: replace our measured $\langle\sigma v\rangle$ with that measured in reference [Bouchiat72], and replace our $\langle\sigma_{se} v\rangle$ with that measured in reference [Cates92]. This change to $\langle\sigma v\rangle$ increases the efficiency by a factor approximately equal to the ratio of the two $\langle\sigma v\rangle$'s ($\sim$1.5), because the Rb spin loss is dominated by binary collisions in either case. The change we have made to $\langle\sigma_{se} v\rangle$, however, has a much more dramatic result. Our value of $\langle\sigma_{se} v\rangle$ suggests that van der Waals molecules dominate spin exchange (with the associated large temperature and pressure dependences), while that of reference [Cates92] suggests a balance between molecules and binary collisions. The ratio of the two efficiency curves (using previously measured rate coefficients vs. using our measurements) appears in figure 6.2.

We suggest that the disagreement between previous models and polarizer performance may be explained by figure 6.2: our predicted efficiency for typical polarizer temperatures and gas densities is approximately a factor of five smaller than that predicted based upon previous measurements. In addition, our measurements suggest that the efficiency itself drops off much faster with temperature than was previously thought. It may be this fundamental rate limitation which has served to keep ^{129}Xe polarizations low even as Γ_{SE} is increased by increasing [Rb] (*i.e.* by increasing *temperature*).

Issues related to temperature dependent efficiencies are compounded in light of recent work measuring gas temperature (as opposed to oven or exterior cell temperature)

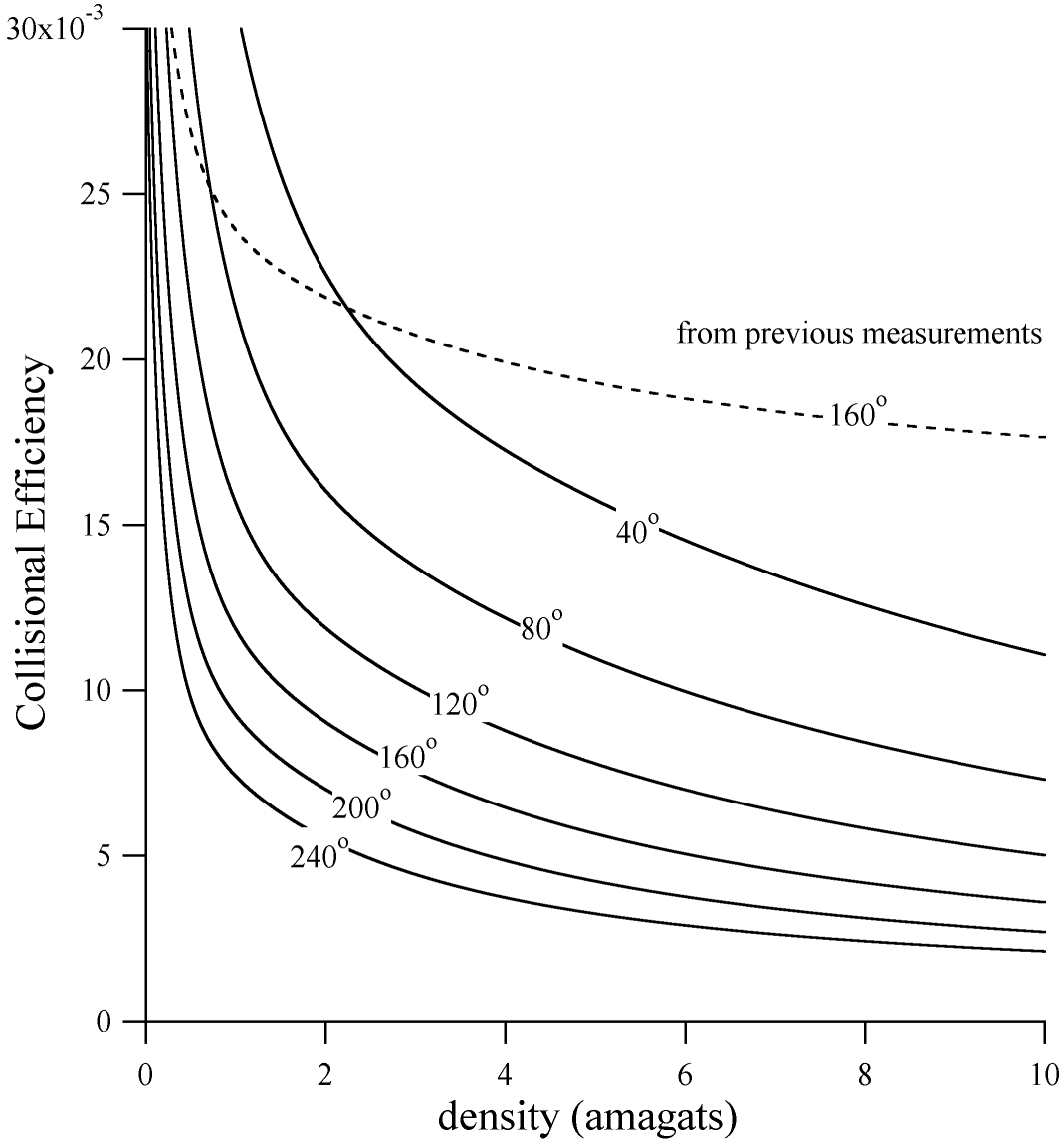

Figure 6.1: Collisional efficiency vs. gas density for several cell temperatures.

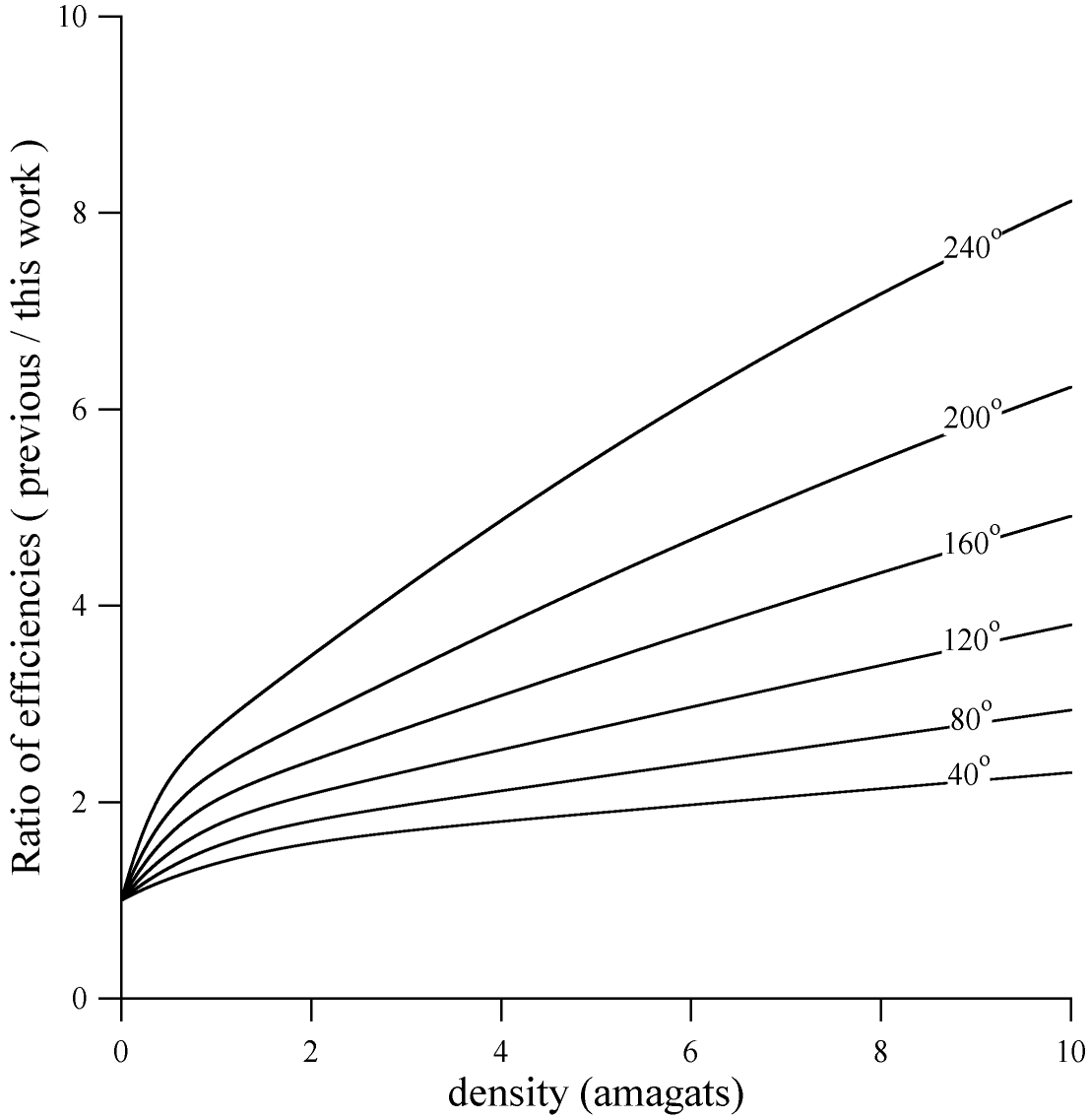

Figure 6.2: Ratio of efficiencies calculated using previously measured binary rate coefficients ($\langle \sigma v \rangle$ and $\langle \sigma_{se} v \rangle$) to those calculated using our measured values.

in a spin exchange optical pumping system pumped by a high power diode array [Walter01]. In that reference, the gas temperature (as measured via rf spectroscopy on the N_2 buffer gas vibrational levels) was observed to increase initially by as much as 10° for each Watt absorbed (until convective processes set in). When it is considered that 30-50 Watts are routinely absorbed in ^{129}Xe polarizing systems, the effect on efficiency may be dramatic. We emphasize here that though [Rb] is likely set by the cell *wall* temperature, our estimated temperature dependences of the efficiencies are with respect to the *gas* temperature — under conditions of high power absorption, the average gas temperature may exceed the cell wall temperature by over 100°, reducing efficiency accordingl y.

It is clear that the temperature dependences of the spin exchange optical pumping parameters must be accounted for when modeling real systems. Our work is the first step in this direction.

6.2 Implications for Polarizer Design

From figure 6.1, it appears that it is desirable to work at the lowest densities and temperatures possible. Our introduction of high power external cavity diode laser arrays (ECDLA's, see section 4.2) makes it feasible to lower the densities and temperatures while still maintaining sufficient optical pumping rate R_p. Just as present polarizing systems were designed largely around the broad linewidth high power diode arrays, we present a redesign around our narrow linewidth ECDLA's.

It is instructive to reframe the spin exchange optical pumping equations, presented first in the introduction of this work, in more fundamental terms. From the expression

for the polarization of the Rb atoms,

$$P_{Rb} = \frac{R_p}{R_p + \Gamma} \tag{6.1}$$

and the expression for circular dichroism (with N_ν as the number of photons absorbed per second in the cell volume V),

$$N_\nu = R_p(1 - P_{Rb})[\mathrm{Rb}]V, \tag{6.2}$$

we can relate laser absorption to Rb polarization:

$$N_\nu = P_{Rb}\Gamma[\mathrm{Rb}]V. \tag{6.3}$$

So for $P_{Rb} = 1$, the number of photons absorbed per Rb atom exactly makes up for the polarization loss rate, Γ (this is the upper limit on the number of photons which can be absorbed). If the absorption falls behind, the polarization drops.

We can reframe the expression for the polarization of the ^{129}Xe atoms in a similar manner:

$$P_{Xe} = \frac{\kappa_{SE}[\mathrm{Rb}]}{\kappa_{SE}[\mathrm{Rb}] + \Gamma_w} P_{Rb} \tag{6.4}$$

leads to

$$\kappa_{SE}[\mathrm{Rb}] = \frac{P_{Xe}}{P_{Rb} - P_{Xe}} \Gamma_w. \tag{6.5}$$

Again, the rate at which spin is added ($\kappa_{SE}[\mathrm{Rb}]$) must balance the rate at which it is lost (Γ_w).

Equations 6.3 and 6.5 together, along with the definition of the collisional efficiency ϵ_c, yield a fundamental relation relating the various parameters of the spin exchange optical pumping system:

$$\frac{P_{Xe}}{1 - P_{Xe}/P_{Rb}} \eta_{129}[\mathrm{Xe}]V\Gamma_w = N_\nu \epsilon_c. \tag{6.6}$$

There are obviously many interconnected system parameters to be varied: gas density, temperature, cell volume, and the cell area presented to the pumping laser (this

parameter affects not only laser absorption, but also affects the cell surface area to volume ratio (recall that this sets Γ_w through the relaxivity, ϱ). Also, the figure of merit for practical ^{129}Xe polarizer systems used for different applications is not always the same; it is some combination of P_{Xe} and κ_{SE}[Rb], the rate at which the ^{129}Xe is produced. The following is meant to serve only as one example of system design.

We start with two design constraints: 1) we will assume that we can absorb up to 10 Watts of laser power (corresponding to 4×10^{19} photons per second), and 2) we will constrain ourselves to total gas densities greater than 1.0 amagat and temperatures greater than 80°C. The constraints on density and temperature are largely to make the absorption assumption realizable — we must keep Rb number densities reasonably high and pressure-broadened absorption linewidths reasonably large.

Equation 6.3 serves as a density and temperature dependent limit on the volume of our cell. Choosing $P_{Rb} = 1$ as a target polarization,

$$N_\nu = \Gamma[\mathrm{Rb}]V \tag{6.7}$$

or,

$$V = \frac{N_\nu}{\Gamma[\mathrm{Rb}]} \tag{6.8}$$

$$\tag{6.9}$$

This is actually an upper limit on V, as reducing V simply reduces the Rb spin loss rate, and we absorb less light; increasing V reduces the Rb polarization because we have assumed a maximum 10 Watts absorption. Because Rb spin loss is dominated by binary collisions, this limit is approximately inversely proportional to gas density. This maximum volume is plotted in figure 6.3 as a function of temperature for five different densities: 1,3,5,7, and 9 amagats.

We can also get a limit on the number of gas atoms from equation 6.5. Choosing

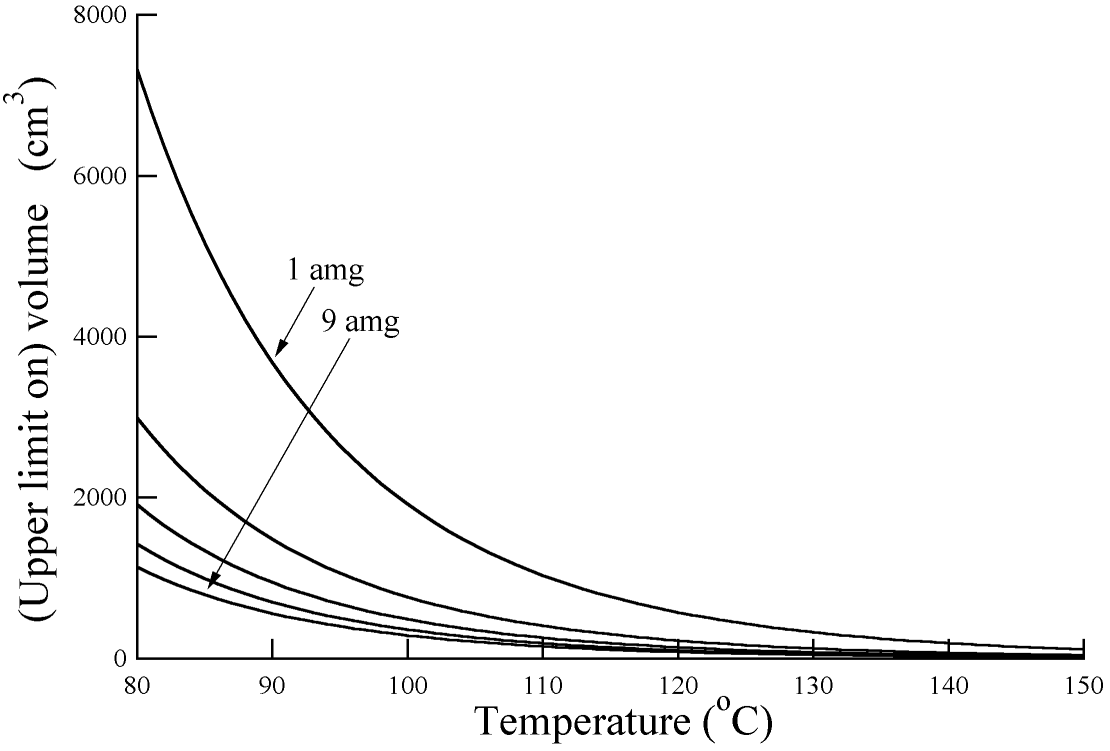

Figure 6.3: Upper limit on the volume of the spin exchange cell for 10 Watts laser absorption. (Note that this volume limit is proportional to laser absorption.)

$P_{Xe} \approx 1/2$,

$$[\mathrm{G}]V = \frac{200 N_\nu \epsilon_c}{\eta_{129} \Gamma_w}. \tag{6.10}$$

Now we assume that by keeping the cell temperature relatively low and by absorbing only 10 Watts, we make it possible to use a cell coated with a siliconizing agent such as SurfaSil, which extends the ^{129}Xe relaxation time (there is some evidence that these coatings degrade quickly at high temperatures). We will therefore assume a relatively long $1/\Gamma_w = 1$hour:

$$[\mathrm{G}]V < 10^{26} \epsilon_c. \tag{6.11}$$

This limit is more sensitive to gas density than to temperature in our range of interest. We find that, owing to the long wall relaxation time we have assumed, this limit is not as restrictive as that of equation 6.9. We will later see just how much this assumption can be relaxed.

Another parameter of interest to us is the rate at which the ^{129}Xe is polarized, $\kappa_{SE}[\mathrm{Rb}]$. Though [Rb] increases rapidly with temperature, this is partially offset by the behavior of κ_{SE}, a decreasing function both of temperature and pressure over our range of interest. $\kappa_{SE}[\mathrm{Rb}]$ is plotted in figure 6.4. Note that we must keep the spin exchange rate higher than the wall relaxation rate in our cell (2.8×10^{-4} s^{-1}), but this is not a limiting factor in our range of interest: $\kappa_{SE}[\mathrm{Rb}](\mathrm{at}80°\mathrm{C}, 1\mathrm{amg}) = 1.67 \times 10^{-3}$. We will assign a figure of merit, $[\mathrm{G}]V\Gamma_{SE}$, for our system, which is [G]/[Xe] = 100 times the number of ^{129}Xe atoms polarized per second. This quantity is plotted in figure 6.5.

It is obvious from figure 6.5 that, owing to the temperature and density dependence of the spin exchange rate, it is desirable to design our system to operate at the lowest temperature and density possible. We will therefore choose to operate at 80°C and 1 amagat gas density. Figure 6.3 then prescribes a 7000 cm^3 (7 liter) cell. With these

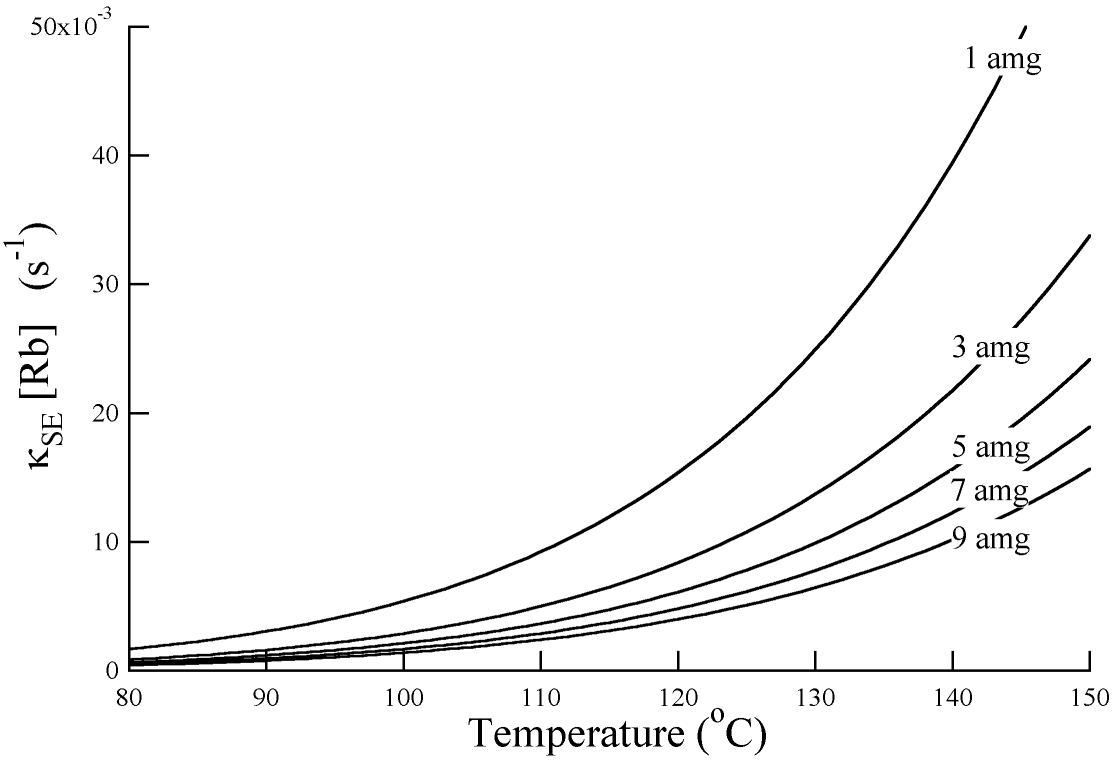

Figure 6.4: Spin exchange rate for Rb-Xe.

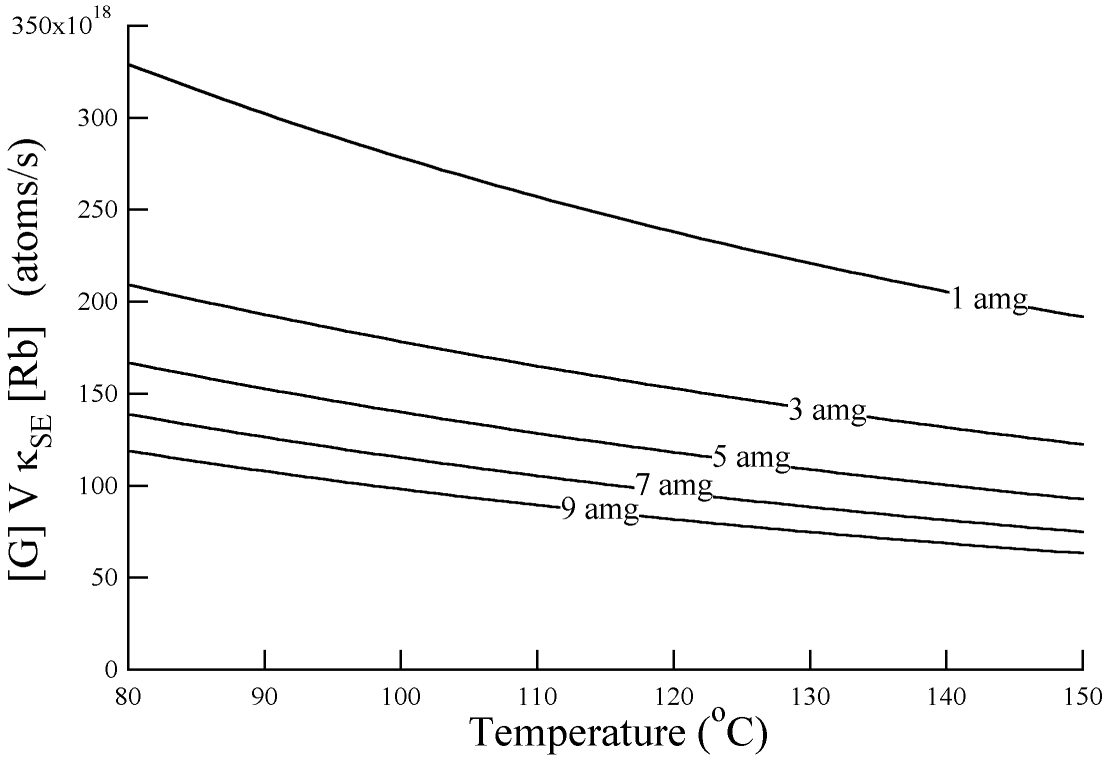

Figure 6.5: Figure of merit, atoms polarized per second, plotted vs. temperature at several gas densities.

parameters, we should be able to produce hyperpolarized Xe at a rate of 3.2×10^{18} atoms per second (1% of the value read from figure 6.5), or 420 cm^3 per hour.

A cylindrical cell is desirable because the flat end windows allow good optical access. There are two considerations relevant to choosing the aspect ratio: laser absorption and internal heating due to the absorption. We first treat the heating. Assuming that it is the conductivity of the gas itself which limits the rate at which heat leaves the cell, we must solve the heat diffusion equation for the temperature rise in the cell:

$$\mathcal{X}\nabla^2 T = -Q, \tag{6.12}$$

where Q is the power per volume per time which we add to the (center of the) cell (10 Watts per 7000 cm^3), and $\mathcal{X}$ is the thermal conductivity of He at 80°C, 1.649 mW·cm^{-1}°K^{-1} [CRC].

First we assume a flattened, pancake like cell. The thermal gradient will then be along the optical axis, $\hat{z}$ (see figure 6.6). For simplicity, we assume a quadratic variation of the temperature along z, where the length of the cell is L. For $z < L/2$,

$$T(z) = \frac{a}{2}\left(\left(\frac{L}{2}\right)^2 - z^2\right) + T_{oven} \tag{6.13}$$

Then $a = Q/\mathcal{X} = 0.87$ °K/cm^2, and the temperature rise at the cell center is

$$\delta T = T(0) - T_{oven} = \frac{aL^2}{8} \tag{6.14}$$

To keep the temperature rise less than 10°K, we need $L < 9.6$ cm.

Alternatively, we could assume an elongated cylinder for the cell shape. The thermal gradient is then radial, along $\hat{r}$. The diffusion equation in cylindrical coordinates is

$$\mathcal{X}\nabla^2 T(r) = \mathcal{X}\frac{1}{r}\frac{\partial}{\partial r}\left(r\frac{\partial T}{\partial r}\right) = Q. \tag{6.15}$$

We again choose a quadratic variation for $T(r)$ for simplicity:

$$T(r) = \frac{a}{4}\left(\left(\frac{D}{2}\right)^2 - r^2\right) + T_{oven}, \tag{6.16}$$

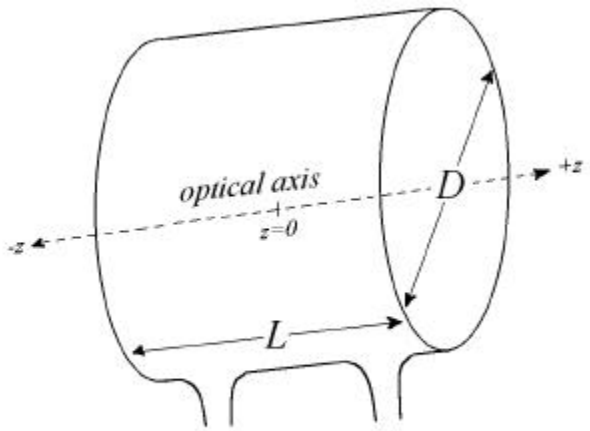

Figure 6.6: Cylindrical cell dimensions: "pancake" cell is assumed to have $D \gg L$ for heat removal calculations, while elongated cell has $L \gg D$.

where D is the cell diameter. Once again $a = Q/\mathcal{X}$, but with the heat able to diffuse radially, the temperature rise at the center of the cell is only half as large. Our requirement to keep the temperature rise less than 10°K is then $D < 18$ cm.

We have written a short numerical model to illustrate the laser absorption and Rb polarization for each case. The input parameters of the model are [G], T, laser power, laser linewidth, cylindrical cell area, and cylindrical cell length. (We use the measurements of chapter 5 to set the spin loss and spin exchange rates, so the relative composition of the gas can not be varied.) For the purposes of modelling, the cell is divided into 100 slices along its length. At each slice, the pumping rate is evaluated from the laser intensity, laser linewidth, and the pressure broadened Rb linewidth. The Rb polarization in that slice is calculated from the pumping rate and the loss rate. The intensity absorbed by that slice is then subtracted from the laser profile and the model steps ahead to the next slice.

We first apply the model to the pancake cell. As prescribed by our calculations, we take [G]=1 amagat, $T = 80$°C, and cell dimensions $L = 10$ cm (to keep $\delta T < 10°$)

and $D = 30$ cm, so as to make a 7 liter volume. The light source is assumed to be an ECDLA, with 20 Watts of output with a spectral profile taken to be a Gaussian with 100 GHz FWHM. Figure 6.7 shows the model output, the amount of laser absorption and both the pumping rate and Rb polarization as a function of z.

For the 7 liter elongated cylinder, we take $D = 18$ cm (to keep $\delta T < 10°$), $L = 27.5$ cm. We run the model with other input parameters unchanged, and obtain the results shown in figure 6.8. The results are measurably better in this case.

In fact, both the Rb polarization and absorption (photons per second per Rb atom) are monotonically increasing functions of L for constant cell volume, approaching 1 and Γ respectively. Of course, this is just equation 6.3. The number of photons taken out of the beam per Rb atom is simply equal to the Rb loss rate, a constant, times the Rb polarization, a function of the pumping rate. The laser is obviously more intense if the cell is more elongated, yielding a larger R_p and therefore a larger Rb polarization.

Though heat removal and laser absorption are both facilitated by elongating the cell at a given volume, the wall relaxation time for ^{129}Xe atoms is not. Still, with a cell this large, the surface to volume ratio is extremely favorable. Even for an extremely elongated 5 cm diameter, 350 cm long cylindrical cell (yielding 98% average Rb polarization, from the model output), the relaxivity of the wall need only be lower than 1.73×10^{-3} cm/s to produce 50% ^{129}Xe polarization.

This design represents a fairly radical departure from past designs [Driehuys96] [Shah00] [Baranga98b] , which is made practical by our ECDLA. We have taken advantage of its narrow linewidth as well as the fundamental rates' density and temperature dependences which we have measured. The system described should be capable of producing polarized ^{129}Xe at a rate of 1/3 liters per hour and at 80% polarization or greater (subject to the cell wall relaxivity). This production rate is comparable to or greater than those of high temperature systems, and we expect that by avoiding high

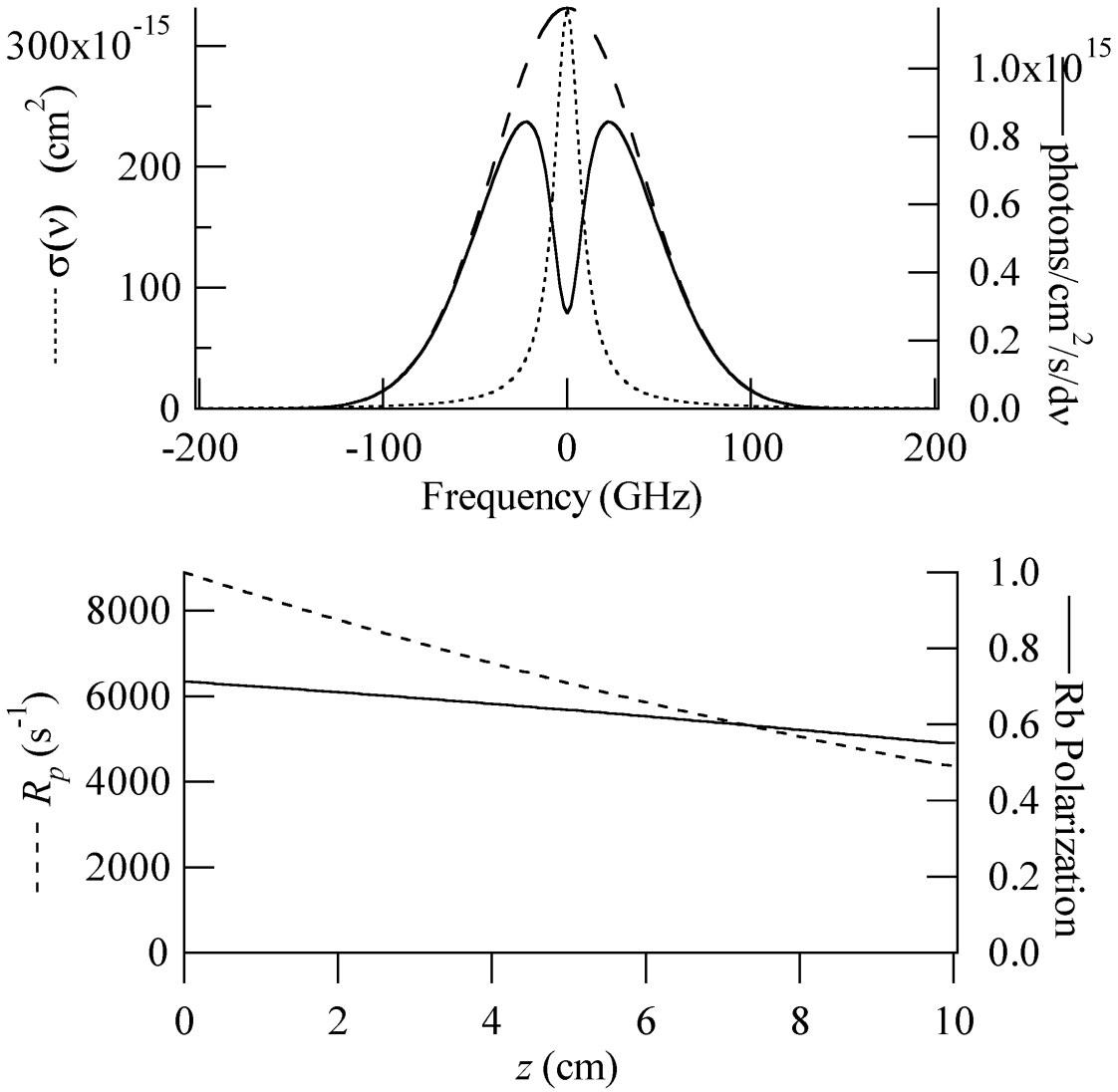

Figure 6.7: Model output for the pancake cell. The upper graph shows the laser spectral profile before (long dashed line) and after (solid line) traversing the cell. The Rb absorption cross section is shown for comparison. The lower graph shows the pumping rate (dashed line) decreasing slowly as a function of distance through the cell and the resulting Rb polarization (solid line).

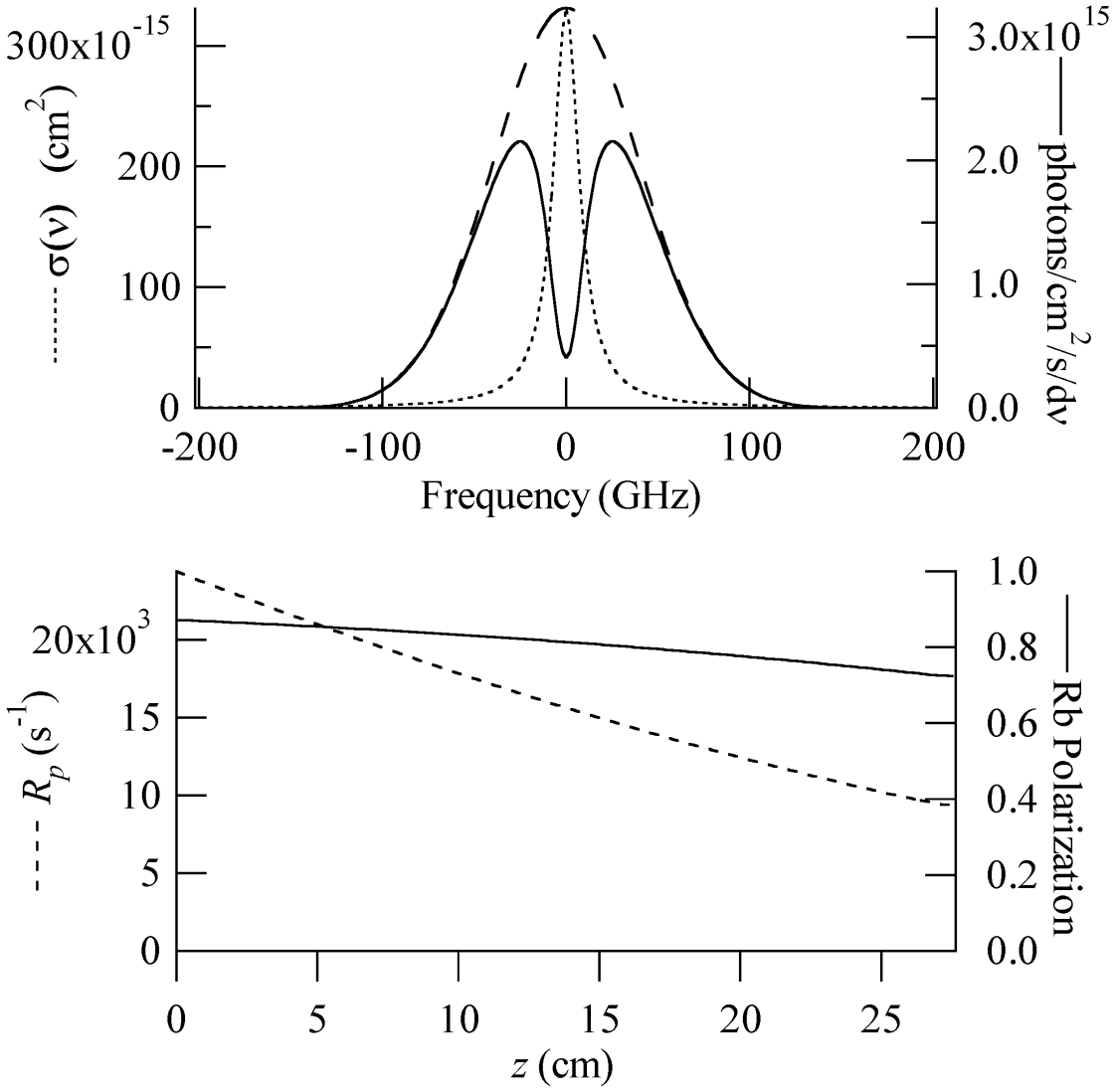

Figure 6.8: Model output for the elongated cylindrical cell.

temperatures the ^{129}Xe polarization produced will be much greater as well.

Chapter 7

Conclusion

Through the course of the studies described in this thesis, we have addressed the three main problems facing spin exchange optical pumping systems: pumping light sources, surface relaxation mechanisms, and fundamental rate measurements.

Our external cavity diode laser array (ECDLA) provides a much needed narrow bandwidth high power light source for optical pumping. Its application makes it possible to pump lower temperature, lower pressure spin exchange cells, thereby increasing the efficiency of the system as a whole.

Our studies of ^{129}Xe relaxation on metal surfaces, though not definitive by any means, may lead to a direct observation of surface Korringa relaxation in the future. In the course of this work, we have gained a greater understanding of physical adsorption effects in general and the interesting adsorption behavior of xenon in particular.

The fundamental rate measurements provided here will aid us and others in understanding the basic physical interactions of the Rb-Xe system. The temperature dependences of the fundamental rates (measured here for the first time) are particularly interesting for the implications they may have for spin exchange optical pumping theory.

Taken as a whole, the work we have done has allowed us to model and design improved spin exchange optical pumping systems.

All of the work described in this thesis was undertaken with the hopes of not only having a practical impact on hyperpolarized gas production, but to gain a greater appreciation of the physics at work as well.

Appendix A

Full Rb Relaxation Equations

Following Appelt *et. al.* (reference [Appelt98], section XI), we write the rate equations for the spin-projections $\langle a \rangle_{iz}$ and $\langle b \rangle_{iz}$, where $a_i = I_i + \frac{1}{2}$ and $b_i = I_i - \frac{1}{2}$. In the absence of optical pumping,

$$\frac{d}{dt}\begin{pmatrix} a_{85z} \\ b_{85z} \\ a_{87z} \\ b_{87z} \end{pmatrix} = \tilde{\Gamma}\begin{pmatrix} a_{85z} \\ b_{85z} \\ a_{87z} \\ b_{87z} \end{pmatrix}, \tag{A.1}$$

where the (4×4) matrix $\tilde{\Gamma}$ is the sum of 3 matrices describing Rb-Rb spin exchange, S-damping, and F-damping: $\tilde{\Gamma} = \tilde{\Gamma}_{se} + \tilde{\Gamma}_{SD} + \tilde{\Gamma}_{FD}$.

$\tilde{\Gamma}_{SD}$ and $\tilde{\Gamma}_{FD}$ relax each isotope independently, so we can use the (2×2) matrices directly from [Appelt98]:

$$\tilde{\Gamma}_{SDi} = \frac{1}{2[\mathrm{I_i}]^2 T_{SDi}}\begin{pmatrix} [\mathrm{I_i}]^2 - [\mathrm{I_i}] + 2 & -[\mathrm{I_i}]^2 - 3[\mathrm{I_i}] - 2 \\ -[\mathrm{I_i}]^2 + 3[\mathrm{I_i}] - 2 & [\mathrm{I_i}]^2 + [\mathrm{I_i}] + 2 \end{pmatrix}, \tag{A.2}$$

and

$$\tilde{\Gamma}_{FDi} = \frac{1}{[\mathrm{I_i}]^2 T_{FDi}}\begin{pmatrix} 1 & 0 \\ 0 & 1 \end{pmatrix}, \tag{A.3}$$

where $1/T_{SDi} = ([\mathrm{Xe}]\langle \sigma v \rangle + f_{1,i}\Gamma_{vdW})$, the S-damping rate, and $1/T_{FDi} = (f_{0,i} -$

$f_{1,i})\Gamma_{vdW}$, the F-damping rate. For Rb,

$$\tilde{\Gamma}_{FD85} = (f_{0,85} - f_{1,85})\Gamma_{vdW} \begin{pmatrix} \frac{1}{36} & 0 \\ 0 & \frac{1}{36} \end{pmatrix} \tag{A.4}$$

$$\tilde{\Gamma}_{FD87} = (f_{0,87} - f_{1,87})\Gamma_{vdW} \begin{pmatrix} \frac{1}{16} & 0 \\ 0 & \frac{1}{16} \end{pmatrix} \tag{A.5}$$

$$\tilde{\Gamma}_{SD85} = (\Gamma_{bin} + f_{1,85}\Gamma_{vdW}) \begin{pmatrix} \frac{4}{9} & \frac{-7}{9} \\ \frac{-5}{18} & \frac{11}{18} \end{pmatrix} \tag{A.6}$$

$$\tilde{\Gamma}_{SD87} = (\Gamma_{bin} + f_{1,87}\Gamma_{vdW}) \begin{pmatrix} \frac{7}{16} & \frac{-15}{16} \\ \frac{-3}{16} & \frac{11}{16} \end{pmatrix}, \tag{A.7}$$

where we have defined $\Gamma_{bin} = [\mathrm{Xe}]\langle\sigma v\rangle$.

$\tilde{\Gamma}_{se}$ describes spin exchange both within each isotope and between isotopes. We then need 4 (2×2) matrices to describe the ^{85}Rb - ^{87}Rb system, $\tilde{\Gamma}_{se85\cdot85}$, $\tilde{\Gamma}_{se87\cdot87}$, $\tilde{\Gamma}_{se85\cdot87}$, and $\tilde{\Gamma}_{se87\cdot85}$, where

$$\tilde{\Gamma}_{sei\cdot j} = \frac{\delta_{ij}}{2[\mathrm{I_i}]^2 T_{ex}} \begin{pmatrix} [\mathrm{I_i}]^2 - [\mathrm{I_i}] + 2 & -[\mathrm{I_i}]^2 - 3[\mathrm{I_i}] - 2 \\ -[\mathrm{I_i}]^2 + 3[\mathrm{I_i}] - 2 & [\mathrm{I_i}]^2 + [\mathrm{I_i}] + 2 \end{pmatrix} + \\ + \frac{\eta_j}{6[\mathrm{I_i}][\mathrm{I_j}]T_{ex}} \begin{pmatrix} -[\mathrm{I_i}]^2 - 3[\mathrm{I_i}] - 2 & [\mathrm{I_i}]^2 + 3[\mathrm{I_i}] + 2 \\ [\mathrm{I_i}]^2 - 3[\mathrm{I_i}] + 2 & -[\mathrm{I_i}]^2 + 3[\mathrm{I_i}] - 2 \end{pmatrix}. \tag{A.8}$$

(Note that the first matrix in equation A.8 is identical to the S-damping matrix, equation A.2.) Solving these for Rb yields

$$\tilde{\Gamma}_{se85\cdot85} = \Gamma_{se} \begin{pmatrix} 0.258 & -0.591 \\ -0.211 & 0.544 \end{pmatrix} \tag{A.9}$$

$$\tilde{\Gamma}_{se87\cdot87} = \Gamma_{se} \begin{pmatrix} 0.350 & -0.850 \\ -0.170 & 0.670 \end{pmatrix} \tag{A.10}$$

$$\tilde{\Gamma}_{se85\cdot87} = \Gamma_{se} \begin{pmatrix} -0.109 & 0.109 \\ 0.0389 & -0.389 \end{pmatrix} \tag{A.11}$$

$$\tilde{\Gamma}_{se87\cdot85} = \Gamma_{se}\begin{pmatrix} -0.150 & 0.150 \\ 0.030 & -0.030 \end{pmatrix}, \tag{A.12}$$

where $\Gamma_{se} = 1/T_{se}$.

We can then construct the total (4×4) relaxation matrix:

$$\tilde{\Gamma} = \begin{pmatrix} \tilde{\Gamma}_{SD85} + \tilde{\Gamma}_{FD85} + \tilde{\Gamma}_{se85\cdot85} & \tilde{\Gamma}_{se85\cdot87} \\ \tilde{\Gamma}_{se87\cdot85} & \tilde{\Gamma}_{SD87} + \tilde{\Gamma}_{FD87} + \tilde{\Gamma}_{se87\cdot87} \end{pmatrix}. \tag{A.13}$$

Finding the fundamental relaxation rate is a matter of finding the smallest eigenvalue of this matrix, which depends upon $\Gamma_{vdW}\Gamma_{se}$ and Γ_{bin}/Γ_{se}. (In the high Γ_{se} limit, the smallest eigenvalue corresponds to equation 5.27.) The first order corrections to equation 5.27 are then obtained from the smallest eigenvalue of the total relaxation matrix to first order in Γ_{vdW}/Γ_{se}, Γ_{bin}/Γ_{se} minus the smallest eigenvalue in the high spin-exchange limit.

The following Mathematica-produced output (Wolfram Research, Inc.) illustrates how this may be done using first order perturbation theory. The S-damping, F-damping, and spin exchange matrices are constructed as above; note that j's and k's correspond to f_1's and f_0's, respectively.

The matrix "gam0" is the spin exchange matrix (*i.e.* the total matrix in the high spin exchange limit), with eigenvectors "u[[1]]" through "u[[4]]" and corresponding eigenvalues "γ[[1]]" through "γ[[4]]". Note that we have used $\Gamma_{se} = 1$; for example, Γ_{vdW} in the final form is actually Γ_{vdW}/Γ_{se}.

```
In[1]:= d[i_] := 2 i + 1

In[2]:= sd[a_, b_, i_] :=
         (({{d[i]^2 - d[i] + 2, -d[i]^2 - 3 d[i] - 2}, {-d[i]^2 + 3 d[i] - 2, d[i]^2 + d[i] + 2}} / 2 /
             d[i]^2)[[a]][[b]]

In[3]:= η[5 / 2] = 0.72

Out[3]= 0.72

In[4]:= η[3 / 2] = 0.28

Out[4]= 0.28

In[5]:= se[a_, b_, i_, j_] := (η[j] {{-d[i]^2 - 3 d[i] - 2, d[i]^2 + 3 d[i] + 2},
                   {d[i]^2 - 3 d[i] + 2, -d[i]^2 + 3 d[i] - 2}} / 6 / d[i] /
               d[j])[[a]][[b]]

In[6]:= gamsd = {{sd[1, 1, 5 / 2], sd[1, 2, 5 / 2], 0, 0}, {sd[2, 1, 5 / 2], sd[2, 2, 5 / 2], 0, 0},
          {0, 0, sd[1, 1, 3 / 2], sd[1, 2, 3 / 2]}, {0, 0, sd[2, 1, 3 / 2], sd[2, 2, 3 / 2]}}

Out[6]= {{4/9, -7/9, 0, 0}, {-5/18, 11/18, 0, 0}, {0, 0, 7/16, -15/16}, {0, 0, -3/16, 11/16}}

In[7]:= Eigenvalues[gamsd]

Out[7]= {-1/18, 1/8, 1, 1}

In[8]:= gamse =
          {{se[1, 1, 5 / 2, 5 / 2], se[1, 2, 5 / 2, 5 / 2], se[1, 1, 5 / 2, 3 / 2], se[1, 2, 5 / 2, 3 / 2]},
           {se[2, 1, 5 / 2, 5 / 2], se[2, 2, 5 / 2, 5 / 2], se[2, 1, 5 / 2, 3 / 2], se[2, 2, 5 / 2, 3 / 2]},
           {se[1, 1, 3 / 2, 5 / 2], se[1, 2, 3 / 2, 5 / 2], se[1, 1, 3 / 2, 3 / 2], se[1, 2, 3 / 2, 3 / 2]},
           {se[2, 1, 3 / 2, 5 / 2], se[2, 2, 3 / 2, 5 / 2], se[2, 1, 3 / 2, 3 / 2], se[2, 2, 3 / 2, 3 / 2]}}

        General::spell1 :
         Possible spelling error: new symbol name "gamse" is similar to existing symbol "gamsd".

Out[8]= {{-0.186667, 0.186667, -0.108889, 0.108889},
         {0.0666667, -0.0666667, 0.0388889, -0.0388889}, {-0.15, 0.15, -0.0875, 0.0875},
         {0.03, -0.03, 0.0175, -0.0175}}

In[9]:= gam0 = gamsd + gamse;

In[10]:= Eigensystem[gam0]

Out[10]= {{1., 0.717725, 0.104497, 2.17437×10^-16}, {{-0.404945, 0.289246, 0.743776, -0.446266},
           {-0.627986, 0.613259, -0.319319, 0.357186},
           {-0.272327, -0.186085, 0.902801, 0.275973},
           {-0.837408, -0.299074, -0.448611, -0.0897223}}}

In[11]:= u = %[[2]]

Out[11]= {{-0.404945, 0.289246, 0.743776, -0.446266},
          {-0.627986, 0.613259, -0.319319, 0.357186}, {-0.272327, -0.186085, 0.902801, 0.275973},
          {-0.837408, -0.299074, -0.448611, -0.0897223}}

In[12]:= γ = %%[[1]]

Out[12]= {1., 0.717725, 0.104497, 2.17437×10^-16}
```

```
In[13]:= q = gamsd * Γsd + Γse * gam0

        General::spell1 :
         Possible spelling error: new symbol name "Γse" is similar to existing symbol "Γsd".

Out[13]= {{4/9 Γsd + 0.257778 Γse, -7/9 Γsd - 0.591111 Γse, -0.108889 Γse, 0.108889 Γse},
          {-5/18 Γsd - 0.211111 Γse, 11/18 Γsd + 0.544444 Γse, 0.0388889 Γse, -0.0388889 Γse},
          {-0.15 Γse, 0.15 Γse, 7/16 Γsd + 0.35 Γse, -15/16 Γsd - 0.85 Γse},
          {0.03 Γse, -0.03 Γse, -3/16 Γsd - 0.17 Γse, 11/16 Γsd + 0.67 Γse}}

In[14]:= gam = Table[Table[1 / Eigenvalues[q /. {Γsd -> 1, Γse -> 10^(x)}][[m]], {x, -3, 3, .3}],
           {m, 1, 4}]

Out[14]= {{0.999001, 0.998009, 0.996035, 0.992119, 0.984398, 0.969347, 0.940649, 0.888184,
           0.79924, 0.666139, 0.5, 0.333861, 0.20076, 0.111816, 0.0593509, 0.0306534, 0.0156017,
           0.00788068, 0.00396529, 0.00199129, 0.000999001}, {0.999306, 0.998617, 0.997244,
           0.994516, 0.989114, 0.978505, 0.95798, 0.919422, 0.85085, 0.740123, 0.586753,
           0.414359, 0.260817, 0.149819, 0.0809922, 0.0422528, 0.0216191, 0.0109498,
           0.00551712, 0.00277251, 0.00139141}, {7.99361, 7.98725, 7.9746, 7.94948,
           7.89982, 7.80253, 7.61529, 7.26684, 6.6571, 5.69713, 4.41436, 3.03623, 1.86597,
           1.05338, 0.563354, 0.292124, 0.148989, 0.0753356, 0.0379263, 0.0190509, 0.00955883},
          {17.9909, 17.9819, 17.9639, 17.9283, 17.8583, 17.7224, 17.4652, 17.0023,
           16.2397, 15.1542, 13.8989, 12.7579, 11.9255, 11.4082, 11.1171, 10.9622,
           10.8821, 10.8414, 10.8208, 10.8104, 10.8052}}
```

Perturbation theory for Γse>>Γsd

```
In[29]:= uin = Inverse[Transpose[u]]

Out[29]= {{-0.265943, 0.531886, 0.354591, -1.06377},
          {-0.316445, 0.865267, -0.116806, 0.653289}, {-0.262049, -0.501375, 0.630633, 0.963874},
          {-0.743033, -0.743033, -0.288957, -0.288957}}

In[30]:= uin . gam0 . Transpose[u] // Chop

Out[30]= {{1., 0, 0, 0}, {0, 0.717725, 0, 0}, {0, 0, 0.104497, 0}, {0, 0, 0, 0}}

In[31]:= λ = uin[[4]] . gamsd . u[[4]] -
            Γsd Sum[uin[[4]] . gamsd . u[[m]] uin[[m]] . gamsd . u[[4]] / γ[[m]], {m, 1, 3}]

Out[31]= 0.0925926 - 0.0448992 Γsd

In[32]:= Table[1 / λ /. Γsd -> 10^(-x), {x, -3, 3, .3}]

Out[32]= {-0.0223182, -0.0446224, -0.0894009, -0.17986, -0.364917, -0.753441,
          -1.61548, -3.7871, -11.6071, 332.557, 20.9672, 14.2674, 12.2979, 11.5022,
          11.1409, 10.9682, 10.8836, 10.8418, 10.8209, 10.8105, 10.8052}
```

add F-damping

```
In[35]:= gamfd = DiagonalMatrix[{1 / 36, 1 / 36, 1 / 16, 1 / 16}]

        General::spell1 :
         Possible spelling error: new symbol name "gamfd" is similar to existing symbol "gamsd".

Out[35]= {{1/36, 0, 0, 0}, {0, 1/36, 0, 0}, {0, 0, 1/16, 0}, {0, 0, 0, 1/16}}
```

perturbation theory for the lowest eigenmode

```
In[37]:= λ =
          uin[[4]] . (Γsd gamsd + Γfd gamfd) . u[[4]] + -Sum[uin[[4]] . (Γsd gamsd + Γfd gamfd) . u[[m]]
                uin[[m]] . (Γsd gamsd + Γfd gamfd) . u[[4]] / γ[[m]], {m, 1, 3}] //
            Simplify //
           Expand

Out[37]= 0.033179 Γfd - 0.00145836 Γfd^2 + 0.0925926 Γsd - 0.00837228 Γfd Γsd - 0.0448992 Γsd^2
```

```
In[38]:= 0.0331790123456789975` / 0.0925925925925925774`

Out[38]= 0.358333
```

Full theory for Ian's expt, high spin-exchange rate

```
In[39]:= gamsd = {{j85 sd[1, 1, 5 / 2], j85 sd[1, 2, 5 / 2], 0, 0}, {j85 sd[2, 1, 5 / 2],
           j85 sd[2, 2, 5 / 2], 0, 0}, {0, 0, j87 sd[1, 1, 3 / 2], j87 sd[1, 2, 3 / 2]},
          {0, 0, j87 sd[2, 1, 3 / 2], j87 sd[2, 2, 3 / 2]}}

Out[39]= {{4 j85/9, -7 j85/9, 0, 0}, {-5 j85/18, 11 j85/18, 0, 0}, {0, 0, 7 j87/16, -15 j87/16},
          {0, 0, -3 j87/16, 11 j87/16}}

In[40]:= gamfd = DiagonalMatrix[{(k85 - j85) / 36, (k85 - j85) / 36, (k87 - j87) / 16, (k87 - j87) / 16}]

Out[40]= {{1/36 (-j85 + k85), 0, 0, 0}, {0, 1/36 (-j85 + k85), 0, 0}, {0, 0, 1/16 (-j87 + k87), 0},
          {0, 0, 0, 1/16 (-j87 + k87)}}

In[41]:= gamian = ΓvdW (gamsd + gamfd) + Γbin (gamsd /. {j85 -> 1, j87 -> 1})

Out[41]= {{4 Γbin/9 + (4 j85/9 + 1/36 (-j85 + k85)) ΓvdW, -7 Γbin/9 - 7 j85 ΓvdW/9, 0, 0},
          {-5 Γbin/18 - 5 j85 ΓvdW/18, 11 Γbin/18 + (11 j85/18 + 1/36 (-j85 + k85)) ΓvdW, 0, 0},
          {0, 0, 7 Γbin/16 + (7 j87/16 + 1/16 (-j87 + k87)) ΓvdW, -15 Γbin/16 - 15 j87 ΓvdW/16},
          {0, 0, -3 Γbin/16 - 3 j87 ΓvdW/16, 11 Γbin/16 + (11 j87/16 + 1/16 (-j87 + k87)) ΓvdW}}

In[42]:= λ = uin[[4]] . gamian . u[[4]] +
           -Sum[uin[[4]] . gamian . u[[m]] uin[[m]] . gamian . u[[4]] / γ[[m]], {m, 1, 3}] //
          Simplify

Out[42]= -0.0448992 Γbin^2 + Γbin (0.0925926 - 0.0483073 j85 ΓvdW -
            0.0331187 j87 ΓvdW + 0.00669783 k85 ΓvdW - 0.0150701 k87 ΓvdW) +
          ΓvdW (0.0162037 j87 + 0.0234568 k85 + 0.00972222 k87 - 0.0238079 j85^2 ΓvdW -
            0.0127251 j87^2 ΓvdW + 0.00497299 j87 k85 ΓvdW - 0.000933349 k85^2 ΓvdW -
            0.0111892 j87 k87 ΓvdW + 0.00420007 k85 k87 ΓvdW - 0.00472508 k87^2 ΓvdW +
            j85 (0.0432099 - 0.00145218 j87 ΓvdW - 0.000608534 k85 ΓvdW + 0.0013692 k87 ΓvdW))

In[43]:= Expand[%]

Out[43]= 0.0925926 Γbin - 0.0448992 Γbin^2 + 0.0432099 j85 ΓvdW + 0.0162037 j87 ΓvdW +
          0.0234568 k85 ΓvdW + 0.00972222 k87 ΓvdW - 0.0483073 j85 Γbin ΓvdW - 0.0331187 j87 Γbin ΓvdW +
          0.00669783 k85 Γbin ΓvdW - 0.0150701 k87 Γbin ΓvdW - 0.0238079 j85^2 ΓvdW^2 -
          0.00145218 j85 j87 ΓvdW^2 - 0.0127251 j87^2 ΓvdW^2 - 0.000608534 j85 k85 ΓvdW^2 +
          0.00497299 j87 k85 ΓvdW^2 - 0.000933349 k85^2 ΓvdW^2 + 0.0013692 j85 k87 ΓvdW^2 -
          0.0111892 j87 k87 ΓvdW^2 + 0.00420007 k85 k87 ΓvdW^2 - 0.00472508 k87^2 ΓvdW^2

In[44]:= N[%, 3]

Out[44]= 0.0926 Γbin - 0.0449 Γbin^2 + 0.0432 j85 ΓvdW + 0.0162 j87 ΓvdW +
          0.0235 k85 ΓvdW + 0.00972 k87 ΓvdW - 0.0483 j85 Γbin ΓvdW - 0.0331 j87 Γbin ΓvdW +
          0.0067 k85 Γbin ΓvdW - 0.0151 k87 Γbin ΓvdW - 0.0238 j85^2 ΓvdW^2 - 0.00145 j85 j87 ΓvdW^2 -
          0.0127 j87^2 ΓvdW^2 - 0.000609 j85 k85 ΓvdW^2 + 0.00497 j87 k85 ΓvdW^2 - 0.000933 k85^2 ΓvdW^2 +
          0.00137 j85 k87 ΓvdW^2 - 0.0112 j87 k87 ΓvdW^2 + 0.0042 k85 k87 ΓvdW^2 - 0.00473 k87^2 ΓvdW^2
```

Appendix B

ECDLA Alignment Procedure

In the interest of assisting future students in our group in ECDLA construction, I include this step by step construction and alignment procedure.

B.1 Parts List:

1. 1 cm long high power diode array
2. Diode current driver capable of 30 Amps output (Newport 5405)
3. Temperature controller capable of 8 Amps output (Melcor 12080)
4. High power diode laser mount (Newport 762-TE includes TEC for temperature control)
5. Cylindrical microlens (Doric lenses 1.500 mm diameter, 2.5 cm length, BBAR coated)
6. 2× Newport GM-1R 3-axis waveplate/polarizer holder
7. 2× Newport RSA-1TI solid insert

8. 25.4 mm diameter, 50 mm focal length lens, BBAR coated (plano-convex singlet or achromat)
9. $\lambda/2$ plate in a rotating optics mount
10. 100 mm diameter, 250 mm focal length lens, BBAR coated (Melles Griot)
11. 50mm x 50mm 2400 lines/mm holographic diffraction grating (Edmund Scientific K43-226)
12. Cylindrical lens, 75.6 mm focal length
13. Linear translation stage (New Focus EZ-track)
14. 2-axis translator (New Focus EZ-track)
15. assorted posts, bases, optical breadboard or table

B.2 Machining:

Enlarge the center hole of one of the RSA-1TI inserts to 2 cm diameter. This insert will serve as the cylindrical microlens holder. Mill a 1.50 mm diameter groove, semicircular in cross section, across the diameter of this insert. Cement the microlens into this groove.

We have found it helpful to attach a 3" mirror in the following manner to one of the GM-1R mounts (which will serve as the diffraction grating mount), such that the angle that this mirror makes with the GM-1R face is fixed. Though not necessary for ECDLA operation, it minimizes the beam movement with tuning which is inherent to Littrow cavity designs. Drill and tap an 8-32 hole in the center of the top edge of the GM-1R face. Using this hole, bolt a $\approx$5 cm long aluminum bar to the GM-1R. Bolt

the mirror (in a suitable mount) to this bar such that it hangs from the end of the bar at an adjustable angle and is mechanically stable.

B.3 Position array

Mount the array on the high power mount. Secure the mount to the optical table such that the long dimension of the array is oriented vertically and the array output will be aligned with a row of holes in the optical table. Turn on array to just above threshold. The divergence in the vertical direction should be only $\approx 10°$, allowing the angle of inclination of the array to be set at $0°$ (parallel to optical table) by observing the height of the illuminated horizontal stripe on a far wall.

B.4 Align microlens

Turn the machined cylindrical microlens holder into one of the GM-1R holders, and position this on the 2-axis translator such that the center of the microlens is at the height of the center of the array, or at $y = 0$ (refer to figure 4.4 for coordinate axes, where the array center defines $(0, 0, 0)$). Using the translator, center the microlens approximately 2 mm from the array. Position the 75.6 mm focal length cylindrical lens at $z = 9$ cm, and place a screen at $z = 58$ cm. With the array running just above threshhold, carefully translate the microlens in towards $z = 0$ while observing the screen. At some point an image of some portion of the array should begin to come into focus on the screen (visible as individual elements, perhaps displaying "smile" as in figure 4.5).

Keeping in mind that this image is inverted, use the xz-translation adjustments and the GM-1R tilt/rotation adjustments to properly collimate the fast axis of the array

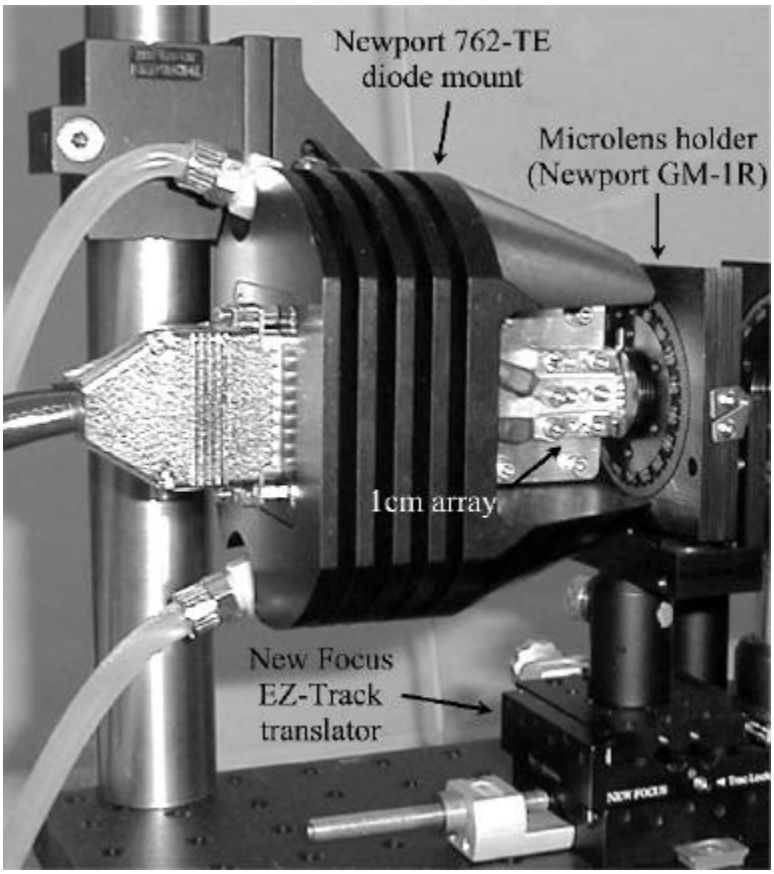

Figure B.1: High power laser diode array mount and microlens.

output. For example, if the *top* of the image comes into focus before the bottom as the microlens is brought closer to the array, then the *bottom* of the microlens is closer than the top. Adjust the GM-1R tilt accordingly. Similarly adjust the rotation angle of the GM-1R to make the image as vertical as possible. Also adjust the x-position of the microlens (using the xz-translator) to properly align the collimated output along $x = 0$ (some iteration may be necessary if the various adjustments are not precisely orthogonal).

When finished, an image similar to those in figure 4.5 should be visible on the screen. (This is a good time to measure the amount of smile present in the array.) Remove the screen and move the 75.6 mm cylindrical lens closer to the array such that an image of the vertical dimension of the array appears on a far wall. Complete the microlens adjustment by decreasing the z-position of the microlens slightly, such that the fast axis of the array is collimated. Remove the 75.6 mm focal length cylindrical lens.

B.5 Align telescope

Place the 50 mm focal length lens at $z = 5$ cm. Observe the large image of the vertical dimension of the array on a far wall. Adjust the height of the 50 mm lens such that the vertical center of this image is at the same height as the center of the array itself. Adjust the x-position of this lens such that the image appears at $x = 0$. Adjust the z-position of the lens to bring the image into focus.

Place the $\lambda/2$ plate at approximately $z = 10$ cm, the 250 mm focal length lens at $z = 35$ cm, and a screen at $z = 60$ cm. Adjust the (x, y, z) position of the 250 mm lens to produce a well focused image of the vertical dimension of the array on the screen centered on $(x, y) = (0, 0)$.

B.6 Position grating

Cement the second RSA-1TI insert to the center of the back of the diffraction grating. Screw the grating into the second GM-1R holder. Align the grooves of the grating along the $\hat{y}$ direction. Mount the GM-1R holder on the translation stage (translatable along z) such that the center of the grating is located at $(x, y, z) = (0, 0, 60\text{cm})$ and the grating normal makes approximately the Littrow angle with the z-axis (72.6° for $\lambda = 795$ nm). An image of the vertical dimension of the array should approximately fill the grating. This image should be well focused along the horizontal center of the grating, and should not deviate significantly from well focused near the image edges.

B.7 Adjust feedback

Use some appropriate method for observing the frequency of the array output in real time (e.g. Ocean Optics S2000 spectrometer). Care mut be taken to observe all of the array elements with the spectrometer. In practice, this means collecting all of the output light with a suitable lens and passing it through at least one diffusing medium before entering the spectrometer. Some subset of array elements may be blocked and unblocked just after the diffraction grating in order to verify that they are contributing to the spectrometer signal.

With the array running slightly above threshhold, make fine adjustments to the grating position, tilt, rotation, and tuning angle to optimize ECDLA output (i.e. maximize frequency tuning range and minimize frequency bandwidth), setting the $\lambda/2$ plate to achieve as much frequency-narrowed output as possible. Only after good performance is achieved at low power should the current to the array be turned up to the desired operating level, at which point more fine grating adjustments may need to be

made (the ECDLA output will be narrower and tune significantly better just above threshhold than at higher power, hence the recommendation to begin optimization at lower power.)

Very fine adjustments of the other optical elements (especially the microlens) may be necessary, depending on the dominant source of frequency broadening. Observing ouput frequency differences between various subsets of array elements can be a valuable means to diagnose suboptimal ECDLA performance associated with microlens rotation (which leads to a different ϕ for different elements exactly as does array smile (see equation 4.7)).

Appendix C

Calculated Surface Korringa Relaxation Times

The following table lists the metals from the periodic table ordered by atomic number. The work functions, ϕ, have been taken from the CRC Handbook of Chemistry and Physics [CRC], where the references cited there are [Holzl79][Riviere69][Michaelson77]. ϕ varies according to crystal face for monocrystalline samples; where the CRC lists values for more than one crystal face, the value in the table below is approximately the average. Conduction electron densities listed are from Tipler's *Modern Physics* (Table 9-2) when possible, and otherwise are taken from reference [Rose91].

The fourth column, "^{129}Xe T_{1cc}", lists the surface Korringa relaxation times for ^{129}Xe in a 1 cm^3 spherical cell at 20°C, as predicted by equation 3.9. The fifth column, "^{129}Xe T'_{1cc}", lists the relaxation times for those conditions as predicted by equation 3.40, which includes a modification to account for ^{129}Xe monolayer formation. This modification is pressure dependent — these numbers represent the values predicted for our experimental pressure, 2.5 amagats.

The sixth column lists the relaxation times for ^{3}He under those conditions as pre-

dicted by equation 3.9. As the binding energy for ^{3}He on all metals listed is much less than kT, equation 3.40 gives the same result.

The remaining columns contain the approximate binding energies (ϵ_0) and locations of the potentials' minima (r_0) as calculated from ϕ via our semiempirical method.

Conduction electron densities, $[e^-]_c$, are in units of $\times 10^{22}$ cm^{-3}. ^{129}Xe relaxation times are listed in number of *hours*, while ^{3}He times are *years*.

Metal	$[e^-]_c$	ϕ (eV)	^{129}Xe T_{1cc}	^{129}Xe T'_{1cc}	^{3}He T_{1cc}	r_0(Xe) (Å)	ϵ_0(Xe) (meV)	r_0(He) (Å)	ϵ_0(He) (meV)
Li	5.7	2.9	28	31	1500	2.8	88	4.5	2.7
Be	5.32	4.98	.74	1.9	4700	2.2	198	3.5	6.0
Na	2.65	2.36	90	96	1500	3.1	65	5.0	2.0
Mg	8.61	3.66	6.7	8.1	1800	2.5	125	4.0	3.8
Al	18.1	4.2	1.6	2.2	1500	2.4	153	3.8	4.6
K	1.4	2.3	147	155	2200	3.2	62	5.1	1.9
Ca	3.16	2.87	44	47	2100	2.8	87	4.6	2.6
Sc	4.22	3.5	14	16	2700	2.6	120	4.1	3.5
Ti	4.83	4.33	3.0	4.4	3800	2.3	160	3.7	4.9
V	5.38	4.3	2.9	4.3	3500	2.3	159	3.7	4.8
Cr	5.7	4.5	1.9	3.1	3700	2.3	170	3.7	5.1
Mn	16.5	4.1	2.0	2.7	1500	2.4	150	3.8	4.5
Fe	17	4.7	.61	1.2	1900	2.2	180	3.6	5.5
Co	5.56	5	.69	1.8	4600	2.2	200	3.5	6.0
Ni	5.43	5.15	.51	1.6	5000	2.1	210	3.4	6.3
Cu	8.47	4.65	1.1	2.0	3000	2.2	180	3.6	5.4
Zn	13.2	4	2.8	3.6	1600	2.4	140	3.9	4.3
Ga	4.26	4.2	4.1	5.8	3900	2.4	150	3.8	4.6
Ge		5.0				2.2	200	3.5	6.0

Metal	$[e^-]_c$	ϕ (eV)	^{129}Xe T_{1cc}	^{129}Xe T'_{1cc}	^{3}He T_{1cc}	r_0(Xe) (Å)	ϵ_0(Xe) (meV)	r_0(He) (Å)	ϵ_0(He) (meV)
Rb	1.04	2.26	187	196	2600	3.2	60	5.2	1.8
Sr	2.95	2.59	65	69	1800	3	74	4.8	2.2
Y	3.92	3.1	27	30	2200	2.7	97	4.4	2.9
Zr	4.63	4.05	5.1	6.8	3400	2.4	150	3.8	4.4
Nb	5.24	4.3	3.0	4.4	3500	2.3	160	3.7	4.8
Mo	5.59	4.6	1.6	2.8	3900	2.2	180	3.6	5.3
Tc	5.68								
Ru	5.68	4.71	1.2	2.4	4000	2.2	180	3.6	5.5
Rh	5.49	4.98	.73	1.9	4600	2.2	200	3.5	6.0
Pd	5.1	5.12	.57	1.7	5100	2.1	210	3.4	6.2
Ag	5.86	4.6	1.5	2.7	3800	2.2	180	3.6	5.3
Cd	4.15	4.22	4.0	5.7	4000	2.3	150	3.8	4.7
In	3.89	4.12	5.1	6.7	4000	2.4	150	3.8	4.5
Sn	14.8	4.42	1.2	1.8	1900	2.3	170	3.7	5.0
Sb		4.55				2.3	170	3.6	5.2
Cs	1.9	1.95	164	171	1300	3.5	48	5.5	1.5
Ba	2.92	2.7	57	62	1900	2.9	79	4.7	2.4
La	3.88	3.5	15	17	2800	2.6	120	4.1	3.5
Hf	4.81	3.9	6.6	8.3	3100	2.4	140	3.9	4.1
Ta	5.38	4.25	3.2	4.6	3400	2.3	160	3.8	4.7
W	5.71	4.55	1.7	2.9	3800	2.3	170	3.6	5.2

Metal	$[e^-]_c$	ϕ (eV)	^{129}Xe T_{1cc}	^{129}Xe T'_{1cc}	^{3}He T_{1cc}	r_0(Xe) (Å)	ϵ_0(Xe) (meV)	r_0(He) (Å)	ϵ_0(He) (meV)
Re	5.88	4.96	.72	1.8	4400	2.2	200	3.5	5.9
Os	5.92	4.83	.95	2.0	4100	2.2	190	3.5	5.7
Ir	5.75	5.27	.38	1.4	5000	2.1	220	3.4	6.5
Pt	5.43	5.65	.17	1.2	5900	2.0	240	3.3	7.2
Au	5.9	5.1	.54	1.6	4600	2.1	200	3.4	6.2
Hg	4.07	4.49	2.4	4.0	4600	2.3	170	3.7	5.1
Tl	3.73	3.84	8.6	10.7	3500	2.5	134	4.0	4.1
Pb	3.64	4.25	4.2	6.0	4400	2.3	156	3.8	4.7
Bi		4.22				2.3	150	3.8	4.7

Bibliography

[Abramowitz] M. Abramowitz and I. A. Stegun (ed.), *Handbook of Mathematical Functions*, Dover Publications, Inc., New York (1972).

[Albert94] M. S. Albert, G. D. Cates, B. Driehuys, W. Happer, C. S. Springer, Jr., B. Saam, and A. Wishnia, Nature (London), Phys. Sci. **370**, 199 (1994).

[Anderson59] L. W. Anderson, F. M. Pipkin and J. C. Baird, Phys. Rev. **116**, 87 (1959).

[Anderson60] L. W. Anderson, F. M. Pipkin and J. C. Baird, Phys. Rev. Lett. **120**, 1279 (1960).

[Anthony93] P. L. Anthony, R. G. Arnold, H. R. Band, H. Borel, P. E. Bosted, V. Breton, G. D. Cates, T. E. Chupp, F. S. Dietrich, J. Dunne, R. Erbacher, J. Fellbaum, H. Fonvieille, R. Gearhart, R. Holmes, E. W. Hughes, J. R. Johnson, D. Kawall, C. Keppel, S. E. Kuhn, R. M. Lombard-Nelsen, J. Marroncle, T. Maruyama, W. Meyer, Z.-E. Meziani, H. Middleton, J. Morgenstern, N. R. Newbury, G. G. Petratos, R. Pitthan, R. Prepost, Y. Roblin, S. E. Rock, S. H. Rokni, G. Shapiro, T. Smith, P. A. Souder, M. Spengos, F. Staley, L. M. Stuart, Z. M. Szalata, Y. Terrien, A. K. Thompson, J. L. White, M. Woods, J. Xu, C. C. Young, and G. Zapalac, Phys. Rev. Lett. **71**, 959 (1993).

[Appelt98] S. Appelt, A. Ben-Amar Baranga, C. J. Erickson, M. V. Romalis, A. R. Young, and W. Happer, Phys. Rev. A **58**, 1412 (1998).

[Appelt99] S. Appelt, T. Unlu, K. Zilles, N. J. Shah, S. Baer-Lang, and H. Halling, Appl. Phys. Lett. **75**, 427 (1999).

[Aymar69] M. Aymar, M. A. Bouchiat, and J. Brossel, Le Journal de Physique **30**, 619 (1969).

[Baranga98] A. Ben-Amar Baranga, S. Appelt, M. V. Romalis, C. J. Erickson, A. R. Young, G. D. Cates, and W. Happer, Phys. Rev. Lett. **80**, 2801 (1998).

[Baranga98b] A. Ben-Amar Baranga, S. Appelt, C. J. Erickson, A. R. Young, and W. Happer, Phys. Rev. A **58**, 2282 (1998).

[Bear98] D. Bear, T. E. Chupp, K. Cooper, S. Dedeo, M. Rosenberry, R. E. Stoner, and R. L. Walsworth, Phys. Rev. A **57**, 5006 (1998).

[Bhaskar82] N. Bhaskar, W. Happer, and T. McClelland, Phys. Rev. Lett. **49**, 25 (1982).

[Bhaskar83] N. D. Bhaskar, W. Happer, M. Larsson, and X. Zeng, Physical Review Letters **50**, 105 (1983).

[Bonin] K. Bonin and V. Kresin, *Electric-dipole polarizabilities of atoms, molecules, and clusters*, World Scientific, River Edge, NJ (1997).

[Botez94] D. Botez and D. Scifres, eds., *Diode Laser Arrays*, Cambridge U. Press, Cambridge, (1994).

[Bouchiat72] M. A. Bouchiat, J. Brossel, and L. C. Pottier, J. Chem. Phys. **56**, 3703 (1972).

[Brown94] E. R. Brown, K. A. McIntosh, F. W. Smith, K. B. Nichols, M. J. Manfra, C. L. Dennis, and J. P. Mattia, Appl. Phys. Lett. **64**, 3311 (1994).

[Bruch] L. W. Bruch, M. W. Cole, and E. Zaremba, *Physical Adsorption: Forces and Phenomena*, Oxford University Press Inc., New York (1997).

[Cates88] G. D. Cates, S. R. Schaefer, and W. Happer, Physical Review A **37**, 2877 (1988).

[Cates88b] G. D. Cates, D. J. White, Ting-Ray Chien, S. R. Schaefer, and W. Happer, Physical Review A, **38**, 5092 (1988).

[Cates92] G. D. Cates, R. J. Fitzgerald, A. S. Barton, P. Bogorad, M. Gatzke, N. R. Newbury, and B. Saam, Phys. Rev. A, **45**, 4631 (1992).

[Chizmeshya92] A. Chizmeshya and E. Zaremba, Surface Science, **268**, 432 (1992).

[Chupp94] . E. Chupp, R. J. Hoare, R. L. Walsworth, and Bo Wu, Physical Review Letters **72**, 2363.

[CRC] *CRC Handbook of Chemistry and Physics* CRC Press, Inc., Boca Raton, Florida (1989)

[Daneu00] V. Daneu, A. Sanchez, T. Y. Fan, H. K. Choi, G. W. Turner, and C. C. Cook, Opt. Lett. **25**, 405 (2000).

[Driehuys95] B. Driehuys, G. D. Cates, and W. Happer, Phys. Rev. Lett. **74**, 4943 (1995).

[Driehuys96] B. Driehuys, G. Cates; E. Miron; K. Sauer, D. Walter, and W. Happer, Appl. Phys. Lett. **69**, 1668 (1996).

[DriehuysPC] B. Driehuys, private communication.

[Duarte] P. Zorabedian, in *T*unable Lasers Handbook, edited by F. J. Duarte (Academic, San Diego, 1995), p. 349.

[Erickson00] C. J. Erickson, D. Levron, W. Happer, S. Kadlecek, B. Chann, L. W. Anderson, and T. G. Walker, Phys. Rev. Lett. **85**, 4237 (2000).

[Eriksen99] T. Eriksen, U. Hoppe, E. Thrane, and T. Blix, Appl. Opt. **38**, 2605 (1999).

[Gamblin65] R. L. Gamblin and T. R. Carver, Physical Review A **138**, 946 (1965)

[Grover78] B. C. Grover, Phys. Rev. Lett. **40**, 391 (1978).

[Happer84] W. Happer, E. Miron, S. Schaefer, D. Schreiber, W. A. van Wijngaarden, and X. Zeng, Phys. Rev. A **29**, 3092 (1984).

[Hasson90] K. C. Hasson, G. D. Cates, K. Lerman, P. Bogorad, and W. Happer, Physical Review A, **41**, 3672 (1990).

[Hecht] E. Hecht, *Optics*, Addison-Wesley Publishing Company, Inc., Reading, MA (1987).

[Heil95] W. Heil, H. Humblot, E. Otten, M. Schaeffer, R. Sarkau, M. Leduc, Physics Letters A **201**, 337 (1995).

[Hölzl79] J. Hölzl and F. K. Schulte, Work Functions of Metals, in *S*olid State Surface Physics, G. Höhler, editor, Springer-Verlag, Berlin (1979).

[Hsu99] L. Hsu, L. Chi, S. Wang, and C. Pan, Opt. Commun. **168**, 195 (1999).

[Hunt63] E. R, Hunt and H. Y. Carr, Physical Review **130**, 2302 (1963).

[Jackson] J. D. Jackson, *Classical Electrodynamics*, John Wiley & Sons, Inc., New York (1975).

[Kadlecek98] S. Kadlecek, L. W. Anderson and T. G. Walker, Phys. Rev. Lett. **80**, 5512 (1998).

[Killian26] T. Killian, Physical Review **27**, 578 (1926).

[Korringa50] J. Korringa, Physica **16**, 601 (1950)

[Krauss90] M. Krauss and W. J. Stevens, Journal of Chemical Physics **94**, 4236 (1990).

[Levron98] D. Levron, D. K. Walter, S. Appelt, R. J. Fitzgerald, D. Kahn, S. E. Korbly, K. L. Sauer, W. Happer, T. L. Earles, L. J. Mawst, D. Botez, M. Harvey, L. DiMarco, J. C. Connolly, H. E. Mller, X. J. Chen, G. P. Cofer, and G. A. Johnson, Appl. Phys. Lett. **73**, 2666 (1998).

[Littman78] M. Littman and H. Metcalf, Appl. Opt. **17**, 2224 (1978).

[Lotem92] H. Lotem, Z. Pan, and M. Dagenais, Appl. Opt. **31**, 7530 (1992).

[MacFall96] J. R. MacFall, Radiology **200**, 553 (1996).

[Michaelson77] H. B. Michaelson, Journal of Applied Physics, **48**, 4729 (1977).

[Navon96] G. Navon, Y. Song, T. Room, S. Appelt, R. Taylor, and A. Pines, Science **271**, 1848 (1996).

[Nordlander84] P. Nordlander and J. Harris, Journal of Physics C, **17**, 1141 (1984).

[Phillips99] D. Phillips, G. Wong, D. Bear, R. Stoner, and R. Walsworth, Rev. Sci. Instrum. **70**, 2905 (1999).

[Raftery91] D. Raftery, H. Long, T. Meersmann, P. J. Graninetti, L. Reven, and A. Pines, Phys. Rev. Lett. **66**, 584 (1991).

[Ramsey83] N. Ramsey, E. Miron, X. Zeng, and W. Happer, Chem. Phys. Lett. **102**, 340 (1983).

[Riviere69] J. C. Riviere, Work Function: Measurements and Results, in *S*olid State Surface Science, Vol. 1, M. Green, editor, Decker, New York (1969).

[Rose91] J. H. Rose and H. B. Shore, Physical Review B **43**, 11605 (1991)

[Rosen99] M. S. Rosen, T. E. Chupp, K. P. Coulter, R. C. Welsh, and S. D. Swanson, Rev. Sci. Instrum. **70**, 1546 (1999).

[Schaefer90] S. R. Schaefer, G. D. Cates, and W. Happer, Physical Review A **41**, 6063 (1990).

[Schearer65] L. D. Schearer and G. K. Walters, Physical Review A **139**, 1398 (1965)

[Shah00] N. Shah, T. Unlu, H. Wegener, H. Halling, K. Zilles, and S. Appelt, NMR in Biomedicine **13**, 214 (2000).

[Slichter] C. P. Slichter, *Principles of Magnetic Resonance*, Springer-Verlag Berlin Heidelberg (1990).

[Swanson97] S. D. Swanson, M. S. Rosen, B. W. Agranoff, K. P. Coulter, R. C. Welsh, and T. E. Chupp, Magn. Res. Med. **38**, 695 (1997).

[Torrey63] H. C. Torrey, Physical Review **130**, 2306 (1963).

[Tseng98] C. H. Tseng, G. P. Wong, V. R. Pomeroy, R. W. Mair, D. P. Hinton, D. Hoffmann, R. E. Stoner, F. W. Hersman, D. G. Cory, and R. L. Walsworth, Phys. Rev. Lett. **81**, 3785 (1998).

[Vliegen01] E. Vliegen, S. Kadlecek, L. W. Anderson, and T. G. Walker, Nucl. Inst. Meth. Phys. Res. A, (2001) accepted for publication.

[Wagshul94] M. E. Wagshul and T. E. Chupp, Physical Review A, **49**, 3854 (1994).

[Walker89] T. G. Walker, Physical Review A **40** 4959 (1989).

[Walker97] T. G. Walker and W. Happer, Rev. Mod. Phys. **69**, 629 (1997).

[Walter01] *to be published*

[Wang95] Chi-Luen Wang and Ci-Ling Pan, Optics Letters **20**, 1292 (1995).

[Wieman91] C. Wieman and L. Hollberg, Rev. Sci. Instrum. **62**, 1 (1991).

[Wu85] Z. Wu, T. G. Walker, and W. Happer, Phys. Rev. Lett. **54**, 1921 (1985).

[Wu86] Z. Wu, T. G. Walker, and W. Happer, Applied Optics **25**, 4483 (1986).

[Wu90] Z. Wu, W. Happer, M. Kitano, and J. Daniels, Physical Review A **42**, 2774 (1990).

[Zeng85] X. Zeng, Z. Wu, T. Call, E. Miron, D. Schreiber, and W. Happer, Phys. Rev. A **31**, 260 (1985).

[Zerger00] J. N. Zerger, M. J. Lim, K. P. Coulter, and T. E. Chupp, Applied Physics Letters, **76**, 1798 (2000).